

Surface Phase Stability and Surfactant Behavior on InAsSb

by

Evan M. Anderson

A dissertation submitted in partial fulfillment
of the requirements for the degree of
Doctor of Philosophy
(Materials Science and Engineering)
in The University of Michigan
2017

Doctoral Committee:

Professor Joanna Millunchick, Chair
Associate Professor Emmanuelle Marquis
Professor Chris Pearson, University of Michigan-Flint
Associate Professor Donald Siegel

© Evan M. Anderson 2017

All Rights Reserved

ACKNOWLEDGEMENTS

I have many people to thank for helping me complete this dissertation, though expressing gratitude is difficult here in writing. First and foremost, I have to thank Annalise, the love of my life. I couldn't have completed my dissertation without her. She brightens my day and cheers me up when I start taking things too seriously. On that note, I have to acknowledge our dog London (whom Annalise convinced me we should adopt) for alternately cuddling next to me during long days of writing and obligating me go outside to take her running.

I would like to thank my family, especially my parents and grandparents, for their continued support. They helped cultivate my interest in science and have always provided me with guidance to become a better man. They give me encouragement and perspective when life's challenges seem overwhelming. I have Dave and Amy Rohweder to thank for inviting me to their cabin up North as a chance to get out of Ann Arbor for a little while.

I have to thank Prof. Joanna Millunchick for her guidance. She has shown me how to look at different angles of a problem to conduct research effectively. I am grateful for her excellent mentoring, expertise in materials science, and remarkable patience with me. I also have to thank those who helped me learn the details of the techniques I used to conduct my research: Prof. Chris Pearson, Dr. Andy Martin, Dr. Adam Duzik, Dr. Matt DeJarld, Dr. John Thomas, Dr. Normand Modine, and Prof. Jessica Bickel. I thank Adam Lundquist for gathering some of the more time consuming data. I would like to thank Profs. Emmanuelle Marquis and Don Siegel for helpful suggestions and questions that lead me to a greater understanding of my work. I have Dr. Tim Chambers to thank for providing additional encouragement.

I would like to thank Alan Olvera and Kyle Johnson for our semi-regular coffee and writing "club" and Aaron Lamoureux, Kevin Fisher, Ellen Solomon, and Beck Andrews for occasional trivia nights and get-togethers as a break from the stresses of grad school and Jim Ropa for weekly trail running. I want to thank Rick Feddema and Mattie Hensley for their occasional visits from Albuquerque and regular Skype chats to keep me and Annalise sane.

TABLE OF CONTENTS

ACKNOWLEDGEMENTS	ii
LIST OF TABLES	viii
LIST OF FIGURES	ix
LIST OF APPENDICES	xiii
LIST OF ABBREVIATIONS	xiv
ABSTRACT	xv
CHAPTER 1 Introduction	1
1.1 Overview and Organization.....	3
CHAPTER 2 Background and Methods	6
2.1 Surface Reconstructions	6
2.2 Surfactants in Semiconductor Growth	8
2.3 Molecular Beam Epitaxy	8
2.3.1 Beam Flux Measurement	9
2.3.2 RHEED Patterns and Oscillations	9
2.4 Scanning Tunneling Microscopy.....	12

2.4.1	Measurements on STM Images	12
2.5	Calculations	13
2.5.1	Procedure for DFT Calculations and Cluster Expansion.....	13
2.5.2	Monte Carlo	18
2.6	Thermodynamics of Surfaces.....	19
2.6.1	0K Surface Energy	20
2.6.2	Finite Temperature Surface Energy.....	22
CHAPTER 3 Interaction Between Sb and As on InAs Surfaces.....		24
3.1	Introduction.....	24
3.2	Procedure and Nomenclature	26
3.2.1	MBE Growth, RHEED, and STM.....	26
3.2.2	Calculations	27
3.2.3	Surface Reconstruction Nomenclature.....	28
3.3	Results and Discussion	29
3.3.1	Surface Reconstruction Driven Sb-As Intermixing	30
3.3.2	Control of Surface Stoichiometry	41
3.3.3	Surface Roughening and Intermixing Driven by Phase Transition	46
3.4	Conclusions	54
CHAPTER 4 Finite Temperature Stabilization of InSb and As on InSb Surface Reconstructions.....		56

4.1	Introduction.....	56
4.2	Procedure and Nomenclature	57
4.2.1	Calculations	57
4.2.2	MBE Growth, RHEED, and STM.....	59
4.2.3	Surface Reconstruction Nomenclature.....	60
4.3	Results and Discussion	60
4.3.1	Newly Calculated InSb Surface Reconstructions and Evidence of Surface Phase Coexistence	61
4.3.2	As-Sb Intermixing and As-Induced Roughening on the InSb Surface	68
4.4	Conclusions	80
CHAPTER 5 Modifying the Surface of InAsSb with Bi as a Surfactant		82
5.1	Introduction.....	82
5.2	Experimental Procedure.....	83
5.3	Results and Discussion	85
5.3.1	Decreased Sb Incorporation Caused by Bi Surfactant.....	85
5.3.2	Model for Bi-Catalyzed Formation of InAs Formation	89
5.4	Conclusions	93
CHAPTER 6 Conclusions and Future Work		94
6.1	Key Findings	95
6.2	Prospects for Future Research	97

APPENDIX A Selected MATLAB Script for Finite Temperature Surface Energy	
Calculations.....	102
APPENDIX B Schematics of Sb:InAs Surface Reconstructions	107
REFERENCES.....	114

LIST OF TABLES

Table 3.1. Island and Divot Coverages of Sb:InAs and Pure InAs Surfaces.....	48
Table 4.1. RHEED Pattern of InSb After Exposure to As and Sb Fluxes.	74
Table 5.1. Growth Conditions for InAsSb Films Grown on GaSb Substrates.....	84

LIST OF FIGURES

Figure 3.1. Schematics of atomic substitution on surface reconstruction structural prototypes. Some atoms are duplicated and some are omitted for clarity. Substitution on duplicated equivalent sites is only highlighted once.	28
Figure 3.2 a. RHEED phase diagram of a static InAs (001) surface at 425°C under various Sb and As ₂ fluxes. b&c. Selected RHEED patterns of InAs exposed to various fluxes. c. branched pattern under 9.3×10^{-7} torr Sb. d. $c(4 \times 4)/n \times 3$ under 9.3×10^{-7} torr Sb and 5.6×10^{-6} torr As ₂ with lines illustrating $\times 2$ (for the $c(4 \times 4)$) and $\times 3$ periodicity. Solid lines indicate integral streaks, dotted lines indicated $\times 3$ streaks, and dashed lines indicate $\times 2$ ($c(4 \times 4)$) streaks.	32
Figure 3.3 0K DFT surface reconstruction phase diagram of Sb:InAs with atomic substitution in surface dimers. Solid lines separate structural transitions while dotted lines separate configurational changes for a given structure. Unlike the RHEED phase diagram (Figure 3.2a), very little of the diagram is occupied by a 4×3 reconstruction.	34
Figure 3.4. 0K DFT surface reconstruction phase diagram of Sb on InAs (001) allowing Sb to occupy both dimer and subsurface sites. Solid lines separate reconstruction prototypes and dotted lines separate compositional configurations of a given reconstruction. Unlike Figure 3.3 much of the phase diagram is occupied by 4×3 reconstructions, which better agrees with the RHEED results in Figure 3.2a.	36

Figure 3.5. Schematics of selected group-V-rich surface reconstructions from the phase diagram in Figure 3.4. For clarity, some atoms are removed, some atoms are duplicated, and the $c(4\times 4)$ unit cell is outlined.....	37
Figure 3.6. STM image of an Sb-terminated InAs surface prepared by depositing 1.0 ML In on InAs before exposure to an Sb BEP of 7.8×10^{-8} torr.	44
Figure 3.7. Filled state ($-2.7\text{ V}\leq V_{\text{bias}}\leq -2.3\text{ V}$) STM images of InAs surfaces prepared by MBE under various growth conditions. a. 405°C , pure InAs; b. 405°C , 0.1 ML Sb deposited; c. 425°C , pure InAs; and d. 425°C , 0.1 ML Sb deposited. All samples display $\beta 2(2\times 4)$ dimer rows.	48
Figure 3.8. Dual bias STM images of Sb deposited on InAs at 425°C . a. filled state (-2.7 V) b. empty state (2.7 V).....	49
Figure 3.9. a: DFT 0K surface reconstruction phase diagram of Sb on InAs at constant $\mu_{\text{As}}=-140\text{ meV}$. b: schematics of dimer site occupancy in the stable $c(4\times 4)$ configurations with cells outlined.	50
Figure 3.10. DFT simulated filled state STM images of $c(4\times 4)$ configurations.	51
Figure 3.11. Schematic of island and divot formation. a. InAs $\beta 2(2\times 4)$. b. left: As and In are removed to expose an As-terminated surface. right: As and In are added to create an As-terminated surface. c. Sb and In are distributed over the surface to create $c(4\times 4)$ reconstructions.	52
Figure 4.1. Schematics of surface reconstruction structural prototypes with sites where substitution is allowed are highlighted. Some atoms are duplicated and some are omitted for clarity. Substitution on duplicated equivalent sites is only highlighted once.	58
Figure 4.2. a. Calculated surface energies of InSb (001) as a function of Sb chemical potential from DFT at 0K (curves) and MC at 700K (points). b. Schematics of InSb (001) surface reconstructions.	63

Figure. 4.3. a. Filled state (-2.7 V) STM image of InSb after exposing 1.0 ML of In to Sb at 395°C. A few c(4x4)-like regions are circled. b. A-(1x3) RHEED pattern for this sample. Primary and secondary streaks are marked with solid and dashed lines, respectively. 66

Figure 4.4. Top: 0K DFT surface reconstruction phase diagram of As:InSb as a function of As and Sb chemical potentials. Bottom: schematics of the As-containing reconstructions on the DFT phase diagram. Some atoms are removed and some atoms are duplicated for clarity. 71

Figure 4.5. Schematic of how As₂ and Sb fluxes were applied for the experiments at 330°C summarized in Table 4.1..... 75

Figure 4.6. Plot of A-(1x3) intermediate streak spacing at 425°C as a function of As₂/Sb BEPR. Inset illustrating which streaks were measured with dashed lines for fractional streaks and solid lines for primary streaks. Error bars are \pm one standard deviation in the measurement of the streak spacing. The roman numerals refer to selected series of experiments from Table 4.1. Series i was conducted with constant Sb flux of 1.26×10^{-6} torr and increasing As₂ flux. Series ii was conducted with constant Sb flux of 7.84×10^{-7} torr and increasing As₂ flux. Series iii was conducted with constant As₂ flux of 1.35×10^{-7} torr with decreasing Sb flux. 77

Figure 5.1. (004) Reciprocal space maps of series A films with Bi fluxes noted. S denotes the GaSb substrate and F denotes the InAsSb film..... 87

Figure 5.2. Plots of InAsSb film composition vs Bi flux for series A and series B. While these data are plotted together, the Bi BEPs were measured in different chambers and might vary slightly with respect to each other. 88

Figure 5.3. Plots of RBS spectra of series A as a function of Bi BEP. The simulated curve and its elemental components are included for the samples grown without Bi. The channel at which Bi would be observed is marked by a dotted line..... 89

Figure 5.4. Schematic of growth processes at the surface of InAsSb [82]. a. Deposition. b. Desorption. c. Removal of Sb by As. d. Sb segregating to the surface by swapping places with As. 90

Figure B.1. 0K surface reconstruction phase diagram of Sb:InAs system over a limited chemical potential range and schematics corresponding to the labels on the diagram. *see Figure B.3. +see Figure B.4. 108

Figure B.2. 0K surface reconstruction phase diagram of Sb:InAs system over a limited chemical potential range and schematics corresponding to the labels on the diagram. *see Figure B.3. + see Figure B.4. # see Figure B.1. 109

Figure B.3. 0K surface reconstruction phase diagram of Sb:InAs system over a limited chemical potential range and schematics corresponding to the labels on the diagram. +see Figure B.4. # see Figure B.1. 110

Figure B.4. 0K surface reconstruction phase diagram of Sb:InAs system over a limited chemical potential range and schematics corresponding to the labels on the diagram. +see Figure B.6. # see Figure B.5. 111

Figure B.5. 0K surface reconstruction phase diagram of Sb:InAs system over a limited chemical potential range and schematics corresponding to the labels on the diagram. +see Figure B.6. # see Figure B.4. * see Figure B.3. 112

Figure B.6. 0K surface reconstruction phase diagram of Sb:InAs system over a limited chemical potential range and schematics corresponding to the labels on the diagram. +see Figure B.5. # see Figure B.4. 113

LIST OF APPENDICES

APPENDIX A Selected MATLAB Script for Finite Temperature Surface Energy	
Calculations.....	102
APPENDIX B Schematics of Sb:InAs Surface Reconstructions	107

LIST OF ABBREVIATIONS

ARL Army Research Laboratory

BEP beam equivalent pressure

BFM beam flux monitor

CASM Cluster Assisted Statistical Mechanics

DFT density functional theory

HRXRD high resolution x ray diffraction

MBE molecular beam epitaxy

MC Monte Carlo

MEE migration enhanced epitaxy

ML monolayer

ML/s monolayers per second

RHEED reflection high energy electron diffraction

RBS Rutherford backscattering spectrometry

STM scanning tunneling microscopy

UHV ultra high vacuum

UM University of Michigan

VASP Vienna *ab initio* simulation package

XRD x ray diffraction

ABSTRACT

Surface Phase Stability and Surfactant Behavior on InAsSb

by

Evan M. Anderson

Chair: Joanna M. Millunchick

InAsSb and related III-As/III-Sb heterostructures are of technological interest for applications in long wavelength infrared optoelectronic devices. However, there remain challenges to growing high quality material for these devices due to the complex interaction between As and Sb. While this interaction has been the subject of intense study, little work has focused on how As and Sb behave at the material surface with even fewer investigations into the atomic scale details of the InAsSb surface. This is a major gap in current knowledge because these materials are typically grown via vapor deposition methods, one atomic layer at a time. Thus, all processes impacting the growth of the crystal and its resultant properties occur at the surface. Despite this, the atomic scale details of the surface phases and processes impacting the Sb-As interaction have not previously been reported. This dissertation investigates the surface As-Sb interaction at an atomistic scale and its modification through different surface chemistry to be used as a guide for future experiments to improve the quality InAsSb of heterostructures by manipulating the surface phase during growth. In order to accomplish this, first principles calculations and experiments are used to investigate this system from three complimentary vantage points. First, the influence of Sb on the InAs surface and the stable surface phases of this system are investigated. Next, a similar approach is used on the

opposite compositional extreme of the InAsSb system: As on the surface of InSb. Finally, the interaction of As and Sb is modified by the use of Bi as a surfactant during growth of InAsSb films.

The interaction between As and Sb is found to be driven through the formation of surface phases and Bi is found to alter this interaction. Phase diagrams of both Sb on InAs and As on InSb show that As and Sb are driven to intermix through the formation of alloyed surface phases. Additionally, these phases range from having bulk-like stoichiometry to being highly As or Sb rich for the full InAsSb compositional range, indicating that surface stoichiometry is a controllable parameter for InAsSb growth. Sb is shown to intermix with the InAs surface by roughening the surface in a process driven by a phase transition. This interaction between Sb and InAs is stronger than previously thought, which has implications for the crystal growth problem of compositional broadening of the interfaces of III-As/III-Sb heterostructures. Finally, applying Bi to the surface of InAsSb during growth shows that modifies the interaction between As and Sb by catalyzing the formation of InAs, which decreases Sb incorporation. The results of this dissertation lay the foundation for optimization of the crystal growth surface in order to improve the properties of InAsSb and arsenide/antimonide heterostructures.

CHAPTER 1

Introduction

InAsSb is of technical interest for long wavelength infrared (LWIR) applications because it is a III-V semiconductor with a sufficiently narrow direct bandgap corresponding 12.5 μm , the longest wavelength of the LWIR range [1,2]. Thus, InAsSb can be developed as a viable replacement for current HgCdTe and strained layer superlattice (SLS) technology. HgCdTe devices have challenges with compositional inhomogeneity [3,4], expensive substrates [5], and prominent Auger recombination requiring the device to be cooled [3]. InAs/GaSb SLSs have advantages over HgCdTe in that III-V infrastructure is better developed than II-VI technology, though have problems with short carrier lifetimes [6]. InAsSb also exhibits high carrier mobility, which would make it suitable for high electron mobility transistors [7]. Additionally, because Earth's atmosphere allows transmission of radiation in the LWIR range, InAsSb would be suitable for thermophotovoltaic applications [8,9]. Despite the expected advantages such as the requisite bandgap [1] and high carrier lifetime in an InAs/InAsSb superlattice [10], growth of high quality InAsSb presents several technical challenges. InAsSb exhibits a miscibility gap and will phase separate under certain growth conditions [11,12], there are no lattice matched substrates for the compositions needed for LWIR, and compositional control in mixed anion semiconductors is not straight forward. Thus, there is much need to characterize and optimize InAsSb growth by molecular beam epitaxy (MBE).

The challenges in growing high quality InAsSb and arsenide/antimonide heterostructures for use in electronic devices are a result of the complicated interaction between As and Sb. This

interaction has been well documented in the literature [13–28]. However, past studies have primarily focused on microscopic and macroscopic effects such as phase separation, compositional broadening, structural quality of the material, and the measurement of electronic properties of the grown material or heterostructure. Additionally, these investigations have focused on bulk-like material, rather than the surface of the material before, during, or after growth. This is a major gap in current knowledge, as these materials are typically grown by vapor deposition methods, so all growth processes occur at the surface. Thus, identifying the bonding and arrangement of atoms at the surface, or surface reconstructions, is crucial for explaining crystal growth phenomena.

There have been many surface studies of the III-V semiconductors, including modifying the surface energy by the use of Bi as a surfactant [29–31] and investigations into the atomic scale structure of both InAs [32] and InSb [33,34]. However, there have been few studies focused on examination of the surface of the InAsSb system [13,20,25,28,35,36]. Of those, even fewer have characterized the atomic details of the surface. The only existing atomic scale reports of this system involved InAs under Sb-rich conditions, rather than the full compositional range [35,36]. There are no previous reports of the atomic scale behavior of As on InSb or the use of Bi as a surfactant on InAsSb.

This dissertation investigates the surface As-Sb interaction at an atomistic scale and its modification through different surface chemistry. To explore the thermodynamics of this interaction, an approach combining *ab initio* total energy calculations and a cluster expansion formalism with experimental surface characterization is employed. The study of the InAsSb surface is divided into segments at opposite ends of the compositional spectrum. Directly studying the random alloy at varying lattice parameters and compositions via calculations would be computationally expensive to the point of being infeasible at present. Additionally, many devices are created by growing an antimonide layer on top of an arsenide layer (or vice versa),

resulting in interactions of Sb on a III-As surface or As on a III-Sb surface. Thus, calculations are conducted focusing on the two compositional endpoints of the InAsSb system: Sb on InAs and As on InSb, to guide and be confirmed by experiments. These have yielded phase diagrams of the surface to guide future experiments to control the Sb-As interaction during InAsSb film and III-As/III-Sb heterostructure growth. Experimentally, the surface is further modified by the use of Bi as a surfactant, which is shown to decrease the strength Sb-As intermixing when present on the growth surface.

1.1 Overview and Organization

In this dissertation, both computations and experiments were used to investigate the InAsSb surface by examining Sb:InAs, As:InSb, and Bi:InAsSb. Density functional theory (DFT) total energy calculations combined with a cluster expansion approach and a genetic fitting algorithm are used to calculate surface reconstruction phase diagrams for Sb:InAs and As:InSb. Reflection high energy electron diffraction (RHEED) and scanning tunneling microscopy (STM) were used to confirm the calculated phase diagrams. High resolution x-ray diffraction (XRD), RHEED, and Rutherford backscattering spectrometry (RBS) were used to explore the influence of a Bi surfactant on film quality and Sb incorporation in InAsSb.

This dissertation is organized into several chapters and appendices discussing the work outlined above. Chapter 1 presented the motivation and outline of this work. Next, Chapter 2 provides background information and a detailed description of the computational and experimental techniques that were utilized to complete this dissertation. This includes background information about the influence of surface reconstructions and surfactants on semiconductor growth. The background information is followed by the procedures used to prepare samples using molecular beam epitaxy (MBE) and the characterization of these surfaces with RHEED and STM. The use of

DFT and MC calculations and the surface energy calculations to produce surface reconstruction phase diagrams is discussed last.

The first compositional endpoint of InAsSb examined in this dissertation is Sb on InAs. Chapter 3 examines the thermodynamic stability of Sb-terminated reconstructions and effect of Sb on the InAs (001) surface. Experimental and computational phase diagrams of the Sb-terminated surface reconstructions are discussed. DFT calculations indicate that many reconstructions are stabilized by subsurface Sb, indicating that Sb-As intermixing is energetically favorable. Additionally, the phase diagram includes both highly anion rich and nearly stoichiometric alloyed surface reconstructions that range from being completely As-terminated to completely Sb-terminated. This suggests that InAsSb could be grown under varying surface stoichiometry to improve material quality. Finally, Sb is shown to roughen the surface of InAs in a process driven by the formation of Sb-rich surface reconstructions, indicating that Sb interacts with the surface more strongly than previously thought. This roughening provides a mechanism by which the widely observed interfacial broadening in III-As/III-Sb heterostructures occurs.

The next compositional endpoint of the InAsSb is explored in Chapter 4, which examines the thermodynamic stability of the pure InSb (001) surface and the effect of As on it. DFT and MC calculations newly predict 2×4 and $c(4\times 4)$ reconstructions to be stable on InSb. This results in a phase diagram that more completely captures experimental results than a previous report in the literature. Additionally, STM shows that the widely observed, but poorly understood $A-(1\times 3)$ RHEED pattern is the result of coexistence between different reconstructions, rather than an otherwise unidentified reconstruction. DFT calculations reveal further evidence of a thermodynamic driving force for Sb-As intermixing through the formation of reconstructions stabilized by subsurface As. RHEED experiments indicate that the $A-(1\times 3)$ RHEED pattern is stable under concurrent As and Sb fluxes and gradually changes with increasing As/Sb ratio. This supports

the conclusion that the $A-(1 \times 3)$ is the result of coexistence between surface phases. As is shown to roughen the surface through the formation of facets. Faceting is reversible; the surface can be smoothed by applying a sufficiently high Sb flux, which is evidence of Sb-for-As exchange under Sb-rich conditions.

Chapter 5 details experiments conducted on a more complex system: the effects of Bi as a surfactant during InAsSb thin film growth. Bi was found to decrease the amount of Sb incorporated in the InAsSb films without incorporating itself. Analysis of a kinetic model of anion incorporation indicates that Bi inhibits Sb incorporation by catalyzing InAs formation. Most of the work presented in Chapter 5 has been previously published [37].

Chapter 6 provides a summary of the work conducted, conclusions derived thereof, and prospective directions for future study of the InAsSb system. Finally, the appendices include an example MATLAB script for surface energy calculations and schematics of all surface reconstructions predicted to be stable for Sb:InAs.

CHAPTER 2

Background and Methods

This dissertation uses a variety of experimental and computational techniques to examine the interaction between As and Sb on semiconductor surfaces and the modification of this interaction through the use of Bi as a surfactant. This requires additional background information and detailed descriptions of the methods employed most often for this dissertation. First are brief summaries of surface reconstructions and surfactants, and their influence on crystal growth. This is followed by background information and methodology for the experimental and computational techniques employed. Finally, the thermodynamics of surfaces are discussed.

2.1 Surface Reconstructions

A surface is essentially a large scale defect when compared to the perfect periodic order of a crystalline material. In the bulk crystal, atoms are surrounded by neighbors at optimal spacing to satisfy all molecular bonds, which is a low energy state. In a III-V semiconductor with zincblende structure, this bonding results in each group-III atom, such as In, bonded to 4 group-V atoms, such as Sb, forming the vertices of a tetrahedron. Alternatively, this structure can be imagined as the group-III atoms occupying the vertices and the group-V atom occupying the center of the tetrahedron. At a surface however, some of these atoms are missing, resulting in a high energy state caused by unsatisfied bonds. For a (001) surface, these atoms form pairs, known as dimers, to reduce the number of unsatisfied bonds by creating strained bonds with their nearest neighbors.

These dimers align along either [110] or [1-10] and form arrangements known as surface reconstructions.

Because semiconductors are typically grown through vapor deposition methods, such as MBE, all growth processes occur at the surface, making understanding the atomic details of the surface crucial to growing high quality material. Indeed, surface reconstructions have been observed to influence the properties of a variety of III-V semiconductors. In one theoretical study involving GaNAs, the strain fields associated with surface dimers reduce the N-for-As substitutional energy and allow alloying to occur [38]. Sites beneath the dimers are under compressive strain and can accommodate smaller solute atoms, while sites between the dimers are under tensile strain and are preferred by larger atoms. Some reconstructions offer only a limited window of chemical potential space that can be used for incorporation, such as in GaSbBi, where the $\beta(4\times3)$ reconstruction does not include any Bi until high Bi chemical potential [39] and has only a narrow range of chemical potential space that accommodates Bi without forming droplets. In GaAsBi, Bi is more easily accommodated by a 2×1 surface than a 1×3 surface, resulting in greater Bi incorporation with the 2×1 reconstruction [40].

In addition to modifying incorporation, the surface reconstruction can influence the ordering of alloying elements. The strain-induced site selective behavior of solute atoms [38], as discussed above, would naturally lead to ordering since the surface dimers are periodically arranged. Indeed, earlier *ab initio* calculations revealed CuPt ordering would arise in $\text{Ga}_{0.5}\text{In}_{0.5}\text{P}$ with $\beta 2(2\times4)$ or $c(4\times4)$ reconstructions [41]. This has similarly been predicted for the $c(4\times4)$ reconstruction on InGaAs [42]. More recently, ordered domains were observed in GaAsBi and were attributed the same anion segregation under a 2×1 surface to explain their presence despite low Bi concentration [43].

Surface reconstructions that contain antisites are well known to exist through the observation of surface reconstructions with double-anion layers, such as the 4×3 reconstructions on AlSb and GaSb [44] and the $c(4\times 4)$ on InAs [32]. Due to the broken bonds on the surface, formation of antisites at the surface have a relatively low energy penalty compared to formation in the bulk [45]. Given that surface reconstructions have been observed to influence incorporation and ordering, certain surface reconstructions might be able to inject point defects as well by kinetically trapping these otherwise energetically unfavorable defects.

2.2 Surfactants in Semiconductor Growth

In the context of MBE growth of semiconductors, a surfactant is an element that is applied to the surface to modify it without incorporating. Originally, surfactants were used in semiconductor growth to suppress Volmer-Weber and Stranski-Krastinov growth, which produce rough surfaces, and promote Frank-van de Merwe growth, which produces flat surfaces [46]. There are additional benefits to semiconductor growth with a surfactant. For example, segregation of alloying elements can be decreased by the use of a surfactant during growth, such as using H to decrease Ge segregation in Si [47]. Surfactants can also reduce the segregation length of constituent elements and decrease surface roughness, such as in the case of Sb used as a surfactant on GaN. Bi is often used as a surfactant in III-V materials because strongly surface segregates under typical growth conditions, though it has not previously been used for InAsSb. The use of Bi as a surfactant will be discussed in further detail in CHAPTER 5.

2.3 Molecular Beam Epitaxy

Molecular beam epitaxy (MBE) was developed by A.Y Cho and J.R. Arthur in the late 1960's to study surface-vapor interactions [48]. All samples were prepared on (001) oriented InAs or GaSb substrates in a solid source MBE chamber using a standard effusion cell for In and valved

cracking cells for As and Sb. In rates were measured using standard reflection high energy electron diffraction (RHEED) oscillations, and As_2 rates were measured with group-V limited RHEED uptake oscillations [49,50], or beam flux measurements. Beam equivalent pressures (BEPs) for both As_2 and Sb were measured using a retractable ion gauge placed in front of the substrate manipulator. The substrate temperature was measured using a low temperature optical pyrometer.

2.3.1 *Beam Flux Measurement*

Beam flux measurement (BFM) is a widely used method to determine the fluxes used during MBE growth. For this dissertation, BFM was conducted to acquire As, Sb, Bi, and occasionally In beam equivalent pressures (BEPs), reported in units of torr. In each case, the BFM was allowed to outgas before recording measurements for at least 10 minutes after turning on the ion gauge. For a given element, the BFM was exposed to a flux of that element for at least one minute before the flux was removed and the BFM allowed to return to baseline pressure. This base pressure was recorded before exposing the BFM to a flux again and recording the measured pressure. This base pressure for a given element was subtracted from each measured flux to calculate the BEP in units of torr. Sb and As beam flux measurements were recorded in series of increasing valve positions, i.e. increasing fluxes.

2.3.2 *RHEED Patterns and Oscillations*

Reflection high energy electron diffraction is a valuable diagnostic tool for crystal growth via MBE. In this dissertation, RHEED was conducted using 15 keV electrons and a filament current of 1.5 A. The RHEED pattern was displayed on a phosphor screen. Images of the pattern were captured and the specular spot intensity were monitored using a CCD camera and k-Space Associates software to acquire real-time data from the growth surface.

Rates from uptake oscillations were measured by monitoring the periodic change in the intensity of the RHEED specular spot. The spectral spot is the result of the electrons that are reflected off of the substrate without diffracting. As material is deposited, the surface alternates between rough and smooth. Starting with a perfectly flat surface, the spectral spot will be brightest. While material is deposited, brightness decreases until it reaches a minimum corresponding to half a monolayer of new material, which is when the surface is roughest. With continued deposition, the RHEED brightness increases until a complete monolayer has been deposited. Tracking the brightness over time yields a damped sine wave, hence the title "oscillations". The oscillations are damped because each subsequent layer is imperfect: atoms do not necessarily incorporate as a complete layer at a time, so material is typically annealed after growth to allow atoms to diffuse and correct these defects. The measured deposition rate is the average frequency of the oscillations in ML/s. For a (001) surface of a material with a zincblende structure, a monolayer is half the thickness of a unit cell, which makes the conversion to $\mu\text{m/hr}$ trivial.

Uptake oscillations were conducted differently for group-III and group-V elements, but with important similarities. Rates were measured with the substrate at the same temperature used to grow the buffer layer, which is approximately 475°C for InAs (for In and As rates) and approximately 380°C for InSb (for Sb rates). Since the substrate is typically held under a group-V overpressure, measuring In oscillations only required opening the In shutter and tracking the RHEED intensity while maintaining a V/III flux ratio of approximately 2.

Group-V oscillations are more complicated than group-III oscillations and have been reported in the literature for As [50] and Sb [49]. All As-limited uptake oscillations were conducted in the following manner for this dissertation. First, As overpressure is removed by closing the valve and shutter. Next, up to 10 MLs of Indium are deposited. After a pause of several seconds, the substrate is exposed to the desired As flux, controlled by the valve position. These oscillations

roughen the surface, so they are usually much dimmer on the RHEED screen than group-III oscillations, but the RHEED brightness typically recovers once all of the excess group-III material has been consumed. Material is grown for 1 minute or more between attempts at oscillations to smooth out the surface.

Sb-limited oscillations proceed similarly to As-limited oscillations, but require additional steps. The first steps are to use a new InAs substrate, desorb it, and grow an InAs buffer layer of approximately 500 nm at 470-480°C with an In rate of about 0.5 ML/s. These parameters have not been tested in detail, but provide a smooth InAs surface. However, this step might be unnecessary if a sufficiently thick InSb layer (1 μm or more) is grown. After annealing, the substrate must be cooled to 380-400°C, at which point the As valve and shutter are closed. Next, the InSb is grown using migration enhanced epitaxy (MEE) to start. The purpose of MEE is to deposit a monolayer of each constituent element separately, starting with In. This allows the In enough time to diffuse and cover the surface before adding Sb to create an abrupt interface. After depositing In, a monolayer of Sb is deposited, followed by growing an InSb film normally, that is with both In and Sb open. However, the MEE step might be unnecessary if a sufficiently thick layer of InSb is grown. The target Sb rate for this film is 0.7-1 ML/s with an In rate=0.5 ML/s to grow InSb. The Sb rate is estimated based on previous Sb rates and BEP measurements. After growing InSb, the film is annealed either without overpressure or with low Sb overpressure, to avoid accumulating polycrystalline Sb on the surface. Sb oscillations are usually acquired after several cycles of growing InSb and annealing, as this likely smoothes out the surface. The cryogenic pump is turned off during Sb oscillations because it creates noise in the RHEED intensity at about 1.2 Hz that tends to obscure the weak Sb oscillations.

2.4 Scanning Tunneling Microscopy

Scanning tunneling microscopy (STM) was invented by G. Binnig and H. Rohrer in 1981 to investigate surfaces over areas less than 10 nm in diameter [51]. All STM imaging in this dissertation was conducted in an STM under UHV conditions. Each sample was transferred from the MBE chamber after growth to the STM chamber *in vacuo*. Samples were imaged within 24 hours of growth in the MBE chamber to ensure that the features being imaged were the result of the growth and not molecules adsorbed to the surface after the sample was left in the buffer chamber. All samples were imaged at approximately room temperature with a tungsten tip under a constant current of 0.1 nA and varying bias voltages.

2.4.1 Measurements on STM Images

The SPIP software was used to conduct measurements of the features on STM images. This includes the area covered by divots and islands on STM images of InAs and InAs after exposure to Sb and the distance between rows on STM images of InSb and InAs. For the island and divot measurements, the raw data was loaded into SPIP followed by Fourier filtering to remove periodic features, such as surface dimer rows, and make non-periodic features more apparent. From here, the particle and pore detection feature was used so the software could identify islands and divots, respectively. This was accomplished by setting the maximum (minimum) height threshold for divots (islands) and manually deselecting false positives that arose from scanning artifacts such as noise or tip changes. This yielded the area covered by divots and islands in each image, which was converted to a coverage and averaged across all images for each experimental condition. Distances between rows on InSb were determined by measuring the distance between several rows, dividing by the number of rows traversed, and averaging these measurements.

2.5 Calculations

2.5.1 Procedure for DFT Calculations and Cluster Expansion

The 0K surface reconstruction phase diagrams in this dissertation were produced using DFT calculations as implemented by the Vienna *ab initio* simulation package (VASP) [52] under the local density approximation [53] with ultrasoft pseudopotentials [54]. A plane wave cutoff energy of 350 eV and a density of 144 k -points per $(2\pi)^2/a^2$ in-plane reciprocal area and 1 k -point normal to the surface were used for all surface slab calculations. Bulk phase calculations of InAs, InSb, Sb, As, and In were conducted with 12 k -points in each direction. These conditions yielded a relaxed bulk InAs lattice parameter of 6.01 Å and a bulk InSb lattice parameter of 6.43 Å. Surface energies were calculated from surface cells consisting of 5 ML of InAs or InSb terminated by surface reconstructions reported for InAs [32] or InSb [34], namely variants of the 2x4, 4x3, c(2x6), and c(4x4) reconstructions. The 2x1, which has been predicted for Bi:GaAs [55] and Bi:GaSb [39], was also considered. The InAs $\zeta(4x2)$ was used as an In-rich reference. The bottom As or Sb layer of each cell was terminated with pseudohydrogen atoms with 0.75 electrons to prevent charge buildup and satisfy dangling bonds. The pseudohydrogen atoms and bottom InAs or InSb monolayer were fixed to the calculated bulk lattice parameter to approximate a bulk substrate, while the remaining atoms were allowed to relax.

Generating an alloyed phase diagram from first principles requires a large number of computational expensive calculations. In order to decrease the computational cost, the computational surface reconstruction phase diagrams discussed in this dissertation were calculated by using a combined *ab initio* approach (VASP) [52] and a cluster expansion formalism with a genetic fitting algorithm implemented by the Cluster Assisted Statistical Mechanics (CASM) code [56]. Starting with basic surface reconstruction prototypes, such as those of InAs [32,35] and

InSb [34], compositional variation at the surface is investigated by allowing In, As, and Sb atoms to substitute on various atomic sites of the given reconstruction prototypes. CASM is run to generate a cluster expansion enumerating all symmetrically unique configurations. A subset of these configurations are selected for DFT calculations, which are then used as inputs for CASM's fitting algorithm. CASM predicts which configurations should be the lowest energy for a given composition. Any of these predicted lower energy configurations that have not yet been calculated with VASP are then run in VASP. This process is repeated until no new configurations are predicted to have lower energy. Using CASM allows for the prediction of which surface configurations are stable using only a few hundred DFT runs, out of hundreds of thousands of possible configurations, and greatly reduces the computational resources needed. The end goal is to create surface reconstruction phase diagrams of Sb on the (001) surface of InAs (Sb:InAs) and As on the (001) surface of InSb (As:InSb). This involves constructing cells with slab geometry for each likely structural prototype and each atomic configuration allowed on those prototypes. The procedure described in this section is pragmatic; more rigorous treatments of the cluster expansion and the thermodynamics of surfaces at 0K and finite temperature are presented in John Thomas's dissertation [57].

The first step is to obtain equilibrium energies for all elements, except for pseudohydrogen, which is treated differently, and equilibrium energies and lattice parameters for all compounds involved in the simulations. In this work, solid phases of As, In, Sb, InAs, and InSb were calculated. First a primitive cell for each element must be constructed; In is body centered tetragonal and As and Sb are trigonal, but with different lattice parameters. In the POSCAR file, the atoms are placed in the correct fractional coordinates, but with a lattice parameter that is somewhat far from the equilibrium spacing. This will prevent the atoms from getting stuck in a local energy minimum. Since these are small cells of only two atoms each, they will run very

quickly. Next a relaxation run is conducted by allowing the cell to change size. The output from this will provide the equilibrium formation energy. InAs and InSb both have the zincblende structure, but the procedure will be similar. The final outputs that are needed are the total energy, which is necessary for calculating surface energies to generate the phase diagram and the lattice parameter, which is necessary to build the slabs for the simulation cells.

Once the bulk energies have been obtained, surface slabs can be built involving layers of InAs or InSb, terminated with pseudohydrogen atoms, and with a layer of vacuum. The vacuum is included so that the slab does not interact with its own image in the [001] (z direction) (there are periodic boundary conditions). Both the slab thickness and the vacuum thickness need to be selected through convergence testing. First a slab that is 1.5 monolayers (ML) of the semiconductor thick in the [001] is created. For a (001) cell, the x and y directions are [110] and [1-10], respectively. This cell contain one In, two group-V atoms, and four pseudohydrogen atoms, with the bottom In atom and bottom group-V atom positions fixed. The pseudo hydrogen atoms have 0.75 electrons each in order to satisfy the dangling bonds of the group-V atoms that would otherwise lead to static charge buildup. This surface slab is then run allowing all atoms to relax except for the bottom In and group-V atoms, keeping the cell size and shape fixed. This process is repeated for cells containing 2.5 ML, 3.5 ML, etc while keeping the absolute thickness of the vacuum layer constant. After these runs have been completed, the difference in cell energy from adding a monolayer of material is calculated. Once this change in energy equals the bulk energy of an In-V unit, the slab is thick enough to simulate bulk-like material.

Once the slab convergence has been completed, vacuum convergence proceeds similarly. Cells with the same number of atoms are run with different vacuum layer thickness, which is adjusted by increasing the magnitude of the z-direction vector. The AFLOW package [58] is useful for converting the cell from fractional ("direct") to Cartesian coordinates to make absolute

adjustments to the thickness of the vacuum layer and back to fractional coordinates to preserve relative atomic positions. As before with the layer convergence, the difference in energy between cells with increments in the vacuum thickness is calculated. For decreasing vacuum thickness, the point just before the change in energy is no longer approximately zero is the smallest vacuum layer that can be used. Thinner vacuum layers change the energy of the cell because the slab is able to interact with its own image in the z direction.

Once layer and vacuum convergence have been completed, reconstruction prototype cells can be constructed. In this work, existing surface reconstruction prototypes such as 2×1 , $\alpha 2(2\times 4)$, $\beta 2(2\times 4)$, $c(4\times 4)$, $h0(4\times 3)$ (and heterodimer-containing variants), $c(2\times 6)$, and $\zeta(4\times 2)$ were used. AFLOW was used to create larger surface slabs from the 1×1 cell used for the convergence testing. After creating the appropriately sized surface slab, the details of each reconstruction prototype were then created by adding and/or removing atoms as needed. Atoms that form dimers must be biased toward the formation of dimers by adjusting their positions closer to each other and away from bulk-like positions. Each prototype was then run in VASP with the bottom In, group-V, and pseudohydrogen atoms fixed in bulk positions (as determined from the calculated lattice parameter of bulk InAs or InSb cell relaxation), while the other atoms were allowed to relax.

Once the proper input files have been generated and the structural prototype cells have been relaxed, CASM can be run to begin the cluster expansion. Each prototype is designed to allow substitution of different atoms in the surface. For dimers attached to substrate In atoms, only Sb and As were allowed to substitute in the 2×4 , 2×6 , and 4×3 cells. In was not allowed to substitute in these sites because double layers of cations are not energetically favorable and the focus of this work was on anion-rich conditions, which is most typical of MBE growth. The double anion layer dimers, those on top of a layer of anions in the $h04\times 3$, $c(4\times 4)$, and $c(2\times 6)$ were allowed to

substitute In, As, and Sb atoms. Additionally for these reconstructions, Sb and As were allowed to substitute onto sites in the first subsurface anion layer. CASM will enumerate all of the symmetrically unique configurations of the given PRIM file that identifies the primitive reconstruction cell, all atomic positions of each species, and which atomic species are allowed to substitute. While CASM can be instructed to enumerate arbitrarily large supercells, that is, cells containing multiple primitive unit cells, this quickly becomes computationally untenable, first for DFT calculations, and later the sheer number of possible requires too much processing power and/or memory. Thus, in this dissertation the largest supercells considered had a surface area no more than 16 times that of the 1x1 surface slab used for convergence testing.

Once the symmetrically unique configurations have been enumerated, DFT runs of selected configurations can begin to provide a set of calculated ground state energies to be used as inputs for CASM's genetic fitting algorithm using leave-one-out cross validation. The first run should include the compositional extremes of the cluster expansion, in this work those are the completely Sb-, As-, and, when allowed, In- rich configurations. The first run of DFT calculations should also include configurations of intermediate surface compositions. Once these ground state energies have been calculated, the CASM fitting algorithm can be run to predict which configurations should have the lowest energy for a given composition, that is, the configurations that fall on the convex hull of energy vs. composition. This process is repeated until all configurations predicted to lie on the convex hull have been calculated in VASP. In this work, the fitting code was run to allow 120 clusters, 60 populations, a mutation bit of 6, and 60 generations per population. The contribution of each configuration's energy to CASM's fitting code was weighted using the following equation:

$$W = \exp\left(\frac{-D}{k_B T}\right) \quad (2.1)$$

where D is the configuration's distance in eV above the convex hull, k_B is Boltzmann's constant, and T is the highest temperature in K intended for subsequent MC simulations.

2.5.2 Monte Carlo

Grand canonical Monte Carlo (MC) simulations were conducted using a Metropolis MC algorithm from the CASM code [56]. In this work, all MC simulations were conducted using a 2D grid of 96x96 times the magnitude of the [110] with no replication in the surface normal direction. This size cell was selected so that 2x4, 4x3, 2x6, and c(4x4) primitive cells could be tiled to produce a square simulation cell with integer multiples of the primitive cell lattice vectors. Because the c(4x4) cell is rotated 45° relative to the other reconstructions, this number was rounded up to 34 from 33.9 for the c(4x4) primitive cell. All MC simulations were conducted with 5000 equilibration passes, in which data is not recorded, followed by an additional 5000 passes to record thermodynamic averages for each point in temperature-chemical potential space.

The MC simulations are run using code provided as part of CASM and additional details are available in the CASM documentation. CASM was designed to run Grand Canonical MC simulations, meaning temperature (T) and chemical potential (μ_{sb}) are controlled. Before the MC simulation can be run, a cluster expansion for the structural prototype of interest must be completed as described above, setting the reference configuration energies to zero and using Equation 2.1 for weighting the fitting code. CASM is limited to simulations of surface reconstruction prototypes that are compatible with VASP POSCAR files. For example, CASM cannot simulate surface of coexisting surface reconstructions, such as h0(4x3) and c(4x4), unless a cluster expansion were completed for a supercell such as that, though this would likely be too computationally expensive and would be limited to a highly ordered arrangement of these reconstructions.

Once a cluster expansion has been completed, the MC simulations may proceed. Metropolis Monte Carlo simulations cannot directly measure the free energy of a system, so free energy integration must be conducted to obtain a surface energy. This means that for a given simulated temperature, a zero configurational entropy reference state must be simulated in order to integrate meaningful surface energies from the out MC data. Thus, for a given temperature the chemical potentials sampled must include a sufficiently high or low chemical potential such that the surface is completely terminated by only one atomic species. This reference state need not be constrained by chemical potentials that would lead to phase changes under corresponding experimental conditions. For example, simulating an Sb chemical potential, μ_{Sb} , that would high enough to cause polycrystalline Sb to form on a real surface is an acceptable reference state for free energy integration if such a chemical potential is necessary to simulate a completely Sb-terminated surface.

2.6 Thermodynamics of Surfaces

Surface free energy is best described as the excess energy that results from the existence of a surface rather than ideal, bulk material. To minimize this energy, atom bond to each other in arrangements known as reconstructions. For a given material, different surface reconstructions exist in different regions of phase space, that is, different values of thermodynamic variables. For MBE growth of III-V semiconductors, the most important thermodynamic variables of surface reconstruction stability are temperature, pressure of the vapor phase of each element, and lattice strain, as these are the easiest to control experimentally in an MBE chamber. However, DFT and MC calculations are more easily interpreted through chemical potential rather than vapor pressure. While chemical potential cannot be directly controlled experimentally, for a given element, increasing (decreasing) substrate temperature and decreasing (increasing) the flux can effectively

decrease (increase) the chemical potential of that element at the substrate. Since MBE is conducted under UHV conditions, the relevant chemical potentials are those of the elements present in the film and any fluxes of material applied to the surface. Any other chemical species are assumed to exist in negligibly low concentrations.

2.6.1 0K Surface Energy

The surface energies of two different material systems, both consisting of In, As, and Sb, are investigated in this dissertation: Sb:InAs and As:InSb. The following description of surface energies at 0 K is adapted heavily from the work of John Thomas et al. [45,57,59], in which surface energy is more rigorously derived. The surface energies of all stable reconstructions can be calculated and plotted in a phase diagram using a MATLAB script modified from Appendix A of Adam Duzik's dissertation [60].

The following equations were used to calculate the surface energies for surface reconstructions of InAs with In, As, and Sb allowed at the surface. The equations for InSb with In, Sb, and As allowed at the surface similar, with the group-V atoms species reversed. Though there are three chemical species present in these, the analysis of this surface can be simplified by the following reference state:

$$\mu_{In} = \mu_{InAs} - \mu_{As} \quad (2.2)$$

Stated another way, Equation 2.2 indicates that μ_{As} is bounded by the formation of bulk In and bulk As at the surface for high and low values of μ_{As} , respectively.

A formation energy for each reconstruction can be calculated from the DFT-calculated energy, E_{DFT} , of the surface reconstruction simulation slab:

$$E_{Form} = \frac{E_{DFT} - e_{InAs}N_{In} - e_{As}(N_{As} - N_{In}) - e_{Sb}N_{Sb}}{A_{1 \times 1}n_{1 \times 1}} - \frac{E_H}{A_{1 \times 1}} \quad (2.3)$$

Because the simulation slab contains bulk-like atoms and the surface energy will be calculated relative to solid InAs, As, and Sb, several terms must be subtracted from E_{DFT} . Here, e_i is the DFT energy per atom or compound unit of i , which must be subtracted from E_{DFT} in proportion to the number of each atom or compound unit in the slab, N_i . In order to compare surface reconstruction cells of different sizes, the energy must be normalized by $n_{1 \times 1}$, which is the number of units of area ($|[110]| \times |[1-10]|$) occupied by the structural prototype (e.g. $n_{1 \times 1}=8$ for 2×4 and $c(4 \times 4)$), and $A_{1 \times 1}$, which is the area of a 1×1 surface slab. E_H is the energy from the pseudohydrogen-terminated bonds in the slab calculated from the energy of the 1×1 slab used for vacuum convergence as follows:

$$2E_H = E_{1 \times 1} - e_{\text{InAs}}N_{\text{In}} - e_{\text{As}}(N_{\text{As}} - N_{\text{In}}) \quad (2.4)$$

the factor of 2 arises because the 1×1 cell used for convergence testing is terminated on top and bottom with pseudohydrogen atoms.

The surface energy per unit area can then be calculated from E_{Form} as follows:

$$\gamma = E_{\text{form}} - \Delta\mu_{\text{As}}x_{\text{As}} - \Delta\mu_{\text{Sb}}x_{\text{Sb}} \quad (2.5)$$

where $\Delta\mu_i$ is the chemical potential of species i relative to e_i . In this case, bulk Sb forms at the surface when $\Delta\mu_{\text{Sb}}=0$, bulk As forms at the surface when $\Delta\mu_{\text{As}}=0$, and bulk In forms at the surface when $\Delta\mu_{\text{As}}=e_{\text{InAs}}-e_{\text{In}}-e_{\text{As}}$. $\Delta\mu_{\text{Sb}}$ can be arbitrarily small. In Equation 2.5, x_i is the surface excess quantity of species i , defined as follows:

$$x_{\text{As}} = \frac{N_{\text{As}} - N_{\text{In}}}{A_{1 \times 1}n_{1 \times 1}} - \frac{0.5}{A_{1 \times 1}} \quad (2.6)$$

$$x_{\text{Sb}} = \frac{N_{\text{Sb}}}{A_{1 \times 1}n_{1 \times 1}} \quad (2.7)$$

The 0.5 in Equation 2.6 arises to ensure that the size of the simulation cell does not impact the calculated surface excess, which should be independent of the number of bulk-like atoms simulated. To achieve this, a 3D cell containing the surface and some bulk-like atoms is

constructed. In this dissertation, this cell contains all of the simulated atoms except for the pseudohydrogen. All atoms in the cell are counted, but the atoms at the bottom most layer only count for half of an atom each. Thus, all In atoms and all As atoms are counted as whole atoms, except for those As at the bottom of the surface cell. Those lowest As atoms are counted as 1/2 of an atom to calculate an accurate surface excess concentration. The number of In atoms is then subtracted from the weighted number of As atoms to determine the As excess. Since the Sb atoms are only allowed at the surface, each Sb atom is counted toward the surface excess concentration. Without this weighting, or tapering of the surface cell, the surface slab thickness would depend on which atoms occupied the bottom, bulk-like layer of the cell. Thus, the surface excess would incorrectly be In-rich if the bottom atom were In, or As-rich if the bottom atom were As.

2.6.2 *Finite Temperature Surface Energy*

The following description of surface energies at finite temperatures is adapted heavily from the work of John Thomas et al. [57,61]. Phase diagrams calculated at 0 K, provide useful insights into the nature of certain thermodynamically stable phases, however, experiments are necessarily conducted at finite temperatures, which allows metastable phases to appear when higher energy phases are statistically accessible, or phases are stabilized by entropic contributions. MC calculations can be used to simulate surfaces at elevated temperatures. The finite temperature surface energies can be calculated by modifying the MATLAB script included in Appendix A.

The Grand Canonical MC simulations were each conducted at constant temperature, μ_{sb} , surface area, and total number of atoms at zero pressure. The surface free energy at a given point in phase space is not directly accessible from MC simulations, except for a point with zero configurational entropy, so a summation must be performed from this point. Thus, the simulations were run over a range of μ_{sb} sufficient to capture the range of chemical potentials between the

formation of bulk Sb and bulk In at the surface as well as to produce a completely Sb-terminated surface as a reference state. The Grand Canonical free energy could then be determined for a given μ_{Sb} as follows:

$$\Phi_{MC} = \Phi_{MC} - \sum_{j=1}^{N-1} \frac{(N_{\text{Sb}}^j + N_{\text{Sb}}^{j+1})(\mu_{\text{Sb}*}^j - \mu_{\text{Sb}*}^{j+1})}{2} \quad (2.8)$$

where Φ_{MC} is the energy output by the MC code, $\mu_{\text{Sb}*}$ is the Sb chemical potential as implemented by CASM, $\mu_{\text{Sb}*}^0$ is the Sb chemical potential that produced the completely Sb-terminated reference, and N_{Sb} is the number of surface sites occupied by Sb. Note that the sum proceeds from high to low μ_{Sb} . For Sb dimer substitution, the sum needs to be divided by 2 again to account for CASM treating N_{Sb} as the number of dimers rather than the number of atoms in this case. The internal energy of the system can then be calculated from $\Phi(\mu_{\text{Sb}})$ by adding the chemical contribution to the energy:

$$E_{MC}(\mu_{\text{Sb}*}) = \Phi_{MC}(\mu_{\text{Sb}*}) + N_{\text{Sb}}\mu_{\text{Sb}} \quad (2.9)$$

The chemical potentials used in CASM (denoted by an asterisk) are not referenced to the extremes of the formation of bulk Sb at the surface or the formation of bulk In at the surface. Before the surface energy can be calculated, the chemical potential needs to be referenced. For simulations allowing In and Sb substitution, this means subtracting $(2e_{\text{Sb}} - e_{\text{InSb}})$ from CASM's chemical potential. For simulations allowing Sb dimer substitution, this means subtracting $2e_{\text{Sb}}$ from CASM's chemical potential and dividing the difference by 2. With substitution of E_{MC} for E_{DFT} in Equation 2.3 and the result into Equation 2.5, the finite temperature surface energy can then be calculated as follows:

$$\gamma = \frac{E_{MC}(\mu_{\text{Sb}}) - e_{\text{InSb}}N_{\text{In}} - e_{\text{Sb}}(N_{\text{Sb}} - N_{\text{In}})}{A_{1\times 1}n_{1\times 1}} - \frac{n_{1\times 1}E_H}{A_{1\times 1}} - \mu_{\text{Sb}}x_{\text{Sb}} \quad (2.10)$$

CHAPTER 3

Interaction Between Sb and As on InAs Surfaces

3.1 Introduction

In order to simplify the problem of characterizing the atomistic details of the InAsSb surface, one compositional endpoint of the system, Sb on InAs, is examined first. There exist some reports in the literature of Sb and InAs. The complex interaction between As and Sb has been studied extensively because it presents challenges to growing high quality InAsSb and III-As/III-Sb heterostructures. For instance, As is commonly observed to displace Sb at typical growth temperatures [13–19]. The opposite effect, Sb-for-As exchange, has also been reported under certain conditions in GaAsSb [17] and InAsSb [20], such as at temperatures above the sublimation of the arsenides [13], though As-for-Sb exchange is more common [15–19]. Additionally, RHEED [25], X-ray diffraction (XRD) [23,62], and cross-sectional scanning tunneling microscopy (STM) [22] demonstrate that Sb surface segregates in InAsSb. It has been suggested that an excess of Sb atoms are weakly physisorbed on the surface during growth, with some fraction of the Sb incorporating into the growth front. Indeed, this segregation has been thought to be the cause of the widely observed interfacial broadening in III-As/III-Sb heterostructures where Sb is unintentionally incorporated into the arsenide layers [16,21–27]. One approach to mitigate this broadening is to expose the Sb-terminated layer to an As overpressure in the absence of an Sb overpressure. This “pre-soaking” step is thought to remove the physisorbed Sb and has been shown to improve interfacial abruptness [14]. However, the analysis does not take surface reconstructions

into account, such that the atomistic mechanism of interface broadening and surface segregation has not been fully determined.

Because III-V devices and films are typically grown by depositing vapor onto a crystalline substrate (e.g. through molecular beam epitaxy (MBE) or chemical vapor deposition), all crystal growth processes occur at the surface. Thus, understanding and controlling the quality of the growth by manipulating surface reconstructions is important for the quality of the film. The surface structure of a material is typically monitored using RHEED during crystal growth. InAsSb is often observed to have an $nx3$ RHEED pattern during growth [2,63,64], which indicates a highly group-V rich surface, though one report indicates that InAsSb can be grown under a more stoichiometric $2x4$ RHEED pattern [65]. However, few studies have been reported in the literature investigating Sb on InAs surfaces at the atomic scale [35,36]. Both used STM to examine the influence of applying Sb to the surface of InAs and one [35] included *ab initio* calculations, but they did not explore the full compositional range of both As and Sb on the surface.

In this chapter, a combination of experiments and *ab initio* calculations are used to characterize the atomic details of the InAs (001) surface in the presence of Sb. RHEED experiments and density functional theory calculations are compared to establish that intermixing between As and Sb in III-V semiconductors is thermodynamically driven through the formation of surface reconstructions that contain subsurface Sb and Sb-As heterodimers. These RHEED experiments and calculations, along with scanning tunneling microscopy show that the stoichiometry of an InAsSb surface can be controlled to range from being anion-rich to stoichiometric for a range of Sb compositions. Further STM imaging shows that a surface reconstruction transition from an As-terminated surface to Sb-terminated reconstructions roughens the surface by creating 2D islands and vacancy clusters (divots). The culmination of these results provides a guide for future work to

manipulate the growth surface reconstruction in order to improve the quality of InAsSb and III-As/III-Sb heterostructures.

3.2 Procedure and Nomenclature

3.2.1 MBE Growth, RHEED, and STM

The general procedure for MBE growth of these samples was discussed in Section 2.3. For this set of experiments, each sample was grown on (001) oriented InAs substrates. After oxide desorption, a buffer layer of at least 250 nm of InAs was grown at approximately 475°C with rates in monolayers per second of approximately $R_{\text{In}}=0.50$ or 0.75 ML/s and approximately $R_{\text{As}_2}=1.0$ or 1.5 ML/s to maintain a V/III ratio of approximately 2. After growing the buffer layer, each film was annealed under the growth As_2 flux for at least 10 minutes. All of these growths produced a streaky 2x4 RHEED pattern, as expected. After annealing, each sample was cooled to the temperature of interest under approximately $R_{\text{As}_2}=0.7$ ML/s, at which point the As valve and shutter were closed. The RHEED phase diagram was produced by observing the RHEED pattern of a static InAs surface (no In flux) held at 425°C and exposed to several series of increasing or decreasing As_2 and Sb fluxes. The flux of only one species at a time was modified during a given series. Between each series of RHEED experiments, 250 nm of InAs was grown under the same conditions as the initial buffer layer.

Samples intended for scanning tunneling microscopy underwent different processing than those used for the RHEED phase diagram after cooling to the temperature of interest. Some samples were prepared by depositing 0.5 or 1.0 ML In on InAs at 425°C prior to exposure to an Sb flux. These samples were then quenched to room temperature by shutting off the power to the substrate heater. Another set of samples were cooled to either 425°C or 405°C. Each sample was either quenched to room temperature immediately, or exposed to approximately 0.1 monolayer

(ML) of Sb at 0.1 ML/s before quenching. Scanning tunneling microscopy (STM) was conducted using an STM attached *in vacuo* to the MBE chamber. All images were acquired under a constant current of 0.1 nA with varying bias voltages.

3.2.2 Calculations

The general procedure for creating *ab initio* phase diagrams using VASP and CASM was discussed in Sections 2.5.1 and 2.6.1, while the details for Sb:InAs are discussed here. The surface compositions of the selected reconstructions were varied by allowing atomic substitution on surface sites on each structural prototype (Figure 3.1). Sb and As were allowed to occupy dimer sites on the 2x4 reconstructions; In substitution was not allowed because it has a high energy cost for these reconstructions. Supercells containing up to 2 primitive 2x4 cells were calculated. Because they are terminated by a double anion layer, two sets of cluster expansions were conducted for the 4x3, c(4x4), and c(2x6). In the first case, In, As, and Sb substitution was allowed on the dimer sites bonded to As atoms below. The dimer sites bonded to In atoms below only allowed As and Sb substitution. The c(4x4) was calculated with supercells containing up to 2 primitive unit cells. In the second case, Sb and As substitution was allowed on the subsurface anion sites, henceforth referred to as subdimer substitution. Only primitive c(4x4) cells were considered in this case due to the large number of compositional configurations. While a previous report predicts the Sb-terminated $\alpha(4x3)$ to be stable [35], preliminary calculations indicated that for the present work, only the $\beta(4x3)$ was stabilized by Sb, so the second cluster expansion of $\beta(4x3)$ proceeded by allowing only As-Sb substitution on the dimer and subdimer sites. The only configuration of the c(2x6) predicted to be stable was completely Sb-terminated, so only Sb-As dimer and subdimer substitution were allowed for the second c(2x6) cluster expansion. Supercells containing up to three primitive unit cells were considered for the 2x1 reconstruction with In, As, and Sb

substitution on the dimer sites. These supercells are considered to be ordered arrangements of reconstruction unit cells rather than larger reconstruction cells *per se* and would not be expected to produce unique RHEED patterns experimentally.

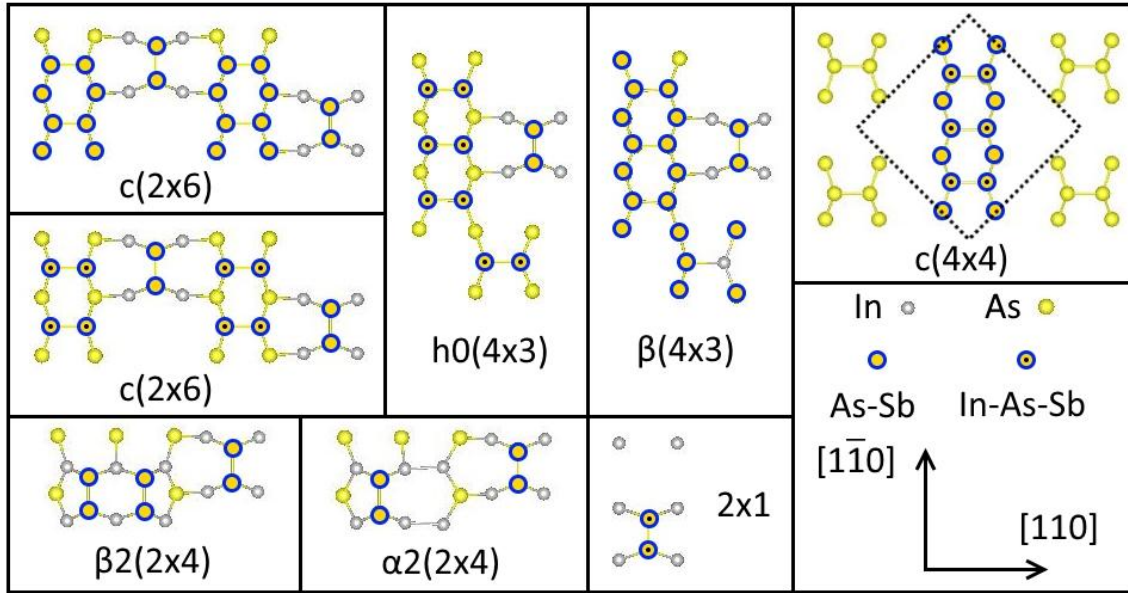


Figure 3.1. Schematics of atomic substitution on surface reconstruction structural prototypes. Some atoms are duplicated and some are omitted for clarity. Substitution on duplicated equivalent sites is only highlighted once.

3.2.3 Surface Reconstruction Nomenclature

To succinctly describe these surface reconstruction configurations, the following naming convention is used throughout this dissertation, adapted from that proposed by Duzik and Millunchick [55]. For a given structural prototype, such as $\alpha 2(2 \times 4)$, $\beta(4 \times 3)$, or $c(4 \times 4)$, the number after the root surface reconstruction refers to the number of Sb atoms occupying dimer sites in the configuration. A supercell configuration is denoted by dividing by the number of primitive unit cells in the reconstruction. For example, $\alpha 2(2 \times 4)_{5/2}$ contains 5 Sb atoms distributed over the dimer sites of 2 unit cells. The $c(4 \times 4)$, which can contain III-V heterodimers, requires additional nomenclature. Following the convention used in the literature [66], α refers to the presence of III-

V heterodimers in the $c(4\times 4)$ surface reconstructions. In our nomenclature, the number following α refers to the number of such heterodimers. Finally, reconstructions containing subsurface Sb atoms require additional nomenclature. The letter 's' is appended to the name after the number of dimer sites occupied by Sb (if any), followed by number of subsurface Sb atoms. For example, a $c(4\times 4)$ reconstruction with 3 In-Sb heterodimers and 7 subsurface Sb atoms is named $\alpha 3c(4\times 4)3s7$. The use of Greek letters in the 2×4 and 4×3 reconstruction prototypes follows long-established conventions in the literature.

3.3 Results and Discussion

The results of the investigation of the atomic-scale interaction between Sb and As on InAs surfaces are divided into three sections here. First, Section 3.3.1 compares RHEED experiments and DFT calculations. Monitoring the RHEED patterns of a static, and initially As-terminated, InAs surface exposed to Sb and As_2 fluxes indicates that the surface exhibits either an $n\times 3$ or $c(4\times 4)$ RHEED pattern under most fluxes. Density functional theory (DFT) calculations confirm these highly anion-rich reconstructions. The DFT calculations also provide evidence of a thermodynamic driving force for Sb-As intermixing through several reconstructions being stabilized by subsurface Sb and many other configurations containing Sb-As heterodimers. Additionally, the *ab initio* calculations predict that much of the phase diagram consists of stoichiometric or nearly stoichiometric 2×4 reconstructions ranging from completely As-terminated to Sb-terminated. In Section 3.3.2, this is confirmed through STM of an initially In-terminated surface that is exposed to Sb. Preparing a 2×4 surface this way is in contrast to the lack of a 2×4 pattern when exposing an As-terminated surface to an Sb flux. These results suggest that there is an energy barrier to replacing As on the surface to from an Sb-terminated 2×4 reconstruction that can be avoided by adding In to the surface. These observations and the DFT phase diagram indicate that InAsSb of any composition

can be grown under a nearly stoichiometric surface. Finally in Section 3.3.3, STM shows that Sb roughens the surface of InAs through a cooperative mechanism of creating 2D islands and vacancy clusters (divots) in order to transform the 2×4 terrace to $c(4\times 4)$ reconstructions. This is in contrast to the past suggestion that Sb only weakly interacts with the InAs surface.

3.3.1 Surface Reconstruction Driven Sb-As Intermixing

This section employs RHEED experiments and *ab initio* calculations to examine a broad compositional range of As and Sb on the surface of InAs. The RHEED experiments first indicate that applying an Sb flux results in anion-rich $nx3$ or $c(4\times 4)$ reconstructions or roughens the surface under As-poor conditions. The DFT calculations agree well with the RHEED results after allowing Sb to occupy both dimer sites and subsurface anion sites and provide atomistic details of the surface by predicting Sb-terminated $\beta(4\times 3)$ and $c(4\times 4)$ reconstructions. Many configurations of these reconstructions are stabilized by subsurface Sb and others contain Sb-As heterodimers, which indicates that Sb-As intermixing is driven by the formation of surface reconstructions.

To efficiently explore the reconstructions available across the compositional range of Sb on InAs, experiments were conducted to monitor changes in the RHEED pattern of a static, that is, without a group-III flux, InAs (001) at 425°C under various Sb and As_2 fluxes, or beam equivalent pressures (BEPs). The results are displayed in a surface phase diagram (Figure 3.2a). In the absence of any Sb flux, the InAs surface retains a 2×4 reconstruction at this temperature for all examined As_2 fluxes. However, even the lowest Sb fluxes alter the reconstruction. For As_2 $\text{BEP} < 5.7 \times 10^{-6}$ torr, the surface exhibits an $nx3$ pattern over the entire range of Sb flux. Both 1×3 and 2×3 patterns were observed, but their existence had no apparent dependence on fluxes, so they are reported together as $nx3$. The $nx3$ RHEED is indicative of a 4×3 reconstruction [67] and this pattern is consistent with previous reports of InAsSb growth [2,63,64]. At high Sb and very low As_2 fluxes,

the RHEED pattern takes on a mixed character, exhibiting $nx3$ streaks with additional features branching or splitting off of them (Figure 3.2b), which suggests roughening through an increase in step density or formation of shallow facets [68]. This roughening of the surface under an Sb flux implies that under As-poor conditions, Sb replaces As at the surface, which is consistent with previous reports of Sb-for-As exchange [13,20]. For As_2 $BEP \geq 5.7 \times 10^{-6}$ torr, the reconstruction transitions from a disordered 1×1 at low Sb flux, and then becomes a clear $c(4 \times 4)$ at Sb $BEP > 2.01 \times 10^{-7}$ torr. A $c(4 \times 4)$ RHEED pattern, which indicates a highly group-V rich surface reconstruction, has not previously been reported for InAsSb growth. This is possibly because the In flux applied during growth introduces a finite V/III flux ratio, thereby decreasing the concentration of anions. Thus, the anion-rich $c(4 \times 4)$ might not be accessible under typical growth conditions. Near the boundary between the $(nx3)$ and $c(4 \times 4)$, the RHEED pattern exhibits a mixed $nx3/c(4 \times 4)$ character (Figure 3.2c). This suggests these phases can coexist at the boundary between the $nx3$ and $c(4 \times 4)$. Finally, all of the surface phase transitions discussed here are reversible; removing the Sb flux and annealing the surface under a sufficiently high As_2 flux returns the surface to an As-terminated 2×4 RHEED pattern. This ability to revert the Sb-terminated surface reconstructions to an As-terminated surface is consistent with the widely observed propensity of As to exchange with Sb at the surface [15–19].

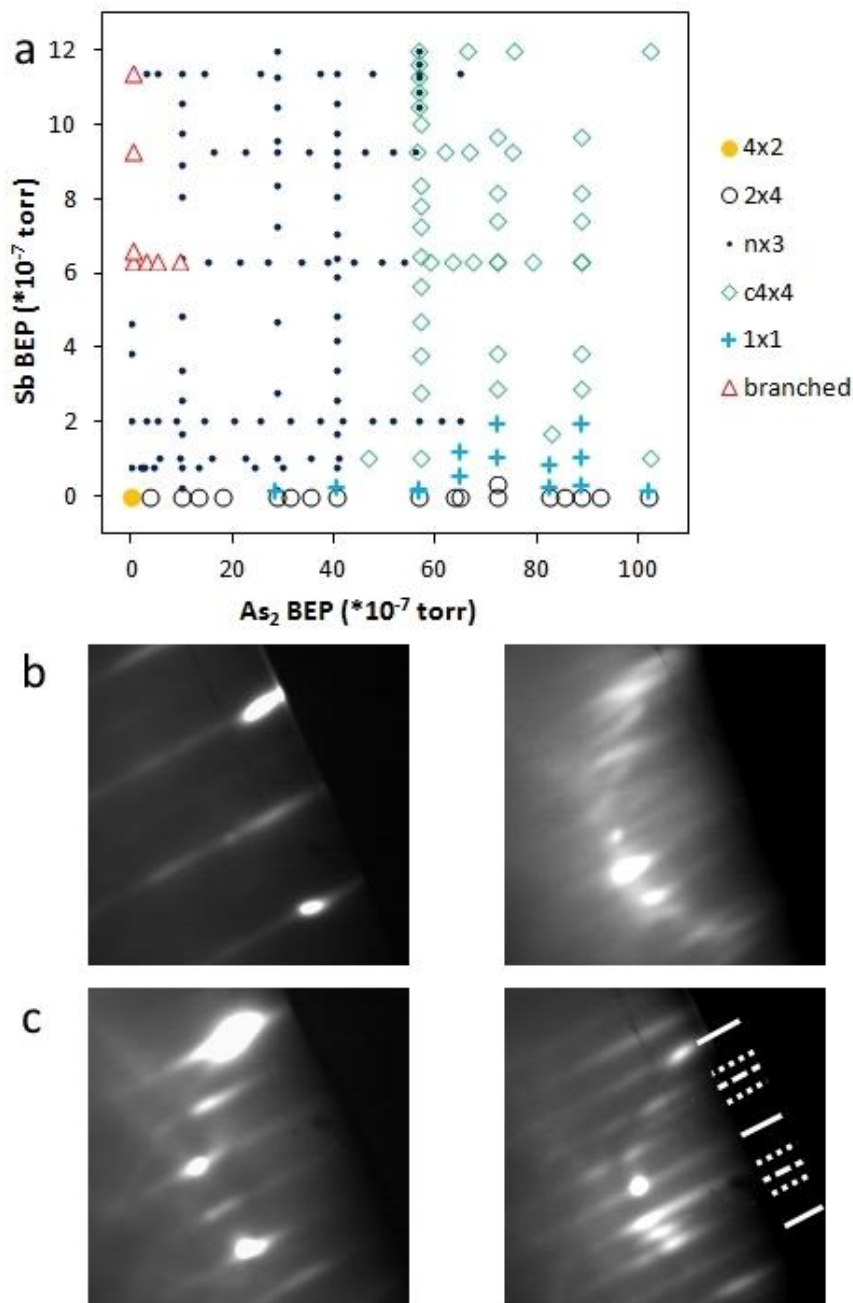


Figure 3.2 a. RHEED phase diagram of a static InAs (001) surface at 425°C under various Sb and As_2 fluxes. b&c. Selected RHEED patterns of InAs exposed to various fluxes. c. branched pattern under 9.3×10^{-7} torr Sb. d. c(4x4)/nx3 under 9.3×10^{-7} torr Sb and 5.6×10^{-6} torr As_2 with lines illustrating x2 (for the c(4x4)) and x3 periodicity. Solid lines indicate integral streaks, dotted lines indicated x3 streaks, and dashed lines indicate x2 (c(4x4)) streaks.

The RHEED experiments discussed above (Figure 3.2a) provide only information about the average periodicity of the surface without precise information about the surface reconstructions present. To better understand the atomic details of the Sb:InAs surface that are not accessible by

RHEED, DFT calculations were used to create a 0K surface reconstruction phase diagram of Sb on InAs as a function of As chemical potential, μ_{As} , and Sb chemical potential, μ_{Sb} , (Figure 3.3). In this phase diagram, a cluster expansion was conducted where atomic substitution was allowed only in dimer sites. The diagram is bounded by the formation of bulk In and bulk As at high and low μ_{As} , respectively, and bounded at arbitrarily low μ_{Sb} and the formation of bulk Sb at high μ_{Sb} . At low μ_{Sb} , effectively in the absence of Sb, the bottom edge of the phase diagram agrees well with that of pure InAs calculated in previous studies [32,35]. Namely, the In-rich $\alpha 3(2 \times 4)$ appears at low μ_{As} , followed by the As-terminated $\alpha 2(2 \times 4)$ and $\beta 2(2 \times 4)$ with increasing μ_{As} . The As-rich $c(4 \times 4)$ forms at high μ_{As} . In agreement with the RHEED phase diagram (Figure 3.2a), there is a large $c(4 \times 4)$ region, which is at approximately $\mu_{\text{As}} \geq -160$ meV and approximately $\mu_{\text{Sb}} \geq -210$ meV. However, unlike the RHEED results that showed much of the phase diagram is occupied by an $n \times 3$ pattern, only a narrow region of phase space is occupied by $\beta(4 \times 3)9^1$. Additionally, the phase diagram is dominated by 2×4 reconstructions for low to moderately high μ_{As} and μ_{Sb} , which will be discussed in further detail in Section 3.3.2. An Sb-terminated $c(2 \times 6)6$ is adjacent to the $c(4 \times 4)$ region at slightly higher μ_{Sb} than the Sb-terminated $\beta(4 \times 3)9$. It is particularly surprising that decreasing μ_{As} from the $\beta(4 \times 3)9$ results in a less Sb-rich reconstruction: $\beta 2(2 \times 4)6$, which occupies much of the high μ_{Sb} and low μ_{As} quadrant. It would be expected that this region of phase space would be more consistent with the pure InSb surface phase diagram, which features a double anion layer $c(2 \times 6)$ reconstruction at high μ_{Sb} [34]. Thus, allowing only dimer site substitution does not produce a sufficiently Sb-rich configuration to match the RHEED results.

¹See Section 3.2.3 for a summary of nomenclature.

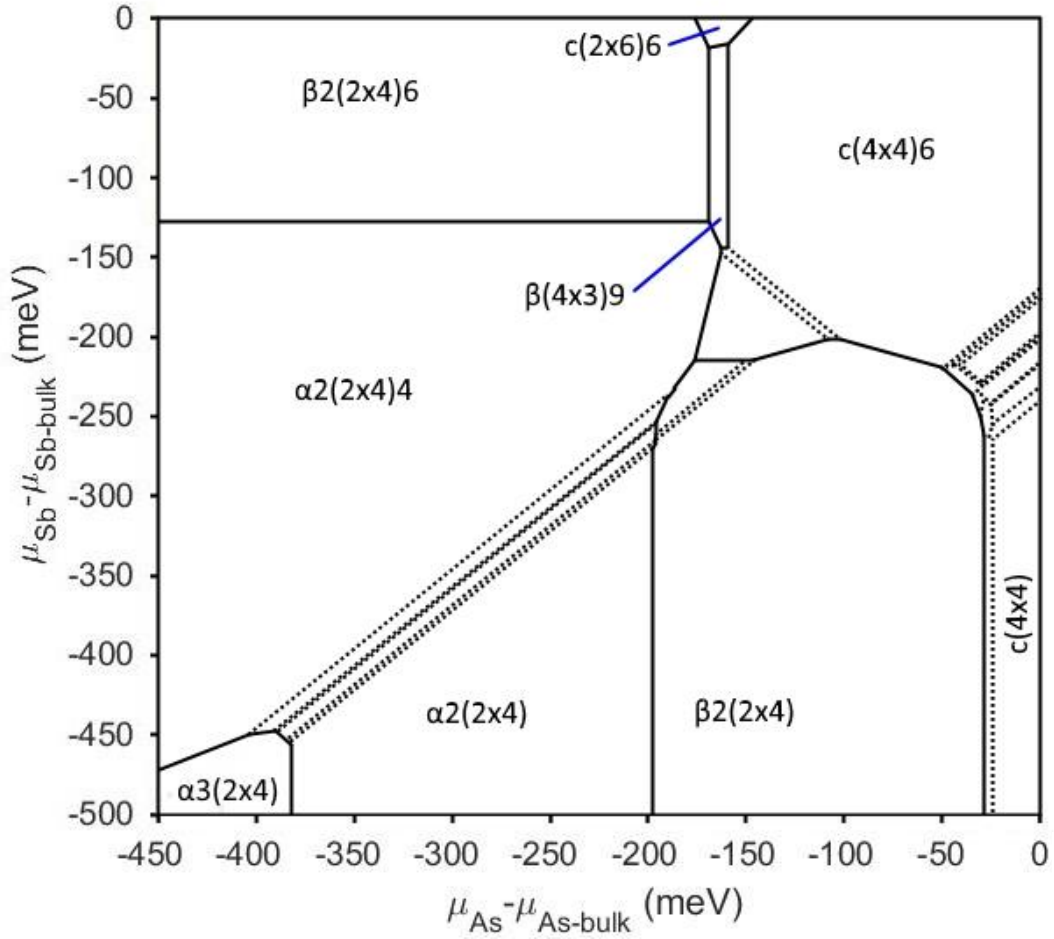


Figure 3.3 0K DFT surface reconstruction phase diagram of Sb:InAs with atomic substitution in surface dimers. Solid lines separate structural transitions while dotted lines separate configurational changes for a given structure. Unlike the RHEED phase diagram (Figure 3.2a), very little of the diagram is occupied by a 4x3 reconstruction.

The RHEED phase diagram (Figure 3.2a) indicates that unlike the predictions of DFT phase diagram created with only dimer site substitution (Figure 3.3), the high Sb, low As, quadrant should be occupied by a highly Sb-rich nx3 (4x3), rather than a less Sb-rich 2x4. In order to produce more Sb-rich configurations, a second cluster expansion was conducted where Sb was additionally allowed to occupy subsurface anion sites of the c(4x4), c(2x6), and $\beta(4x3)$ reconstructions. A single configuration of h0(4x3) with full Sb site occupancy was considered as well. Including subdimer substitution provides a calculated phase diagram (Figure 3.4) that better

agrees with the RHEED results (Figure 3.2). In this case, subsurface Sb stabilizes several 4×3 configurations in much of the high μ_{Sb} and low μ_{As} quadrant. This is more similar to the $\text{nx}3$ -dominated low As_2 flux region of the RHEED phase diagram than the case without subdimer substitution was to the RHEED phase diagram. A few additional $c(4\times 4)$ configurations are stabilized by subsurface Sb. This increases the region of chemical potential space covered by $c(4\times 4)$ configurations such that these configurations are stable at high μ_{Sb} with low $\mu_{\text{As}} = -220$ meV compared to the previous boundary of $\mu_{\text{As}} = -180$ meV when μ_{Sb} is high (Figure 3.3). The increase in the area of stability for the $c(4\times 4)$ reconstructions remains consistent with the high As_2 flux part of the RHEED phase diagram, which is dominated by a $c(4\times 4)$ RHEED pattern. The $c(2\times 6)$ is no longer predicted on the 0K DFT phase diagram after allowing subdimer Sb substitution. This result was unexpected because this reconstruction has been observed coexisting with a $c(2\times 8)$ on an InAs surface exposed to a high Sb flux after first depositing 1 ML In [36]. These results suggest that the $c(2\times 6)$ might be metastable or might be stabilized by entropy at finite temperatures through coexistence with other reconstructions. However, such coexistence would be too computationally expensive to investigate with DFT calculations and the $c(2\times 8)$ was not simulated in the present study.

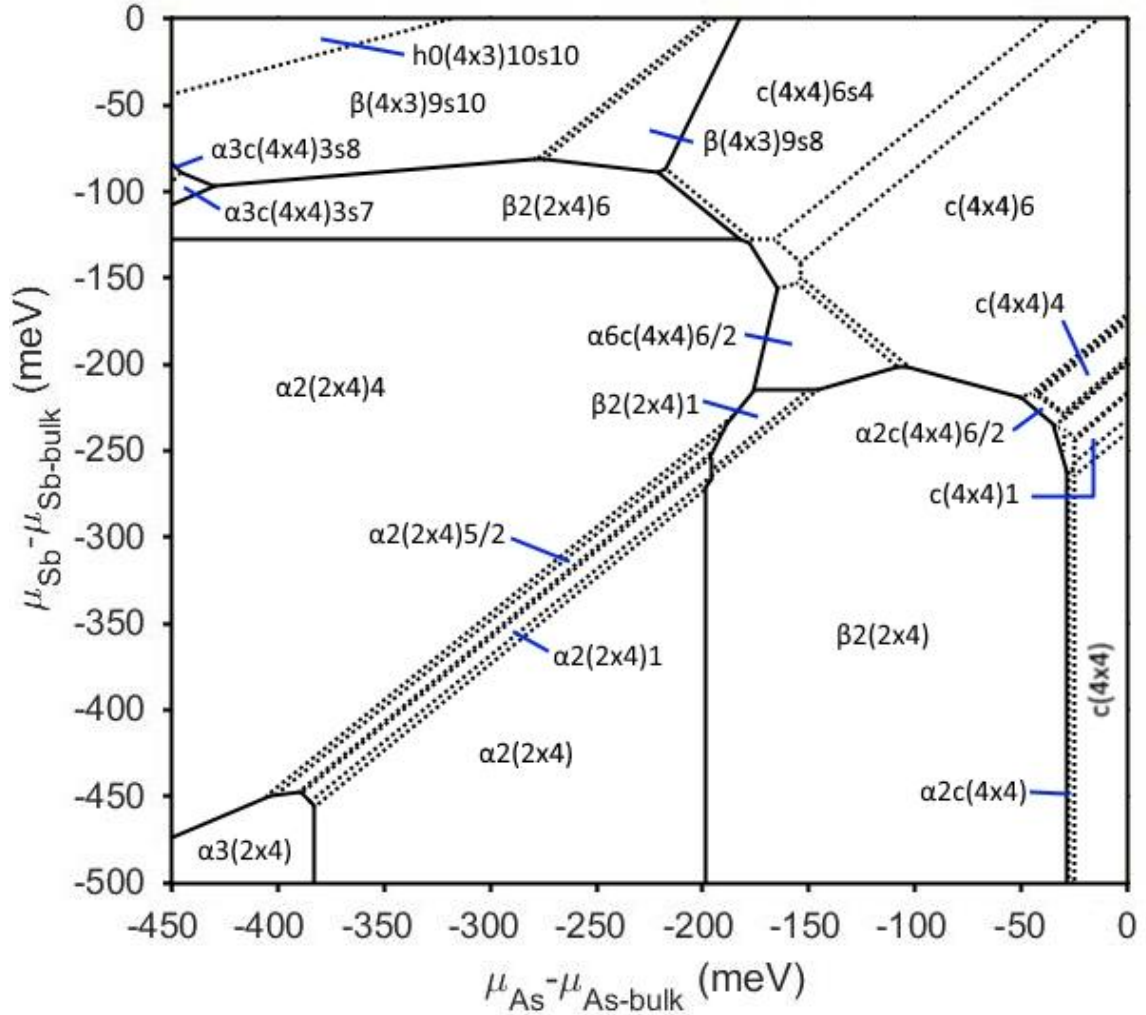


Figure 3.4. 0K DFT surface reconstruction phase diagram of Sb on InAs (001) allowing Sb to occupy both dimer and subsurface sites. Solid lines separate reconstruction prototypes and dotted lines separate compositional configurations of a given reconstruction. Unlike Figure 3.3 much of the phase diagram is occupied by 4x3 reconstructions, which better agrees with the RHEED results in Figure 3.2a.

To illustrate the trends in Sb site occupation with changes in chemical potential, a sample of reconstructions from the phase diagram (Figure 3.4) are presented schematically in Figure 3.5. The remaining reconstructions are included in Appendix B. For those predicted to be stable for the Sb:InAs system, the formation of various reconstructions proceeds generally as would be expected with either increasing μ_{As} or μ_{Sb} . Starting from the In-rich $\alpha 3(2 \times 4)$, increasing either μ_{As} or μ_{Sb} first creates reconstructions terminated by a single layer of anions: various configurations of $\alpha 2(2 \times 4)$

and $\beta 2(2 \times 4)$. Further increasing μ_{As} or μ_{Sb} results in further increasing the surface anion concentration by creating double anion layer reconstructions: various compositional configurations of $\beta(4 \times 3)$ and $c(4 \times 4)$.

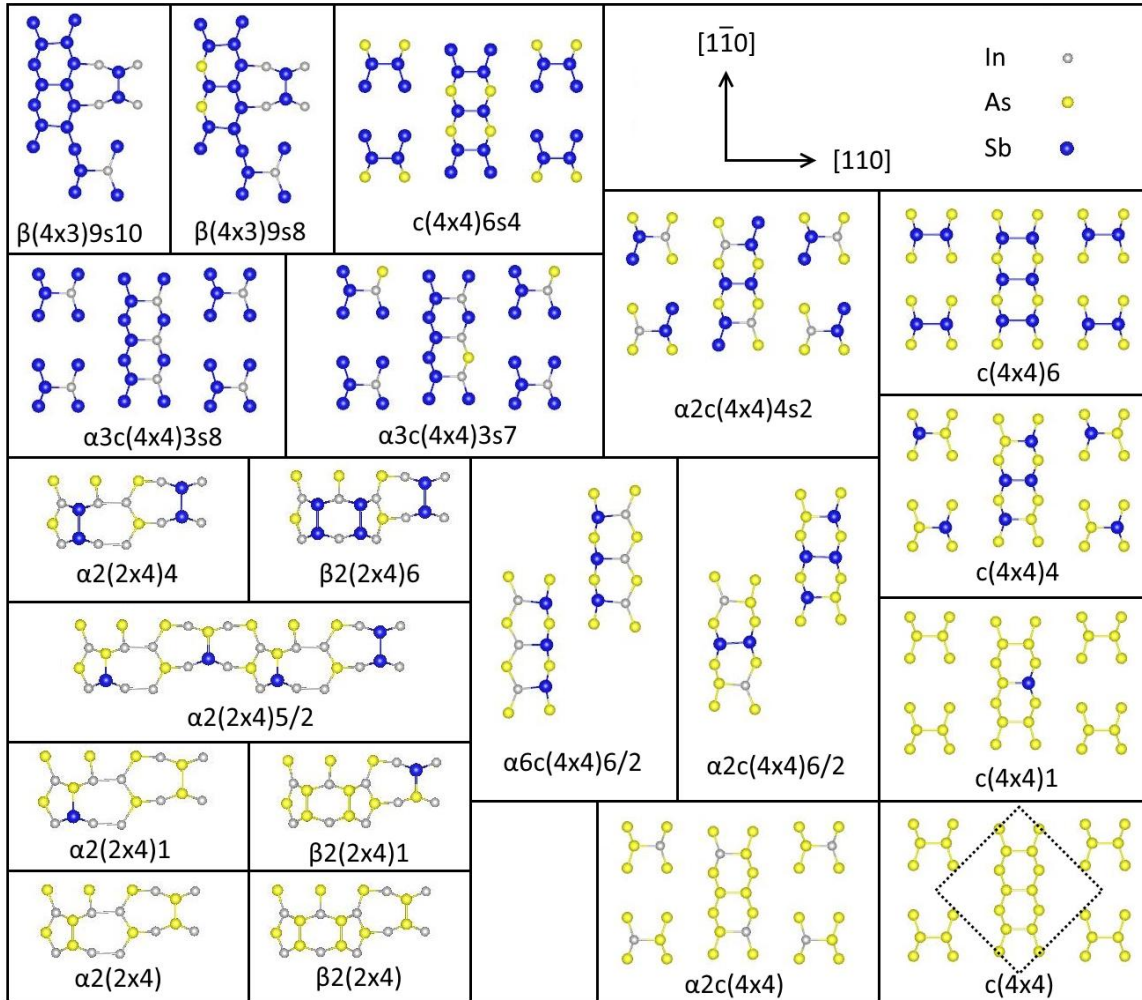


Figure 3.5. Schematics of selected group-V-rich surface reconstructions from the phase diagram in Figure 3.4. For clarity, some atoms are removed, some atoms are duplicated, and the $c(4 \times 4)$ unit cell is outlined.

In detail, when increasing μ_{Sb} from the InAs $\alpha 2(2 \times 4)$, the surface concentration of Sb increases by forming dimers containing an As and an Sb atom, that is, As-Sb heterodimers (Figure 3.4 & Figure 3.5). First $\alpha 2(2 \times 4)1$ is created by forming an Sb-As heterodimer. With increasing μ_{Sb} , one Sb atom is added at a time until the trench dimer becomes an Sb-Sb homodimer in

$\alpha 2(2 \times 4)5/2^2$. At sufficiently high μ_{sb} , the $\alpha 2(2 \times 4)4$ is created, which is completely terminated by Sb-Sb homodimers. Further increasing μ_{sb} results in the addition of another Sb homodimer to create the $\beta 2(2 \times 4)6$. These DFT predictions of Sb-terminated 2×4 reconstructions is consistent with past studies. While there have been reports of an InAsSb 2×4 RHEED pattern during growth [65], a 2×4 pattern on a static InAs surface exposed to a high Sb flux at high temperature [13], and an Sb-terminated $\alpha 2(2 \times 4)4$ on InAs [35], these results are not widely known. The best agreement occurs between the current work and the latter study, in which *ab initio* calculations predicted the $\alpha 2(2 \times 4)4$, which was confirmed using STM.

At the minimum $\mu_{\text{As}} = -450$ meV, still increasing μ_{sb} from the $\beta 2(2 \times 4)6$ causes the surface to transition to double anion layer reconstructions. First the $\alpha 3c(4 \times 4)3s7^2$ and $\alpha 3c(4 \times 4)3s8$ form, which are terminated by In-Sb heterodimers and contain subsurface Sb. The subsurface Sb is not surprising because this transition can be thought of as adding a layer of Sb to an already Sb-terminated surface. While there are no $c(4 \times 4)$ reconstructions at the corresponding location of the RHEED phase diagram (Figure 3.2a), that is, under an applied Sb flux, but without an As_2 flux, this is not a contradiction. The absence of an As_2 flux does not necessarily mean that μ_{As} is minimized. Thus, these RHEED experiments might have occurred in a regime that bypasses the $c(4 \times 4)$ in favor of the $\beta(4 \times 3)$. Similar to the RHEED experiments with high Sb fluxes, the 4×3 reconstructions become stable at high μ_{sb} .

When increasing μ_{As} from the InAs $\alpha 2(2 \times 4)$, the surface transitions to the expected $\beta 2(2 \times 4)$ [32]. Increasing μ_{sb} from the InAs $\beta 2(2 \times 4)$ at approximately $\mu_{\text{As}} = -170$ meV creates $\beta 2(2 \times 4)1/2$ followed by $\beta 2(2 \times 4)1$, each of which contains one As-Sb heterodimer. Further increasing μ_{sb} results in a transition to $\alpha 6c(4 \times 4)6/2$, which is completely terminated by In-Sb

² See section 3.2.3 for a summary of nomenclature.

heterodimers. The Sb surface concentration continues to increase by replacing the dimer-site In atoms and some subsurface As atoms until $c(4\times4)6s4$ forms. At higher As chemical potential, approximately $\mu_{\text{As}} \geq -140$ meV, the As-terminated $\beta 2(2\times4)$ can transition directly to an Sb-rich $c(4\times4)$ configuration, which will be discussed in greater detail in Section 3.3.3.

At low μ_{Sb} and approximately $\mu_{\text{As}} \geq -30$ meV, three different configurations of the $c(4\times4)$ are found (Figure 3.4 & Figure 3.5), two of which contain In-As heterodimers ($\alpha 2c(4\times4)/2$ and $\alpha 2c(4\times4)$), and one containing only As-As homodimers ($c(4\times4)$). Interestingly, the $\alpha 6c(4\times4)/2$, which was found for GaAs [66], does not appear for InAs despite the fact that it is nearly degenerate in energy with the other As-terminated $c(4\times4)$ configurations, though it might exist at finite temperature. Starting from the completely As-terminated $c(4\times4)$ and increasing μ_{Sb} , the surface transitions through several reconstructions creating Sb-As heterodimers by adding one Sb atom at a time until all dimer sites are occupied by Sb. The middle dimer fills first, as illustrated in $c(4\times4)1$, followed by the outer dimers, as in $c(4\times4)4$, until all dimer sites are occupied by Sb in $c(4\times4)6$. At slightly lower μ_{As} , the surface excess As concentration decreases and there are additional configurations containing In-As heterodimers, such as in $\alpha 2c(4\times4)6/2$. The In-As heterodimers are presumably preferred by the system over In-Sb heterodimers because the In-As bond is stronger than the In-Sb bond [69]. At even lower As chemical potential, no As remains in the dimer sites and the $\alpha 6c(4\times4)6/2$ forms. Further increases in Sb concentration from either the $\alpha 6c(4\times4)6/2$ or $c(4\times4)6$ require subdimer Sb substitution to eventually create $c(4\times4)6s4$. Further decreasing μ_{As} , the $\beta(4\times3)$ reconstruction appears and the number of subdimer sites occupied by Sb increases from 8 subdimer sites in $\beta(4\times3)9s8$ to full occupancy in $\beta(4\times3)9s10$. In contrast, a previous *ab initio* study predicted an Sb-terminated $\alpha(4\times3)$ to be stable on InAs at very low As chemical potential and high Sb chemical potential [35]. However, their calculations predicted the Sb-terminated $\beta(4\times3)$ to

be less than $0.1 \text{ meV}/\text{\AA}^2$ lower in surface energy than the Sb terminated $\alpha(4\times 3)$ using a different software package (FHIMD98) for the DFT calculations than in the present work. Additionally, at the time of that study they did not have the tools available to efficiently examine the full chemical potential range of the system. The most Sb-rich reconstruction accessible to the system is $h0(4\times 3)10s10$, which is stable at low μ_{As} and high μ_{Sb} . This is surprising since the $c(2\times 6)$, which has the same group-V concentration as $h0(4\times 3)$, is predicted to be stable for InSb [34], though this might be the result of strain due to the difference in lattice parameter between InAs and InSb. At minimal μ_{As} and approximately $\mu_{\text{Sb}} = -100 \text{ meV}$, the surface transitions again into one of two $c(4\times 4)$ configurations completely terminated by In-Sb heterodimers and containing subdimer Sb, namely $\alpha 3c(4\times 4)3s7$ and $\alpha 3c(4\times 4)3s8$.

The surface reconstruction configurations predicted on the DFT phase diagram (Figure 3.4 & Figure 3.5) suggest that rather than simply segregating, Sb and As have complex atomic scale interactions. This has implications for crystal growth in that Sb is present in reconstructions in both weakly bound dimer sites and strongly bound subsurface sites. Thus, Sb is both driven to infiltrate an InAs crystal and remain on the surface, when there is a double-anion reconstruction present. This suggests that controlling the growth surface reconstruction might control interfacial broadening in arsenide/antimonide heterostructures as well as compositional uniformity in InAsSb. Many configurations of the $\alpha 2(2\times 4)$, $\beta 2(2\times 4)$, and $c(4\times 4)$ reconstructions contain Sb-As heterodimers, rather than Sb and As being separated into homodimers. Thus, Sb and As are driven to evenly dispersed across the growth surface, rather than concentrated into different domains, so such surface reconstructions might promote compositionally uniform InAsSb films. It is noteworthy that at sufficiently high μ_{Sb} , Sb begins to infiltrate the subsurface layer after all of the As has been replaced by Sb or In in the dimer layer. Indeed, all of the 4×3 and a few of the $c(4\times 4)$

configurations are stabilized by subsurface Sb atoms. These predictions of surface reconstructions stabilized by subdimer substitution of Sb and configurations containing Sb-As heterodimers are evidence that Sb-As intermixing is driven by the formation of surface reconstructions. This is in contrast to the surface segregation model for interfacial broadening [25,70], which assumes that weakly Sb atoms exchange with As to remain on the surface during growth, while some of them become trapped in the grown crystal. Instead, Sb atoms intermix with As atoms at the surface to form stable surface reconstructions, making the Sb atoms more strongly bound to the crystal. However, the Sb atoms do still have a preference for dimer sites; all of the reconstructions that contain subsurface Sb lack As in the dimer sites. Additionally, it has been suggested that the excess Sb atoms present in double anion layer reconstructions, such as 4×3 or $c(4\times 4)$, contribute to the interfacial broadening in arsenide/antimonide heterostructures [27]. This is consistent with experimental observations of Sb segregation [22,23,25,62]. When μ_{As} is sufficiently high, Sb is limited to occupying dimer sites probably because the Sb atom is larger than the As atom and Sb segregation to the surface would minimize strain energy for the crystal. Additionally, this leaves subsurface As bonded with In, which is a lower energy state because the In-As bond is stronger than the Sb-In bond [69]. However, with lower μ_{As} , Sb can infiltrate the crystal and intermix with As in the subsurface layer, which is consistent with previous reports of Sb-for-As exchange occurring under certain conditions [13,20]. This could account for the widely observed interfacial broadening in III-As/III-Sb heterostructures [19,22,23,25].

3.3.2 *Control of Surface Stoichiometry*

Because III-V devices and films are typically grown by depositing vapor onto a crystalline substrate (e.g. through molecular beam epitaxy (MBE) or chemical vapor deposition), all crystal growth processes occur at the surface. Thus, understanding and controlling the quality of the

growth by manipulating surface reconstructions is important for the quality of the film. InAsSb is often observed to have an $nx3$ RHEED pattern during growth [2,63,64] and is often unintentionally background n-type doped [10,63,71–73]. Additionally, it has been suggested that the excess Sb atoms present in a double anion layer reconstruction contribute to the interfacial broadening in arsenide/antimonide heterostructures [27]. Thus, growth under a $2x4$ reconstruction without excess anions might prevent this broadening. While there has also been a report of InAsSb $2x4$ RHEED pattern during growth [65], research has not previously been conducted to determine how to control the stoichiometry of the growth surface.

The purpose of this section is to review the DFT predictions and RHEED results of Section 3.3.1 and compare them to additional RHEED and STM experiments. The DFT calculations indicated that several $2x4$ reconstructions should be stable for the Sb:InAs, though this was not supported by the RHEED experiments of a static InAs surface exposed to Sb and As_2 fluxes. However, the $\alpha 2(2x4)4$ surface can be stabilized instead by first creating an In-rich surface before exposure to an Sb flux. This suggests that converting an As-terminated $2x4$ to an Sb-terminated $2x4$ is a slow process requiring Sb-for-As exchange. By increasing the surface concentration of In, this process can be circumvented. These results suggest that a $2x4$ surface can be maintained during InAsSb growth by providing sufficient In to the surface.

As noted in the preceding paragraph, an apparent discrepancy exists between the *ab initio* phase diagram (Figure 3.4) and the RHEED phase diagram of a static InAs surface (Figure 3.2a). While much of the DFT phase diagram is occupied by $2x4$ reconstructions, they are not present on the RHEED phase diagram after exposure to Sb. Adding Sb to the InAs $2x4$ surface at the relatively low temperature of 425°C tends to proceed directly to a double anion layer terminated reconstruction such as the $c(4x4)$ or $4x3$. In this case, the Sb is more easily accommodated on top of the existing anion layer. It is possible that there exists a formation barrier that slows the

transition from the pure InAs reconstructions to an Sb-containing 2x4 reconstruction. One study indicated that an Sb-terminated 2x4 surface can be created on InAs either by heating the substrate to above 500°C under a high Sb BEP= 1.2×10^{-6} torr [13], while another revealed that this can be accomplished by annealing InAs under a low Sb deposition rate of 0.1 ML/s for one hour at 490°C [35]. These experiments were conducted at higher temperatures and for longer exposure times than in the present study, suggesting the transition is a slow process that requires significant thermal energy to occur, and is thus kinetically limited. In order to transform an InAs 2x4 surface to an Sb-terminated 2x4 surface, Sb must substitute for As in the dimer sites. This process is presumably slow because the In-As bond is stronger than the In-Sb bond [69], thus creating a large activation barrier.

On the other hand, this configuration can be achieved by converting the In-rich reconstruction to the $\alpha 2(2 \times 4)_4$ reconstruction. In this case, samples were prepared by first depositing 0.5 to 1.0 ML In at 425°C, followed by exposing the surface to Sb and/or As₂ fluxes. In doing so, a 2x4 RHEED pattern emerges under an Sb BEP= 5.1×10^{-8} torr up to 2.94×10^{-7} torr, above which the surface transitions to an nx3 or more complex pattern with branched streaks (Figure 3.2b). Figure 3.6 shows an STM image of one such sample displaying a structure consistent with the $\alpha 2(2 \times 4)$ reconstruction, which confirms the DFT predictions of Sb-terminated $\alpha 2(2 \times 4)$ configurations (Figure 3.4 & Figure 3.5). Exposing this surface even to a small As₂ BEP ($\geq 6.6 \times 10^{-8}$ torr) quickly transforms the RHEED pattern to the branched pattern shown in Figure 3.2b, suggesting that the Sb-terminated 2x4 is difficult to maintain at this temperature without replenishing the supply of In at the surface.

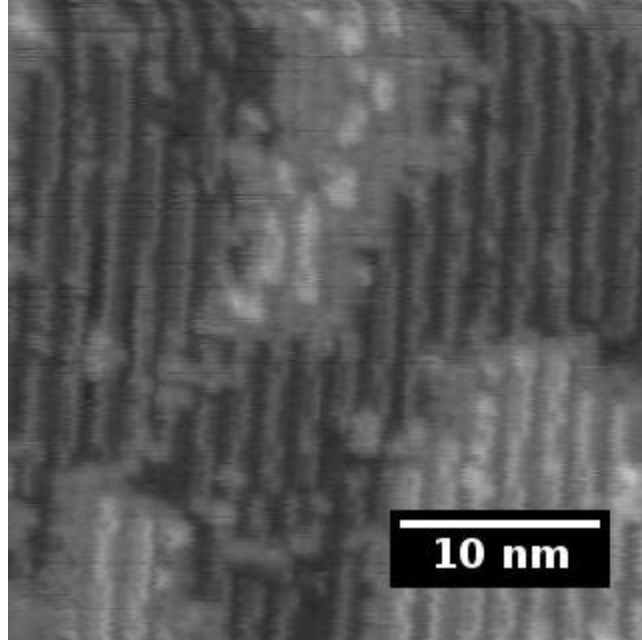


Figure 3.6. STM image of an Sb-terminated InAs surface prepared by depositing 1.0 ML In on InAs before exposure to an Sb BEP of 7.8×10^{-8} torr.

The results of this chapter illustrate that there are multiple paths to control the stoichiometry of an InAsSb surface, though the highly anion-rich reconstructions might not be desirable. It is proposed that controlling the growth surface by stabilizing a stoichiometric reconstruction might improve the quality of the grown InAsSb and reduce compositional broadening in III-As/III-Sb heterostructures. The RHEED experiments on a static InAs surface (Figure 3.2a) suggest that the 4×3 and $c(4 \times 4)$ reconstructions, with a double anion layer, are the most straightforward to obtain. Indeed, an $n \times 3$ RHEED pattern is often observed for InAsSb growth [2,63,64]. However, this growth surface might not be desirable since InAsSb is widely observed to contain n-type defects [10,63,71–73]. Alternatively, one report indicates that this n-type doping persists when growing InAsSb with a 2×4 reconstruction under high As_4 flux [65]. However, no reports in the literature have investigated a potential link between growth RHEED pattern (surface reconstruction) and point defects. It is possible that growth under a double anion layer reconstruction, with effectively a layer of antisites at the surface, kinetically traps point

defects and causes the n-type defects in InAsSb. Additionally, it has been suggested that the excess Sb atoms present in a double anion layer reconstruction contribute to the interfacial broadening in arsenide/antimonide heterostructures [27]. The more weakly bound Sb atoms in the upper anion layer might be more easily displaced and unintentionally incorporated during growth of an arsenide layer on top. While this excess Sb can be removed by annealing the antimonide layer under an As flux prior to the arsenide growth [14], stabilizing a stoichiometric antimonide (such as InAsSb) surface might be a better method. The stoichiometric surface, by definition, does not have the problem of excess Sb, which would save time by eliminating the need to remove the excess atoms by annealing. Also, since As is well known to readily exchange with Sb in the crystal [13–19], this annealing step has the potential to reduce the Sb content of the antimonide from its desired concentration.

The results of this section, along with some analysis of the literature suggest experimental conditions that would allow for MBE growth of InAsSb films under a stoichiometric surface. The above DFT (Figure 3.4) and STM (Figure 3.6) observations, along with results in the literature [13,35,65], suggest that InAsSb can be synthesized under a stoichiometric $\alpha 2(2 \times 4)$ surface reconstruction under a variety of growth conditions. The DFT results suggest that maintaining low As and Sb chemical potentials. This is consistent with the fact that, while not widely known, the 2×4 has been observed for an InAsSb growth surface under As_4 -rich, rather than the more typical As_2 , conditions [65]. They observed that Sb incorporation was increased when using As_4 instead of As_2 , which implies that As_4 is less easily incorporated than As_2 and effectively creates a lower μ_{As} . Additionally, film growth includes an In flux, which lowers the relative concentrations of As and Sb at the surface and effectively makes both μ_{As} and μ_{Sb} lower than what might be experimentally accessible for a static surface. This is also consistent with the observation

that exposing an In-terminated surface to Sb leads to a 2×4 RHEED pattern, while exposing an As-terminated surface to Sb does not at 425°C . In practice, this would be similar to growth with a low V/III flux ratio. Finally, the kinetic limitation to the formation of an Sb-terminated 2×4 suggests that, consistent with previous reports [13,35], increasing the growth temperature to 490°C might aid in stabilizing a 2×4 surface. A higher growth temperature effectively lowers the anion chemical potentials through increased desorption. Thus, it is suggested that in order to grow InAsSb under a stoichiometric $\alpha 2(2 \times 4)$, rather than a highly anion-rich 4×3 , the growth should proceed with a low V/III ratio, with As_4 instead of As_2 , and at high temperature.

3.3.3 Surface Roughening and Intermixing Driven by Phase Transition

In this section, further experiments were conducted to examine the interaction of Sb on InAs surfaces at the atomic scale and compare these results to the DFT calculations. Scanning tunneling microscopy (STM) reveals that Sb reacts with InAs to roughen the surface on the atomic scale through the formation of 2D islands and vacancy clusters (divots) consisting of $c(4 \times 4)$ reconstructions. Reviewing the *ab initio* calculations predicts that these stable surface reconstructions contain In-Sb heterodimers. For these to form, we show that As and In atoms must be displaced from the surface, resulting in atomic-scale roughening and intermixing of the alloy. Given that it is supported directly by experimental data and predicted by theoretical calculations, we propose this intermixing model as the correct atomistic mechanism for As-Sb interfacial broadening.

STM was used to characterize the atomistic interaction between As and Sb on the surface of InAs and gather further evidence of Sb infiltrating the InAs surface. In agreement with the branched RHEED pattern that arises after Sb exposure (Figure 3.2b), STM shows that Sb roughens the InAs surface. Figure 3.7 shows filled state STM images of InAs (001) surfaces prepared under $T=405^\circ\text{C}$

and 425°C. At both temperatures, the pure InAs surfaces exhibit the expected $\beta 2(2 \times 4)$ reconstruction, but with occasional dimer vacancies (divots) and small 2D islands (Figure 3.7a&c). The divot and island coverages of these surfaces are nominally equivalent, at about 2% and 6%, respectively (Table 3.1). Table 3.1. Island and Divot Coverages of Sb:InAs and Pure InAs Surfaces). Figure 3.7b&d show InAs surfaces that were exposed to approximately 0.1 ML of Sb at $T = 405^\circ\text{C}$ and 425°C, respectively. Both surfaces still exhibit the $\beta 2(2 \times 4)$ reconstruction, with an increase in 2D island coverage due to the presence of Sb, in agreement with observations by Nosho et al. [36]. At 405°C, the 7 percentage point increase in island coverage as a result of the deposited Sb is lower than expected, though this might be due to uncertainty in the measurement of either the island coverage or the Sb flux. The divot coverage at this temperature remains unchanged by Sb exposure. On the other hand, at 425°C, a 17 percentage point increase in island coverage is observed, significantly greater than would be expected, especially when compared to the lower than expected increase in island coverage at 405°C. In addition, there is a 9 percentage point increase in the divot coverage. Furthermore, the divots exist as large clusters rather than the occasional missing dimers observed in the initial InAs surface.

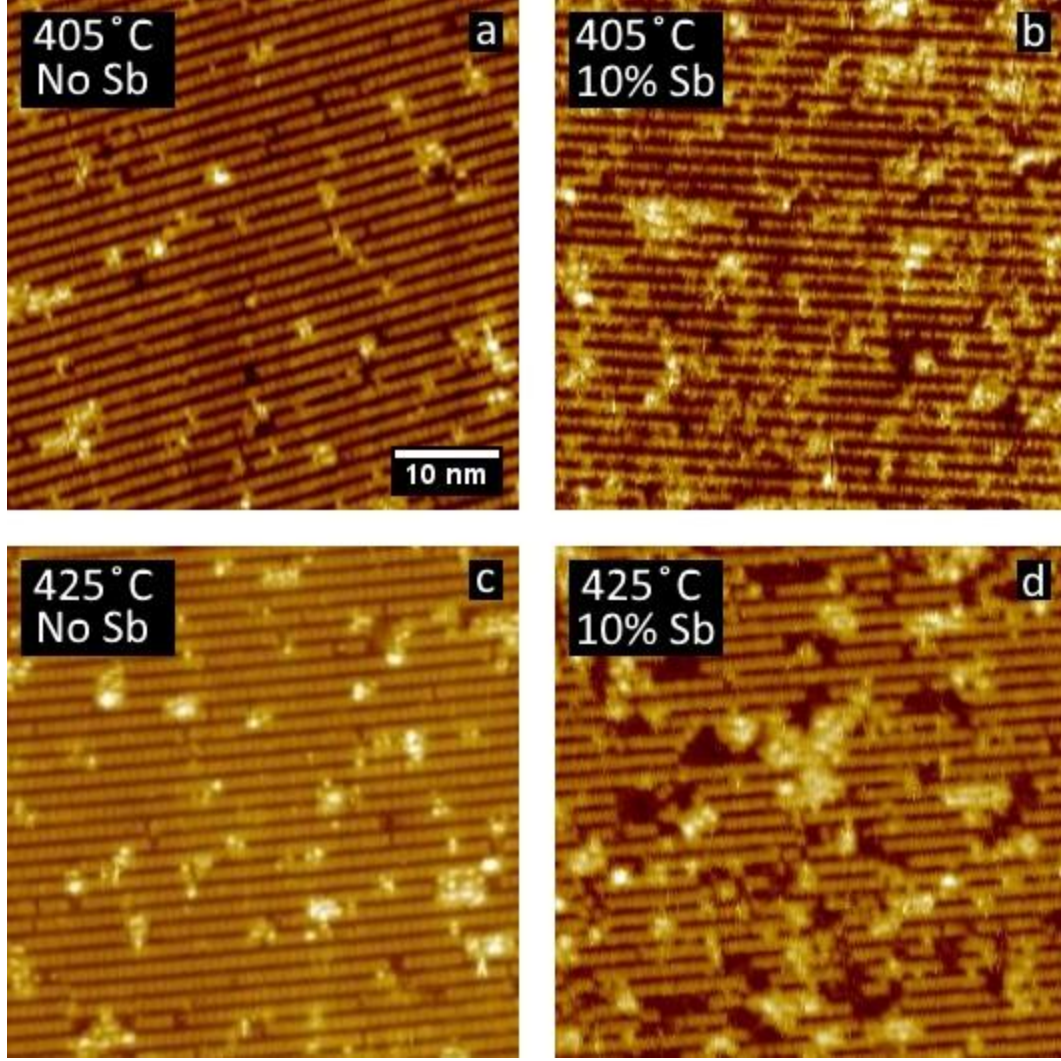


Figure 3.7. Filled state ($-2.7 \text{ V} \leq V_{\text{bias}} \leq -2.3 \text{ V}$) STM images of InAs surfaces prepared by MBE under various growth conditions. a. 405°C, pure InAs; b. 405°C, 0.1 ML Sb deposited; c. 425°C, pure InAs; and d. 425°C, 0.1 ML Sb deposited. All samples display $\beta 2(2 \times 4)$ dimer rows.

Table 3.1. Island and Divot Coverages of Sb:InAs and Pure InAs Surfaces

Figure 3.7	Temp. (°C)	Dep. Sb (%)	Coverage (%)	
			Island	Divot
a	405	0	6.0 ± 0.8	1.6 ± 0.5
b	405	10	13.2 ± 1.4	1.2 ± 0.2
c	425	0	5.3 ± 1.7	1.7 ± 0.8
d	425	10	21.8 ± 1.7	10.7 ± 1.0

To further investigate the chemical and structural details of the surface islands and divots, pairs of dual bias STM images were captured. Figure 3.8 shows dual bias STM images of

an InAs surface prepared with 0.1 ML of Sb deposited at 425°C. These images reveal that the surface reconstruction of the islands is clearly different than the rest of the terrace. While the small average size of the islands makes it difficult to discern, the larger islands show a structure consistent with the $c(4\times 4)$ reconstruction. Given that it has a double layer of anions on the surface, it is unsurprising that the Sb deposition caused a $c(4\times 4)$ structure, especially because it is predicted to be stable for pure InAs at extremely high As overpressures [32]. The scanning tunneling micrographs also indicate that the divots (Figure 3.8b) exhibit a $c(4\times 4)$ reconstruction as well. Additionally, bias reversal revealed that the divots appear darker and the islands appear brighter relative to the $\beta 2(2\times 4)$ dimer rows in the filled state image (Figure 3.8a) than in the empty state image (Figure 3.8b), implying that the divots and islands contain In at the surface. However, these structures are not likely completely In-terminated as no additional In was deposited after the initial InAs film was grown.

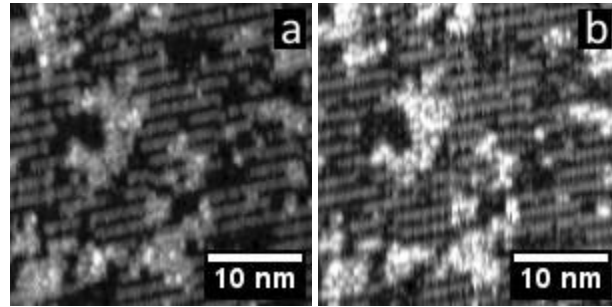


Figure 3.8. Dual bias STM images of Sb deposited on InAs at 425°C. a. filled state (-2.7 V) b. empty state (2.7 V)

To better understand the thermodynamics behind the STM images, the DFT calculations are again explored. Figure 3.9a shows a computational surface reconstruction phase diagram for the surface energy of Sb on InAs as a function of Sb chemical potential, μ_{Sb} , at a constant As chemical potential, $\mu_{\text{As}} = -140$ meV. This As chemical potential is slightly higher than the transition between the InAs $\alpha 2(2\times 4)$ and $\beta 2(2\times 4)$ and is consistent with the $\beta 2(2\times 4)$ reconstruction observed in the STM images (Figure 3.7 & Figure 3.8). Only two structural prototypes are predicted to occur at

these conditions: $\beta 2(2 \times 4)$ and $c(4 \times 4)$. The $\beta 2(2 \times 4)$ is completely As terminated and stable for arbitrarily low μ_{Sb} . The $c(4 \times 4)$ on the other hand, has three different predicted configurations. Two of these contain In-Sb heterodimers: $\alpha 6c(4 \times 4)6/2$ and $\alpha 3c(4 \times 4)9/2$ and one is completely terminated by Sb-Sb homodimers (Figure 3.9b). While the predicted $c(4 \times 4)$ reconstructions do not contain As at the surface, it is conceivable that at elevated temperature there could be some As present. However, simulated STM indicates that As and Sb are difficult to discern in $c(4 \times 4)$ reconstructions (Figure 3.10).

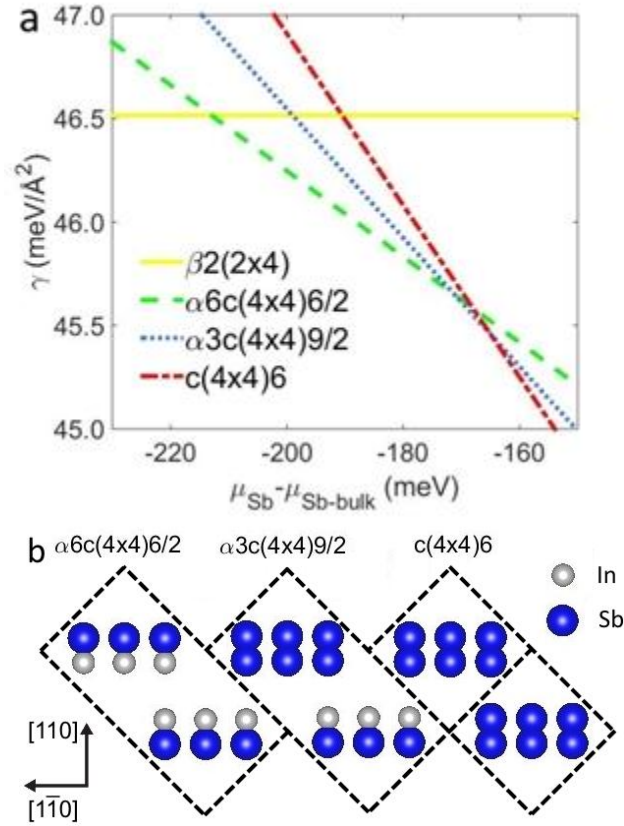


Figure 3.9. a: DFT 0K surface reconstruction phase diagram of Sb on InAs at constant $\mu_{\text{As}} = -140$ meV. b: schematics of dimer site occupancy in the stable $c(4 \times 4)$ configurations with cells outlined.

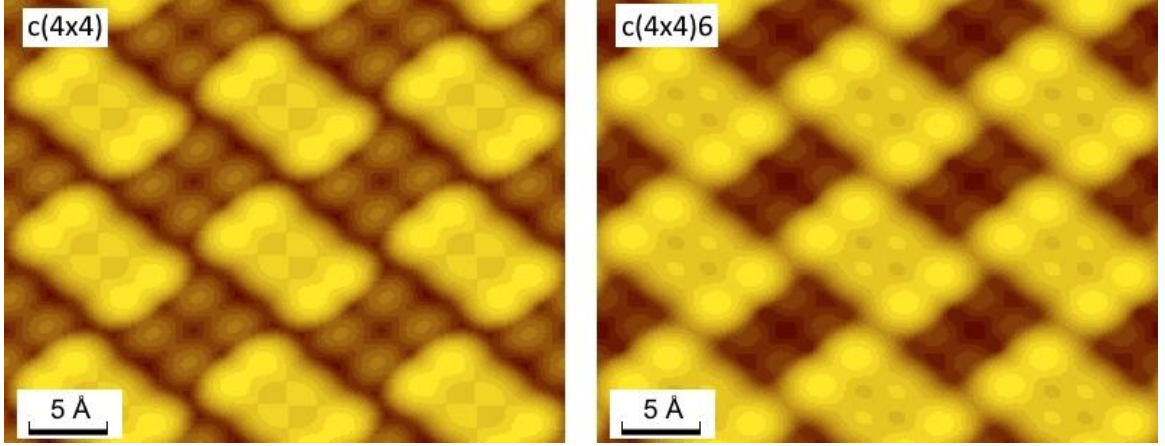


Figure 3.10. DFT simulated filled state STM images of $c(4 \times 4)$ configurations.

The presence of Sb on the surface influences the evolution of surface reconstructions on InAs. A pure InAs surface transitions from $\alpha 2(2 \times 4)$, to $\beta 2(2 \times 4)$, to $c(4 \times 4)$ with increasing μ_{As} [32]. This progression increases the concentration of As atoms at the surface. With increasing μ_{Sb} at $\mu_{\text{As}} = -140$ meV, the transition from the As-terminated $\beta 2(2 \times 4)$ transforms into three different configurations of the $c(4 \times 4)$ structure (Figure 3.9). First, the $\alpha 6c(4 \times 4)6/2$ forms, which is completely terminated by In-Sb heterodimers. The $\alpha 6c(4 \times 4)6/2$ is similar to the heterodimer terminated GaAs $c(4 \times 4)$ variant [74], referred to as $c(4 \times 4)\text{-}\alpha$ in the literature [66], but named $\alpha 6c(4 \times 4)/2$ in our notation. At higher μ_{Sb} , half of the heterodimers become Sb-Sb homodimers to form the $\alpha 3c(4 \times 4)9/2$, followed by the rest of the heterodimers to form $c(4 \times 4)6$ at even higher μ_{Sb} . Given the surface phase diagram, it is easy to understand how a “pre-soak” step [14] may improve interfacial abruptness. In this case, the Sb-terminated surface may become As-terminated by reducing the Sb overpressure, thus reducing the μ_{Sb} . This will drive the surface to the As-terminated $\beta 2(2 \times 4)$ reconstruction, and prevent Sb from incorporating into subsequent InAs. Presumably, simultaneously increasing μ_{As} will amplify this effect.

The fact that Sb deposition does not merely lead to Sb-terminated surfaces implies that there is a more complex process involved. The STM images (Figure 3.8) suggest that this occurs

through the cooperative creation of 2D islands and divots. Transforming an InAs $\beta 2(2 \times 4)$ surface (Figure 3.11a) to an Sb-terminated $c(4 \times 4)$ surface can occur through two separate pathways (Figure 3.11b): removal of atoms and addition of atoms. For divot creation (Figure 3.11b, left), 6 In and 4 As atoms per unit cell must be removed from the $\beta 2(2 \times 4)$ surface to expose an As-terminated, unreconstructed surface. For island creation (Figure 3.11b, right), 2 In and 4 As atoms per unit cell must be added to the surface to fill the trench in the $\beta 2(2 \times 4)$. The net result of these transformations is 2 excess In atoms per unit cell that can react with Sb to form $c(4 \times 4)$ reconstructions (Figure 3.11c). However, the predicted reconstructions have 3, 1.5, and 0 surface In per unit cell (Figure 3.9). This suggests that there are either local composition fluctuations, or additional In comes from step edges to complete the stable surface reconstruction for a given μ_{Sb} .

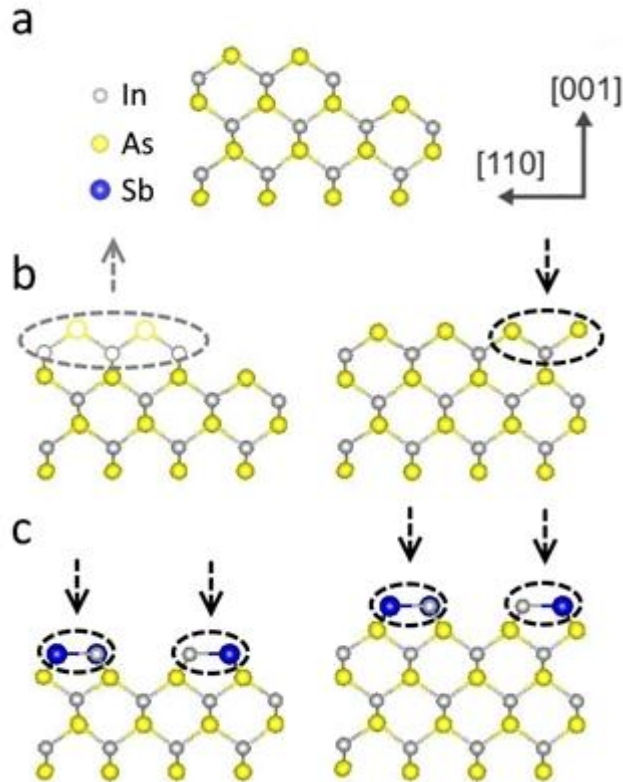
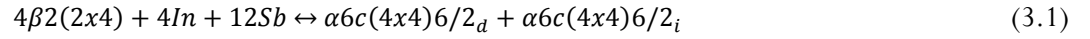


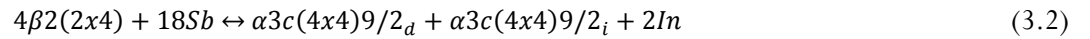
Figure 3.11. Schematic of island and divot formation. a. InAs $\beta 2(2 \times 4)$. b. left: As and In are removed to expose an As-terminated surface. right: As and In are added to create an As-terminated surface. c. Sb and In are distributed over the surface to create $c(4 \times 4)$ reconstructions.

Coexistence between $c(4 \times 4)$ configurations during the Sb-induced creation of islands and divots from the As-terminated $\beta 2(2 \times 4)$ can be explored by accounting for the atoms involved in the formation of each configuration. The formation of an island of $\alpha 6c(4 \times 4)6/2$ requires two cells of $\beta 2(2 \times 4)$. 4 In atoms and 8 As atoms are needed to fill the trenches, and 6 In atoms and 6 Sb atoms are needed to form the Sb-In heterodimers. The formation of a divot of $\alpha 6c(4 \times 4)6/2$ also requires two cells of $\beta 2(2 \times 4)$. 8 As and 6 In atoms must be removed, and 6 Sb atoms must be added. A reaction equation to form and divot-island pair (subscripts) is as follows:



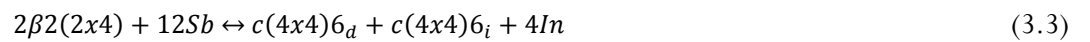
Though the As atoms are conserved, this reaction requires 4 additional In atoms, thus it cannot be the only configuration being formed.

The $\alpha 3c(4 \times 4)9/2$ configuration can be considered next in a similar manner and also consumes 2 cells of $\beta 2(2 \times 4)$. An island of $\alpha 3c(4 \times 4)9/2$ necessitates the addition of 4 In and 8 As to fill the trenches, and 3 In and 9 Sb for the dimers on top. A divot necessitates the removal of 8 As atoms and 9 In atoms, and the addition of 9 Sb atoms. This reaction is represented as follows:



The As atoms are still conserved in this case, however an excess of 2 In atoms remain after this reaction.

The $c(4 \times 4)6$ reconstruction only requires one $\beta 2(2 \times 4)$ reconstruction to form. An island requires 2 In and 4 As to fill the trench in the $\beta 2(2 \times 4)$, and 6 Sb atoms for the dimers on top. A divot requires the removal of 4 As and 6 In atoms as well as the addition of 6 Sb atoms. The equation for this reaction is



Again, this reaction consumes too few In atoms, with 6 remaining after the reaction.

Combining the above reactions (Equations 3.1-3.3) results in an expression for the formation of divots and islands containing all three c(4x4) configurations:

$$12\beta 2(2x4) + 48Sb \leftrightarrow \frac{\alpha 6c(4x4)6}{2}_v + \frac{\alpha 6c(4x4)6}{2}_i + 2\alpha 3c(4x4)9/2_v + 2\alpha 3c(4x4)9/2_i \quad (3.4)$$

12 $\beta 2(2x4)$ s are consumed to form an island of 1 $\alpha c(4x4)6/2$ and 2 $\alpha 3c(4x4)9/2$, and a divot of the same reconstructions.

While surface roughening has been observed via STM for transitions between (001) surface reconstructions on homoepitaxial GaAs and InAs [75], Sb coverage greater than 1 ML on InAs [36], and Bi on GaAs [76], and is consistent with the observed branched RHEED pattern under moderate to high Sb flux (Figure 3.2b), the present mechanism of island and divot formation has not been previously reported. This observation of Sb pulling atoms out of the surface is contrary to the accepted model of a physisorbed Sb-layer. Neglecting surface reconstructions, the surface segregation model for interfacial broadening [25,70] assumes that sub-surface Sb atoms exchange with surface As during growth, while some of them become trapped in the grown crystal. However, the STM data (Figure 3.7 & Figure 3.8) suggests instead that this broadening occurs via intermixing by Sb-induced surface roughening. This along with the DFT predictions of surface reconstructions containing Sb-As heterodimers and subsurface Sb (Figure 3.4 & Figure 3.5) indicate that rather than merely floating on the growth surface, Sb is actively infiltrating the growing crystal to cause interfacial broadening.

3.4 Conclusions

The influence of Sb on the surface of InAs has been investigated using, RHEED, STM and *ab initio* calculations. A RHEED phase diagram of a static InAs surface exposed to Sb and As₂ fluxes revealed that in the absence of an In flux, the surface is primarily terminated by reconstructions with a double layer of anions. The calculated 0K DFT surface reconstruction phase diagram

predicts that these reconstructions have configurations stabilized by subsurface Sb. Additional reconstructions contain As-Sb heterodimers. These results indicate that rather than Sb being weakly bound to the surface, Sb and As are thermodynamically driven to intermix. The DFT calculations also indicate the stability of $\alpha 2(2 \times 4)$ and $\beta 2(2 \times 4)$ configurations varying from complete As-termination to complete Sb-termination. STM imaging confirms that an Sb-terminated $\alpha 2(2 \times 4)$ is experimentally accessible. Thus, InAsSb could be grown for the full compositional range under a stoichiometric surface instead of the typical anion-rich surface, which might improve the quality of InAsSb and reduce interfacial broadening in III-As/III-Sb heterostructures. Finally, Dual bias STM images of InAs surface exposed to fractional coverages of Sb further support the DFT predictions of Sb-As intermixing. Sb is found to roughen the InAs surface through a cooperative mechanism of 2D island and divots creation. This roughening is thermodynamically driven by transforming the $\beta 2(2 \times 4)$ to islands and divots of $\alpha 6c(4 \times 4)_{6/2}$ and $\alpha 3c(4 \times 4)_{9/2}$, which results in Sb atoms in both the top layer (islands) and the layer below (divots). The mechanism of Sb pulling atoms out of the terrace is in contrast to the prevailing model that Sb is only weakly physisorbed to the surface. Thus, this roughening and intermixing is proposed to explain interfacial broadening for arsenide on antimonide interfaces in heterostructures.

CHAPTER 4

Finite Temperature Stabilization of InSb and As on InSb Surface Reconstructions

4.1 Introduction

In an effort to fully characterize the surface of InAsSb, one compositional extreme of this system, the Sb-terminated InAs surface, was discussed in CHAPTER 3. In order to better understand the atomic details of the surface of the InAsSb system, the next compositional endpoint must now be explored: As on the surface of InSb. Much of the literature cited in CHAPTER 3 regarding the complex interaction between As and Sb is applicable to the current chapter as well. This includes the often observed phenomenon of As displacing Sb from semiconductor surfaces typical growth temperatures [13–19] and the observation of Sb-for-As exchange under As-poor conditions and at elevated temperatures [13,20].

Before investigating the alloyed As on InSb system, an understanding of the surface of pure InSb is necessary. Investigations of the InSb (001) surface have been reported in the literature for studies involving reflection high energy electron diffraction (RHEED) [13,28,77–79] and low energy electron diffraction [33,80]. However few studies have examined the anion-terminated at the atomic scale, of particular note are one involving scanning tunneling microscopy (STM) [33], and another involving density functional theory (DFT) calculations [34]. While the interaction between Sb and As has been the subject of intense study in various InAs/III-Sb heterostructures [15,16,18,19,22,81], only two reports exist investigating this interaction on InSb [13,28], though not on the atomic scale.

In this chapter, a combination of *ab initio* calculations and RHEED and STM experiments are used to investigate the atomic scale details of the InSb surface and As on the surface of InSb. DFT and Monte Carlo (MC) calculations newly predict stable InSb 2×4 and $c(4\times 4)$ reconstructions, resulting in a more complete phase diagram that agrees with experimental results in the literature. STM measurements combined with the MC calculations suggest that the commonly observed A-(1×3) RHEED pattern is the result of coexistence between 4×3 and $c(4\times 4)$ reconstructions, rather than a unique reconstruction in and of itself. Next, a thermodynamic driving force for Sb-As intermixing is supported by a DFT-predicted surface phase diagram including configurations that contain subsurface As substitution on InSb. RHEED experiments confirm much of this phase diagram and provide further evidence that the InSb A-(1×3) RHEED pattern is the result of coexistence between 4×3 and $c(4\times 4)$ reconstructions. Additionally, As is found to roughen the InSb surface through the formation of facets, which is confirmation of As-for-Sb exchange. However, the formations of these As-induced facets is reversible. Removing the As flux and applying an Sb flux smoothes the surface to produce a streaky RHEED pattern, which is evidence of Sb-for-As exchange.

4.2 Procedure and Nomenclature

4.2.1 Calculations

The general procedure for creating *ab initio* phase diagrams using DFT calculations was discussed in Sections 2.5.1 and 2.6.1, while the details for As:InSb are discussed here. The surface compositions of the anion terminated reconstructions were varied by allowing atom or dimer substitution at selected sites, as indicated in Figure 4.1. Sb and As were allowed to occupy dimer sites on the 2×4 reconstructions. The 4×3 , $c(4\times 4)$, and $c(2\times 6)$ reconstructions are terminated by a double layer of group-V atoms, which necessitated the consideration of subsurface As substitution.

For the $c(4 \times 4)$, Sb, As, or In were allowed to occupy dimer sites and As was additionally allowed to occupy anion sites beneath the dimer layer, which are referred to as subdimer sites in this dissertation. The sheer number of possible compositional configurations for the 4×3 and $c(2 \times 6)$ required two sets of cluster expansions. In the first set, Sb, As, or In were allowed to occupy dimer sites and the subdimer sites only contained Sb. In the second set, As and Sb, but not In, were allowed substitute in the dimer and subdimer sites. In substitution was not allowed for the $\alpha(4 \times 3)$ when considering such subdimer substitution because this would have resulted in In homodimers, which preliminary calculations indicated were higher energy than V-V or V-III dimers. The $c(2 \times 6)$ configurations containing In in the dimer sites were all higher energy than analogous In-containing 4×3 and $c(4 \times 4)$ configurations, so In substitution was excluded when considering subsurface As for the $c(2 \times 6)$. Supercells containing up to two primitive unit cells were considered for the 2×4 reconstructions and supercells containing up to three primitive unit cells were considered for the 2×1 reconstruction.

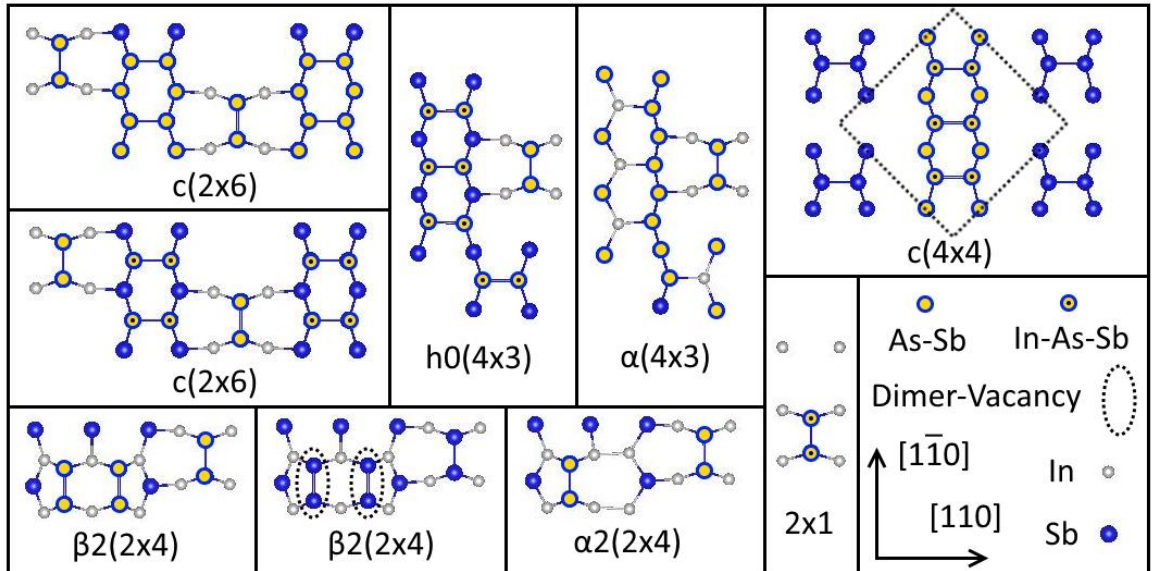


Figure 4.1. Schematics of surface reconstruction structural prototypes with sites where substitution is allowed are highlighted. Some atoms are duplicated and some are omitted for clarity. Substitution on duplicated equivalent sites is only highlighted once.

The general procedure used for running the Monte Carlo simulations and calculating surface energies from them is discussed in Sections 2.5.2 and 2.6.2. Compositional variation was simulated through In-Sb substitution at the dimer sites of InSb for the $h0(4\times3)$, $c(4\times4)$, and $c(2\times6)$ reconstructions. In-Sb substitution was not allowed in the cluster expansions of the $\alpha2(2\times4)$ and $\beta2(2\times4)$, so the number of Sb homodimers at the surface were instead allowed to vary, since the $\alpha2(2\times4)$ and $\beta2(2\times4)$ differ by only one dimer (Figure 4.1). Thus, the 2×4 MC simulation allowed either a completely $\alpha2(2\times4)$ surface, completely $\beta2(2\times4)$ surface, or a mixture of the two. The 2×1 was calculated to have much higher surface energy than the other reconstructions at all Sb chemical potentials, so it was excluded from the MC simulations.

4.2.2 MBE Growth, RHEED, and STM

The general procedure for MBE growth of these samples was discussed in Section 2.3. Films were grown on InAs (001) substrates without growing an InAs buffer. After oxide desorption, the substrates were cooled to 380-390°C to grow at least 1 μm of InSb with a growth rate in monolayers per second of $R_{\text{In}}=0.57$ ML/s and Sb BEPs ranging approximately 8.2×10^{-7} to 9.2×10^{-7} torr, which always resulted in a streaky $A-(1\times3)$ RHEED pattern. All samples were annealed without Sb overpressure for at least 5 minutes at the growth temperature. Samples were then heated or cooled to the temperature of interest and either exposed to various As_2 and Sb fluxes or exposed to Sb after depositing 1.0 ML of In. The RHEED experiments were conducted in series of either increasing or decreasing As_2 or Sb fluxes, with at least 200 nm of InSb grown between series. Samples used for STM imaging were quenched to room temperature by immediately turning off the substrate heater without supplying an Sb overpressure. STM images were acquired with a constant current of 0.1 nA at room temperature in a chamber attached *in vacuo* to the MBE chamber.

4.2.3 Surface Reconstruction Nomenclature

Surface reconstructions of the As:InSb system are named in a similar manner to those for Sb:InAs as discussed in Section 3.2.3, with Sb and As switched. In this chapter, the number following the root reconstruction denotes the number of As atoms occupying dimer sites. The number following the letter 's' refers to the number of subsurface As atoms. For the $c(4\times 4)$ and $c(2\times 6)$, ' α ' followed by a number indicates the number of In-V heterodimers at the surface. Dividing the name by an integer denotes a supercell consisting of multiple primitive unit cells of the root reconstruction. For example, a $c(2\times 6)$ containing 1 subsurface As atom distributed over 2 unit cells is named $c(2\times 6)s_{1/2}$. A $c(4\times 4)$ consisting of 3 In-As heterodimers and 6 subsurface As atoms is called $\alpha_3c(4\times 4)_6s_6$. The use of Greek letters in the 2×4 and 4×3 reconstruction prototypes follows long-established conventions in the literature.

4.3 Results and Discussion

The results of RHEED and STM experiments and *ab initio* calculations of the InSb surface and As on the InSb are divided into two sections here. First, DFT and MC simulations of the InSb (001) surface are presented in Section 4.3.1. These calculations produced a surface reconstruction phase diagram includes 2×4 and $c(4\times 4)$ reconstructions. This is a more complete phase diagram that shows better agreement with experimental results than has been previously reported. STM imaging of a surface exhibiting an A- (1×3) RHEED pattern indicates that this pattern is the result of coexistence between 4×3 or $c(2\times 6)$ and $c(4\times 4)$ reconstructions. The MC calculations suggest that this is possible because 4×3 , $c(2\times 6)$, and $c(4\times 4)$ reconstructions are predicted to be close in surface energy. Next, DFT calculations of the surface reconstructions stabilized by As on InSb are presented in Section 4.3.2. The calculated surface reconstruction phase diagram indicates that As and Sb are driven to intermix through As infiltrating the subsurface layer of the InSb crystal to form

configurations of the $\alpha(4\times 3)$ reconstruction. RHEED experiments confirm that the 4×3 surface persists under a variety of substrate temperatures, and As_2 and Sb fluxes. These experiments also provide further evidence that the A-(1×3) pattern is the result of phase coexistence between 4×3 and c(4×4) reconstructions. At elevated temperature, the 4×3 is not accessible, but the spacing between intermediate streaks of the A-(1×3) approaches the even spacing of an $n\times 3$ pattern with increasing As_2 flux. RHEED also indicates that As_2 roughens the surface through the formation of facets under Sb-poor conditions. These experimental results are evidence of As-for-Sb exchange at the surface. Sb-for-As exchange is also observed as all of the RHEED pattern transitions can be reversed by removing the As_2 flux and annealing under a sufficiently high Sb flux.

4.3.1 *Newly Calculated InSb Surface Reconstructions and Evidence of Surface Phase Coexistence*

The atomic scale details of the InSb surface are explored in this section comparing density functional theory and Monte Carlo calculations to RHEED and STM experiments. The reconstructions of InSb (001) surfaces are discussed first. DFT and MC calculations predict 2×4 and c(4×4) surface reconstructions that have not previously been predicted computationally for InSb, but are in agreement with experimental results. This provides a more complete thermodynamic understanding of the InSb surface than has been available in the literature. Next, STM indicates that the widely observed A-(1×3) RHEED pattern is the result of coexistence between c(4×4) and 4×3 and/or c(2×6) reconstructions. This is supported by the small surface energy difference between these reconstructions on the MC phase diagram.

The 0K surface energies of various surface reconstructions on InSb(001) as a function of Sb chemical potential, μ_{Sb} , were found using DFT calculations and are shown in Figure 4.2a. This phase diagram is in better agreement with experimental results than past reports. The phase diagram is bounded at low μ_{Sb} by the formation of bulk In at the surface and at high μ_{Sb} by the

formation of bulk Sb at the surface. The stable reconstructions are the In-rich $\zeta(4\times 2)$ at the lowest values of μ_{Sb} , followed by the stoichiometric (no surface excess of group-III or group-V atoms) $\alpha 2(2\times 4)$ at somewhat higher μ_{Sb} . Next, the surface is characterized by the group-V-rich $\alpha 3c(4\times 4)$ ³, which is terminated by 3 In-Sb heterodimers, and the completely Sb-terminated $c(2\times 6)$ at the highest values of μ_{Sb} . These reconstructions are shown schematically in Figure 4.2b. This phase diagram is notably different from a previous *ab initio* study [34] in which only the $\zeta(4\times 2)$, $\alpha(4\times 3)$, and $c(2\times 6)$ were reported to be stable. However, that study considered neither the $\alpha 2(2\times 4)$ nor the $\alpha 3c(4\times 4)$. Incidentally, this structure has also been predicted to be stabilized by Sb in both dimer and subsurface sites on InAs (Section 3.3.1), so it is perhaps not so peculiar to appear on the InSb surface phase diagram. In agreement with the previous study, the completely Sb-terminated $c(4\times 4)$ is not predicted to be stable. These calculations provide a more complete computational surface reconstruction phase diagram than has previously been available. Indeed, this phase diagram agrees with reports of the appearance of a $c(4\times 4)$ structure [13,28,77–79] with high Sb flux and/or low substrate temperature (corresponding to moderate to high Sb chemical potential), and one report of a 2×4 that arose during heating of an InSb $c(4\times 4)$ surface under an Sb flux [13].

³ See Section 4.2.3 for a summary of nomenclature

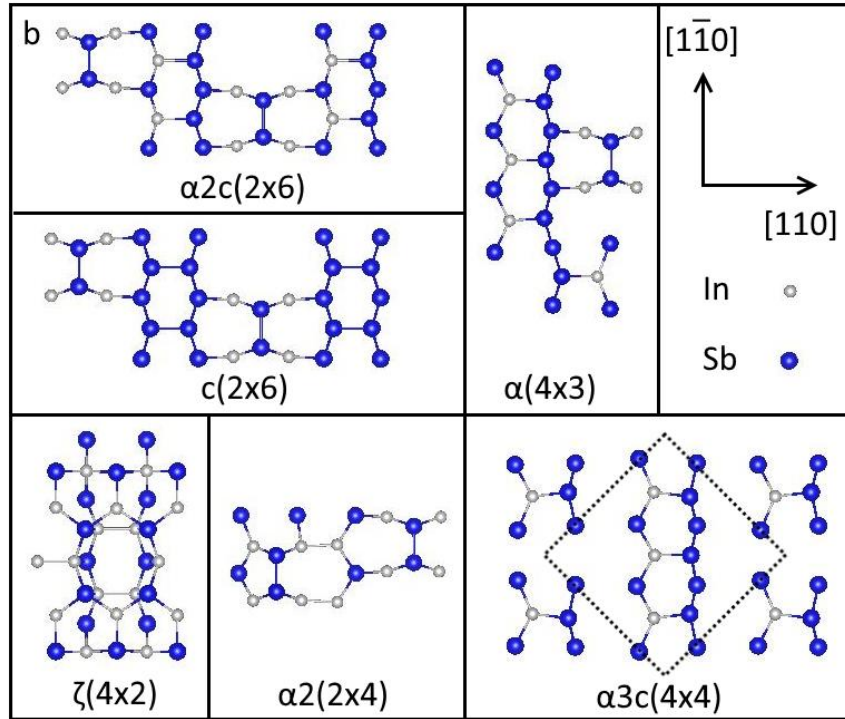
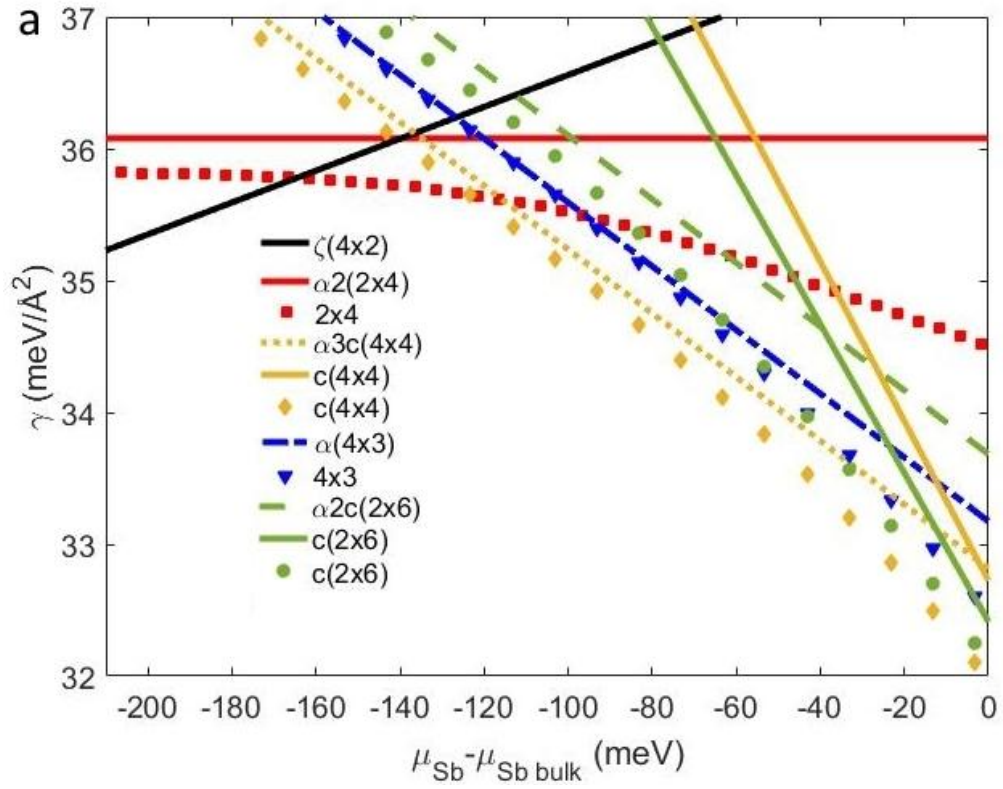


Figure 4.2. a. Calculated surface energies of InSb (001) as a function of Sb chemical potential from DFT at 0K (curves) and MC at 700K (points). b. Schematics of InSb (001) surface reconstructions.

While the calculated phase diagram agrees well with experiments, there is still an apparent discrepancy. This reconstruction phase diagram (Figure 4.2) does not contain a single reconstruction that would be consistent with an “asymmetric” 1×3 , or $A-(1 \times 3)$, RHEED pattern, which has been observed under a variety of experimental conditions [33,77,79,80]. Unlike an evenly spaced $n \times 3$ RHEED pattern, the two intermediate streaks of the $A-(1 \times 3)$ have a spacing less than $1/3$ times the distance between the primary streaks. In the past, the $A-(1 \times 3)$ had been hypothesized to be made up of domains of 2×4 cells [77,79], though STM imaging of the $A-(1 \times 3)$ indicates smaller spacing between rows on the surface than would be expected for a 2×4 reconstruction [33]. An alternative 1×3 cell containing an un-dimerized In atom was proposed [33], but more recent DFT calculations indicated that this structural prototype has a very high surface energy [34]. While the present DFT calculations predict the $\alpha 3c(4 \times 4)$ to dominate the phase diagram, two analogous structures, the $\alpha 2c(2 \times 6)$ and the $\alpha(4 \times 3)$, were calculated as potential candidates for the $A-(1 \times 3)$ reconstruction. These three reconstructions (Figure 4.2b) are similar in that they all contain a row of aligned In-Sb heterodimers and have the same surface excess Sb concentration, though $\alpha 2c(2 \times 6)$ and $\alpha(4 \times 3)$ were predicted to have higher surface energy than $\alpha 3c(4 \times 4)$ at all μ_{Sb} . This fact and the high, narrow μ_{Sb} range of stability for the $c(2 \times 6)$ suggests that none of these reconstructions are sufficient to explain the $A-(1 \times 3)$ on their own and that the structure causing an $A-(1 \times 3)$ RHEED pattern is more complex.

Grand canonical MC simulations were performed at 700K, shown as points in Figure 4.2a, to investigate whether configurational entropy at finite temperature would stabilize a 4×3 or $c(2 \times 6)$ surface at the range of μ_{Sb} between $\zeta(4 \times 2)$ and $\alpha 3c(4 \times 4)$. Instead, these calculations show that the 2×4 and $c(4 \times 4)$ reconstructions are further stabilized by configurational entropy. Because the MC simulations are based on surface cells that were required to be small and compatible with DFT

calculations, random coexistence between structural prototypes could not be simulated. The MC simulations decreased the surface energy of the 2x4 reconstructions enough to increase their stability relative to the other reconstructions. This is unexpected because there is only one report of an InSb 2x4 [13], while the A-(1x3) and c(4x4) have been more commonly observed experimentally [13,28,33,77–80]. The c(4x4) reconstructions also decreased in surface energy to the point that the c(2x6) surface is no longer the lowest energy structure at high μ_{Sb} , though this energy difference is only approximately $0.1 \text{ meV}/\text{\AA}^2$. However, this result might explain why there are no reports in the literature of experimental observations of an InSb c(2x6) surface. The increasingly negative slope of the c(4x4) surface energy indicates that this reconstruction becomes more Sb-rich at finite temperature, consistent with STM observations of coexistence between c(4x4) cells containing varying numbers of In-Sb heterodimers [33].

RHEED and STM experiments were conducted to confirm the calculated InSb phase diagram and gain further insight into the structure of the A-(1x3) surface. These results reveal that the A-(1x3) RHEED pattern is the result of coexistence between c(4x4) and 4x3 and/or c(2x6) surface reconstructions. In agreement with previous reports [33,78], InSb A-(1x3) and c(4x4) RHEED patterns were observed in the present work, which are discussed in Section 4.3.2. To experimentally investigate atomic scale details of the InSb surface, an sample was grown for STM imaging. This sample was prepared by first depositing 1.0 ML of In, which produced the expected 4x2 RHEED pattern. A low Sb flux of 7.3×10^{-8} torr was applied to this surface with the goal of creating a 2x4 RHEED pattern from an In-rich surface similarly to how an Sb-terminated $\alpha 2(2 \times 4)$ was created on InAs in Section 3.3.2. However, this resulted in an A-(1x3) surface instead. An STM image of this surface and its RHEED pattern are shown in Figure. 4.3. This surface is dominated by meandering rows of atoms separated by $11.0 \pm 0.7 \text{ \AA}$, which is approximately 2.4

times the magnitude of the $[110]$ and is consistent with the spacing between the intermediate streaks on the RHEED image. These agree with a previous STM report of the A -(1×3) pattern that showed meandering and similar spacing [33]. Additionally, unlike the previous study there appear to be small regions of the c (4×4), which appear as a brick-like motif (circled in Figure. 4.3a) scattered across the surface, indicating that there are multiple reconstructions present.

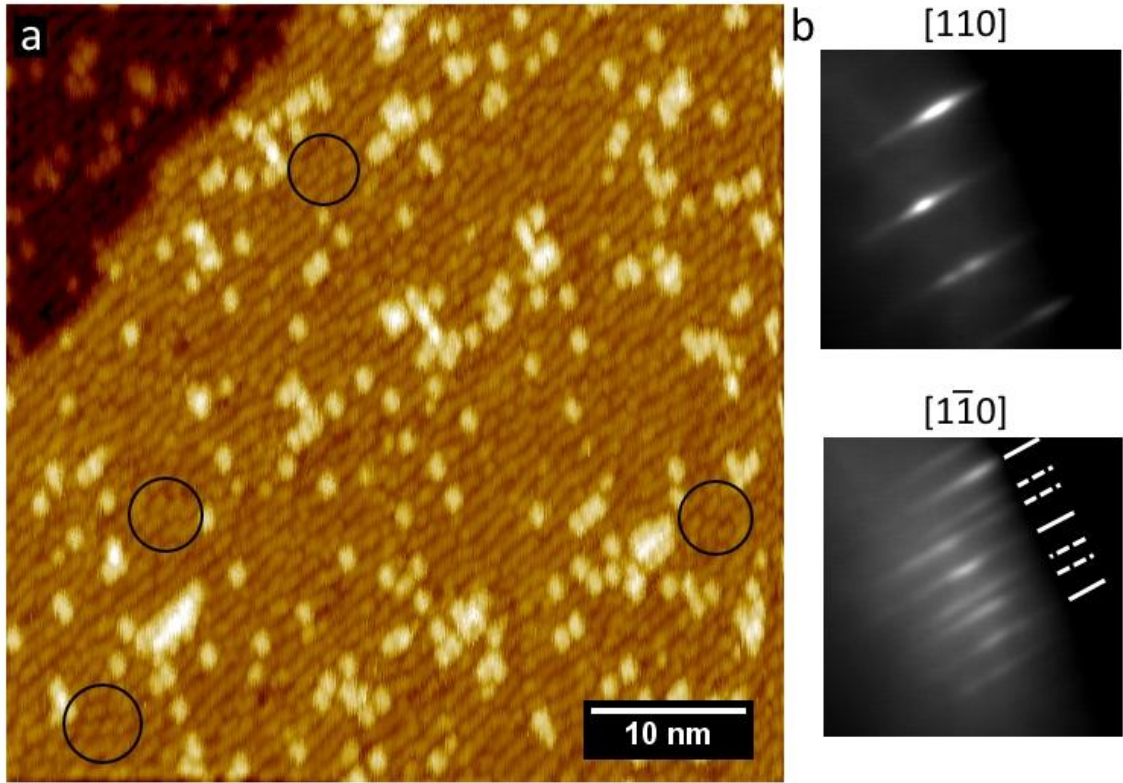


Figure. 4.3. a. Filled state (-2.7 V) STM image of InSb after exposing 1.0 ML of In to Sb at 395°C. A few c (4×4)-like regions are circled. b. A -(1×3) RHEED pattern for this sample. Primary and secondary streaks are marked with solid and dashed lines, respectively.

This observation of c (4×4) regions on a surface exhibiting an A -(1×3) diffraction pattern (Figure. 4.3) indicates that the A -(1×3) is not the result of a single reconstruction, but coexistence between different reconstructions. Coexistence between A -(1×3) and c (4×4) have been observed in a previous LEED and He scattering study [80]. However, that study did not examine the atomic scale details of the InSb surface and in that study, it was assumed that the A -(1×3) pattern arises

from a single reconstruction. It is proposed instead that the A-(1x3) is not a surface reconstruction *per se*, but coexistence between an $\alpha(4\times3)$ and/or $c(2\times6)$ structure and a $c(4\times4)$ structure, where increasing coverage of $c(4\times4)$ cells would account for the gradual surface transition. While the DFT and MC phase diagrams (Figure 4.2a) predict the $c(4\times4)$ reconstructions to be stable, the $\alpha(4\times3)$ is less than 0.5 meV/Å higher in surface energy. In addition, the $\alpha 2c(2\times6)$ is less than 1.0 meV/Å higher in surface energy, with the completely Sb homodimer terminated $c(2\times6)$ reconstruction having even lower surface energy at approximately $\mu_{\text{sb}} = -40$ meV. These energy differences further decrease with the In-Sb substitution allowed by the finite temperature MC simulations. This energy difference would be easily surmountable by thermal energy at experimental temperatures and the additional entropic decrease in surface energy that could be caused by coexistence between different surface reconstructions, which is beyond the scope of these simulations. A random distribution of $c(4\times4)$ cells, which have features separated by twice the magnitude of the [110], with 4×3 or $c(2\times6)$ cells could account for the average spacing of approximately 2.4 times the magnitude of the [110] the between rows as measured from the STM (Figure. 4.3). Additionally, the A-(1x3) fractional order streak spacing has been shown to decrease with increasing substrate temperature [77], which is consistent with a disordered surface. Coexistence between these phases might also contribute to the difficulty in experimentally preparing an InSb 2×4 surface, which is well ordered and would be a lower entropy state than coexistence between $\alpha(4\times3)$ or $c(2\times6)$ reconstructions (at lower or higher μ_{sb} , respectively) and $c(4\times4)$ reconstructions. The formation of an InSb 2×4 surface might be kinetically limited as well. It has only been observed as a transition from the Sb-rich $c(4\times4)$ side of the phase diagram [13], rather than from the $\zeta(4\times2)$ on the In-rich side of the phase diagram or from film growth, which occurs under conditions that are relatively In-rich compared to the $c(4\times4)$ surface.

The results of this section have provided further insights into the atomic structure of the InSb (001) surface. DFT and MC calculations have generated a surface reconstruction phase diagram that is more complete than previously available in the literature. This new phase diagram includes 2×4 and $c(4\times 4)$ reconstructions that agree with reported experimental results. STM measurements have shown that the widely observed A-(1×3) RHEED pattern, rather than being the result of a single reconstruction, is caused by coexistence between 4×3 or $c(2\times 6)$ reconstructions and $c(4\times 4)$ reconstructions. This is supported by the small surface energy difference between these reconstructions on the calculated phase diagram.

4.3.2 *As-Sb Intermixing and As-Induced Roughening on the InSb Surface*

The present investigation was extended by including *ab initio* calculations and RHEED experiments investigating the interaction between As and Sb on the InSb surface. The DFT calculations show that the widely observed As-for-Sb exchange [15–19] has a thermodynamic driving force. Various configurations of the $\alpha(4\times 3)$ reconstruction, a structure consistent with the $n\times 3$ RHEED pattern often observed during InAsSb growth [2,28,63,64], are stabilized by As atoms infiltrating the crystal. The DFT calculations also predict nearly stoichiometric 2×4 reconstructions to be stabilized by As, suggesting that InAsSb can be grown under such a surface, rather than a highly anion-rich surface. RHEED experiments confirm the stability of an $n\times 3$ RHEED pattern under concurrent As_2 and Sb fluxes. At elevated temperatures, instead of the $n\times 3$ pattern, the A-(1×3) pattern is observed under. The fractional spacing between the intermediate streaks of the A-(1×3) are found to increase and approach the even spacing of the $n\times 3$ pattern with increasing As_2/Sb BEPR. This observation is further support for the argument presented in Section 4.3.1 that the A-(1×3) pattern indicates a surface of coexisting 4×3 and $c(4\times 4)$ reconstructions. Under sufficiently As-rich conditions, the surface is roughened through the formation of facets, which is

further evidence for As-for-Sb exchange. All of the RHEED pattern transitions and the faceting are reversible under sufficiently high Sb flux, which is evidence of Sb-for-As exchange under As-poor conditions, consistent with previous reports [13,20].

The 0K DFT surface reconstruction phase diagram of As:InSb is shown in Figure 4.4 and contains several reconstructions stabilized by subsurface As, indicating a thermodynamic driving force for As-Sb intermixing. The phase diagram is bounded on the left by the formation of bulk In at low μ_{Sb} , at the top by the formation of bulk As at high μ_{As} , on the right by the formation of bulk Sb at high μ_{Sb} , and at the bottom by arbitrarily low μ_{As} . The bottom of this phase diagram, effectively in the absence of As, is identical to the pure InSb DFT phase diagram presented above in Figure 4.2a. The As:InSb phase diagram is dominated by anion-rich reconstructions, namely various configurations of $\alpha(4\times3)$, $c(4\times4)$, and $c(2\times6)$ reconstructions. Three configurations of $\alpha(4\times3)$, all of which are stabilized by subsurface As (Figure 4.4), occupy the majority of chemical potential space. Increasing μ_{As} from either the $\alpha 2(2\times4)$ or $\alpha 3c(4\times4)$, these configurations are $\alpha(4\times3)s2^+$, $\alpha(4\times3)s4$, and $\alpha(4\times3)s6$. These configurations increase in As content with increasing μ_{As} , as would be expected. Interestingly, the order in which subdimer sites are filled proceeds with the two group-V sites below the In row, followed by the two group-V sites below the In atom in the kink dimer, finally followed by the remaining group-V sites below surface In row. None of the of the dimer sites are filled by As, thus As only bonds with In atoms in these reconstructions. The $c(2\times6)$ also has only subdimer As substitution with increasing μ_{As} , with a maximum of two subdimer-As atoms diagonally across a trench dimer from each other in $c(2\times6)s2/2^+$.

The surface reconstruction phase diagram (Figure 4.4) shows that there is a thermodynamic driving force for As-Sb intermixing on InSb through the fact that all of the double anion layer

⁴ See Section 4.2.3 for a summary of nomenclature.

reconstructions have configurations that are stabilized by subsurface As. As intermixes with InSb, forming stable surface reconstructions by infiltrating the surface and replacing Sb atoms, which lowers the surface energy of the configuration because the In-As bond is stronger than the In-Sb bond [69]. These reconstructions that are stabilized by As infiltrating the InSb crystal are consistent with reports As-for-Sb exchange [15–19]. Additionally, all of these reconstructions, except for the $\alpha 3c(4 \times 4)3s6$ at high μ_{As} and low μ_{Sb} , lack As in the dimer sites. This is consistent with observations of Sb on InAs (Section 3.3.1) where Sb has a preference for first substituting on dimer sites before infiltrating the subsurface anion layer; μ_{Sb} needs to be high relative to μ_{As} for Sb to occupy subdimer sites in either system. Sb remains in the dimer sites presumably because of the higher surface energy of InAs compared to InSb. Thus, these calculations are also consistent with experimental observations of Sb segregation [23,25,62]. It is noteworthy that the onset of As infiltration of the surface occurs at very low μ_{As} . For instance, $\alpha(4 \times 3)$ reconstructions are stabilized by $\mu_{\text{As}} \geq -190$ meV, which might contribute to the experimental prevalence of A-(1x3) RHEED pattern. The low As chemical potential need to form the $\alpha(4 \times 3)s2$ suggests that the background As partial pressure in a typical MBE chamber might be sufficient to create As-containing 4x3 surface cells coexisting with Sb-terminated $c(4 \times 4)$ cells on a real surface. This might also explain one report of an InSb 1x3 surface prepared in an As-containing growth chamber [13], rather than the A-(1x3) that is more typically observed.

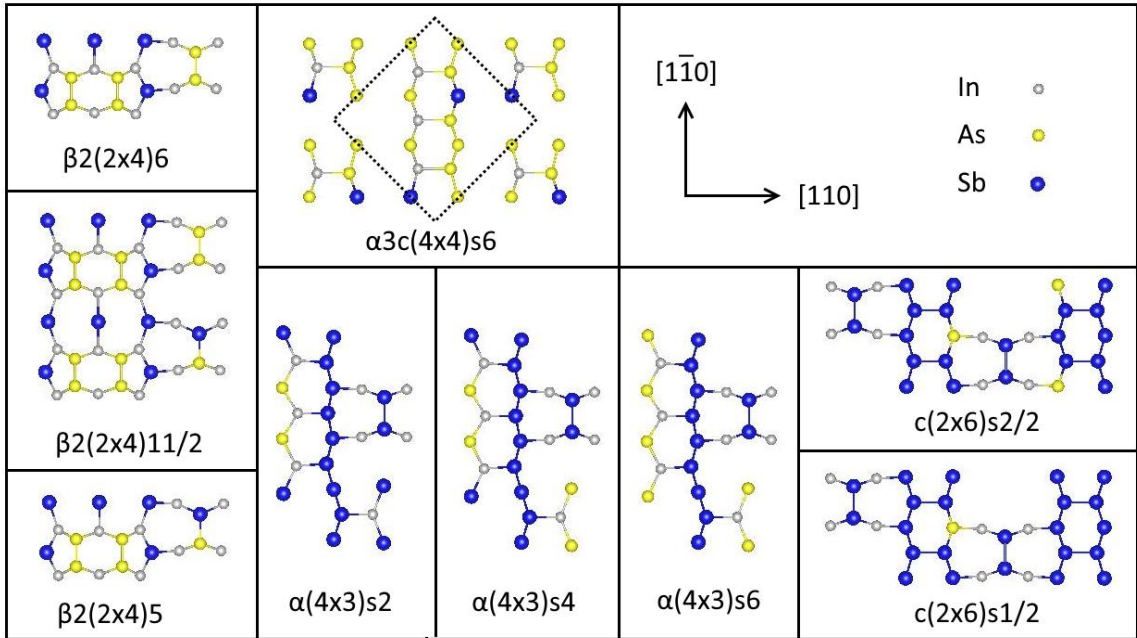
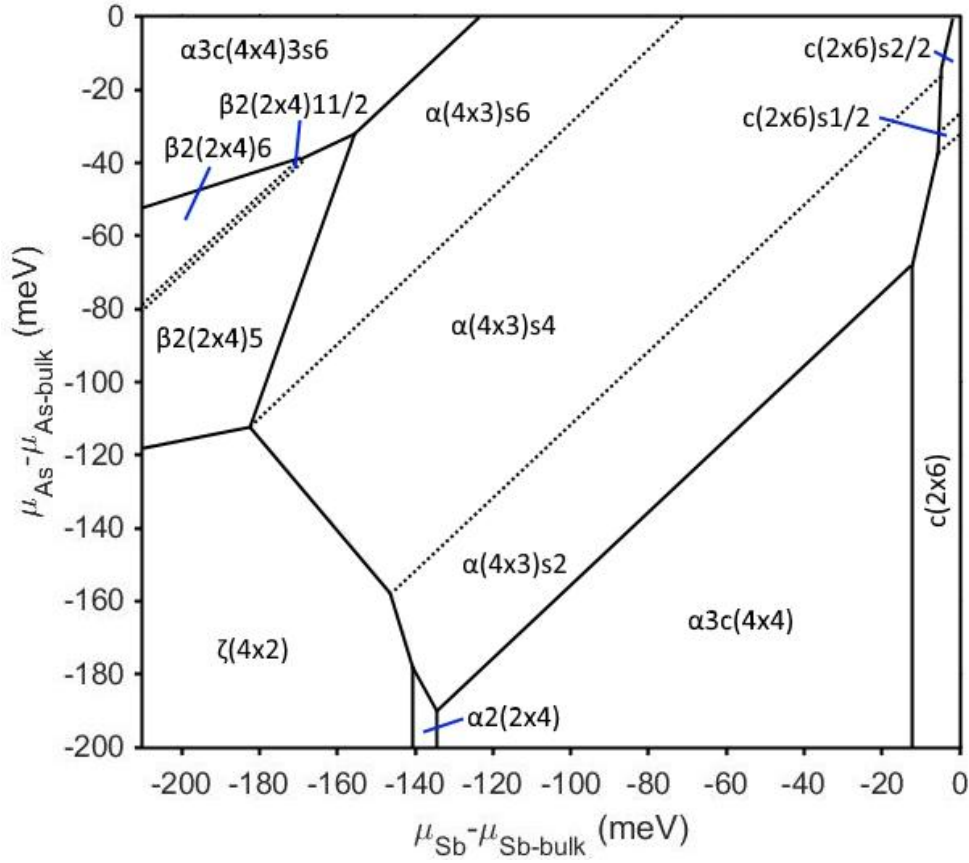


Figure 4.4. Top: 0K DFT surface reconstruction phase diagram of As:InSb as a function of As and Sb chemical potentials. Bottom: schematics of the As-containing reconstructions on the DFT phase diagram. Some atoms are removed and some atoms are duplicated for clarity.

The remaining reconstructions in Figure 4.4 have configurations that contain As in dimer sites, which is further evidence that As-Sb intermixing occurs through the formation of alloyed surface reconstructions. Some of these alloyed configurations are highly anion-rich while others are nearly stoichiometric, consistent with the DFT results in CHAPTER 3, suggesting that the surface stoichiometry can be controlled during film growth. Three As-terminated $\beta 2(2 \times 4)$ configurations are stabilized by As at low μ_{Sb} and increase in As concentration from 5 dimer sites filled by Sb in $\beta 2(2 \times 4)5^5$ to all dimer sites being occupied by Sb in $\beta 2(2 \times 4)6$ with increasing μ_{As} . The $\beta 2(2 \times 4)11/2$, which is stable for a narrow range of μ_{As} , is a supercell consisting of one unit cell of each $\beta 2(2 \times 4)5$ and $\beta 2(2 \times 4)6$. The prediction of As-stabilized $\beta 2(2 \times 4)$ reconstructions, along with previous DFT predictions and STM observations of Sb-stabilized $\alpha 2(2 \times 4)$ reconstructions on InAs (CHAPTER 3), suggest that InAsSb might be able to be grown under a nearly stoichiometric surface for the full compositional range. Further increasing μ_{As} from $\beta 2(2 \times 4)6$ produces the most As-rich reconstruction predicted, $\alpha 3c(4 \times 4)3s6$, which features 6 subsurface Sb atoms and is terminated by 3 In-As heterodimers. The presence of a Sb-As heterodimer in each $\beta 2(2 \times 4)5$ and $\beta 2(2 \times 4)11/2$ and the presence of As in both the dimers and subsurface layer of $\alpha 3c(4 \times 4)3s6$ are further evidence for a thermodynamic driving force for As-Sb intermixing.

RHEED experiments of a static InSb surface, that is, without an applied In flux, were conducted to confirm the predicted reconstructions on the As:InSb DFT phase diagram (Figure 4.4) and identify the conditions for transitions between RHEED patterns. These experiments confirm the prediction of As-stabilized 4×3 reconstructions and As infiltration of the crystal through the formation of facets. These experiments provide evidence of As-for-Sb exchange under As-rich conditions and evidence of Sb-for-As exchange under Sb-rich conditions. The results of a series of

⁵ See Section 4.2.3 for a summary of nomenclature.

experiments applying various Sb and As₂ fluxes to an InSb surface at 330°C to 445°C are summarized in Table 4.1, with the beam equivalent pressure ratio (BEPR) tabulated when applicable. Each instance of the growth temperature listed on the table denotes a new series of experiments conducted on a freshly grown InSb buffer layer at least 250 nm thick. All experiments commenced by recording the RHEED pattern without any applied flux. Note that only fluxes that caused a surface phase transition are tabulated; incremental changes in fluxes between these points are omitted. The experiments conducted at 330°C are discussed first, as all of the RHEED patterns observed in the present work were accessible at this temperature. The paths of increasing and decreasing fluxes applied to the surface is illustrated in Figure 4.5. Rather than creating streaky RHEED patterns, applying only an As₂ flux $\geq 7.2 \times 10^{-8}$ torr roughens the surface by creating facets, which appear as chevrons on the RHEED screen. Interestingly, this faceting is reversible; the faceted surface transitions to a streaky nx3 RHEED patterns by removing the As₂ flux while applying an Sb BEP = 8.0×10^{-8} torr. Further increasing the Sb flux results in the surface reverting to the original Sb-terminated A-(1x3) pattern. This transition is evidence of Sb-for-As exchange at the surface and consistent with reports in the literature of this phenomenon under Sb-rich conditions [13,20]. Increasing the Sb flux to 2.19×10^{-7} torr results in the expected c(4x4) RHEED pattern, which persists at higher Sb fluxes. Under an Sb BEP = 2.19×10^{-7} torr, the c(4x4) transitions to an evenly spaced nx3 pattern upon application of a small As₂ flux of 7.2×10^{-8} torr. The evenly spaced nx3 patterns are indicative of 4x3 reconstructions [67]. An additional increase in the As₂ flux to 1.35×10^{-6} torr causes spots to appear on top of the nx3 pattern, indicating roughening through the formation of 3D features on the surface. This spotty pattern is consistent with a previous report [13] and possibly the onset of faceting. Similar results to those observed at 330°C for the formation of A-(1x3), evenly spaced nx3, and chevrons were observed at substrate temperatures up to 445°C as well.

Table 4.1. RHEED Pattern of InSb After Exposure to As and Sb Fluxes.

Temperature (°C)	Initial RHEED	Sb BEP (torr)	As ₂ BEP (torr)	As ₂ /Sb BEPR	Final RHEED
330	A-(1x3)	0	7.2×10^{-8}		chevrons
	chevrons	8.0×10^{-8}	0		nx3
	nx3	2.19×10^{-7}	0	0.00	A-(1x3)
	A-(1x3)	3.27×10^{-7}	0	0.00	c(4x4)
	c(4x4)	4.74×10^{-7}	7.2×10^{-8}	0.15	nx3
	nx3	4.74×10^{-7}	1.35×10^{-6}	2.85	spotty/nx3
350	A-(1x3)	0	4.4×10^{-8}		chevrons
	chevrons	3.25×10^{-7}	4.4×10^{-8}	0.13	spotty/nx3
	spotty/nx3	3.25×10^{-7}	0	0.00	A-(1x3)
380	A-(1x3)	0	1.31×10^{-7}		chevrons
	chevrons	7.71×10^{-7}	1.31×10^{-7}	0.17	spotty/chevrons
	spotty/chevrons	7.71×10^{-7}	0	0.00	A-(1x3)
400	A-(1x3)	7.63×10^{-7}	0	0.00	A-(1x3)
	A-(1x3)	7.63×10^{-7}	7.73×10^{-7}	1.01	nx3
	nx3	7.63×10^{-7}	1.56×10^{-6}	2.04	spotty/nx3
425 (i)*	4x2	9.7×10^{-8}	0		A-(1x3)
	A-(1x3)	1.26×10^{-6}	2.36×10^{-6}	1.87	chevrons
	chevrons	1.26×10^{-6}	0	0.00	chevrons
425 (ii)*	4x2	7.84×10^{-7}	0	0.00	A-(1x3)
	A-(1x3)	7.84×10^{-7}	1.51×10^{-6}	1.93	chevrons
	chevrons	7.84×10^{-7}	0	0.00	chevrons
425 (iii)*	4x2	0	1.35×10^{-7}		chevrons
	chevrons	5.58×10^{-7}	1.35×10^{-7}	0.24	chevrons
	chevrons	5.58×10^{-7}	0	0.00	A-(1x3)
	A-(1x3)	5.58×10^{-7}	1.35×10^{-7}	0.24	A-(1x3)
	A-(1x3)	8.2×10^{-8}	1.35×10^{-7}	1.64	A- (1x3)/chevrons
	chevrons	6.40×10^{-7}	0	0.00	A-(1x3)
445	A-(1x3)	1.28×10^{-6}	0	0.00	A-(1x3)
	A-(1x3)	1.28×10^{-6}	1.77×10^{-6}	1.38	chevrons
	chevrons	1.28×10^{-6}	0	0.00	A-(1x3)

* The roman numerals correspond to the data series in Figure 4.6.

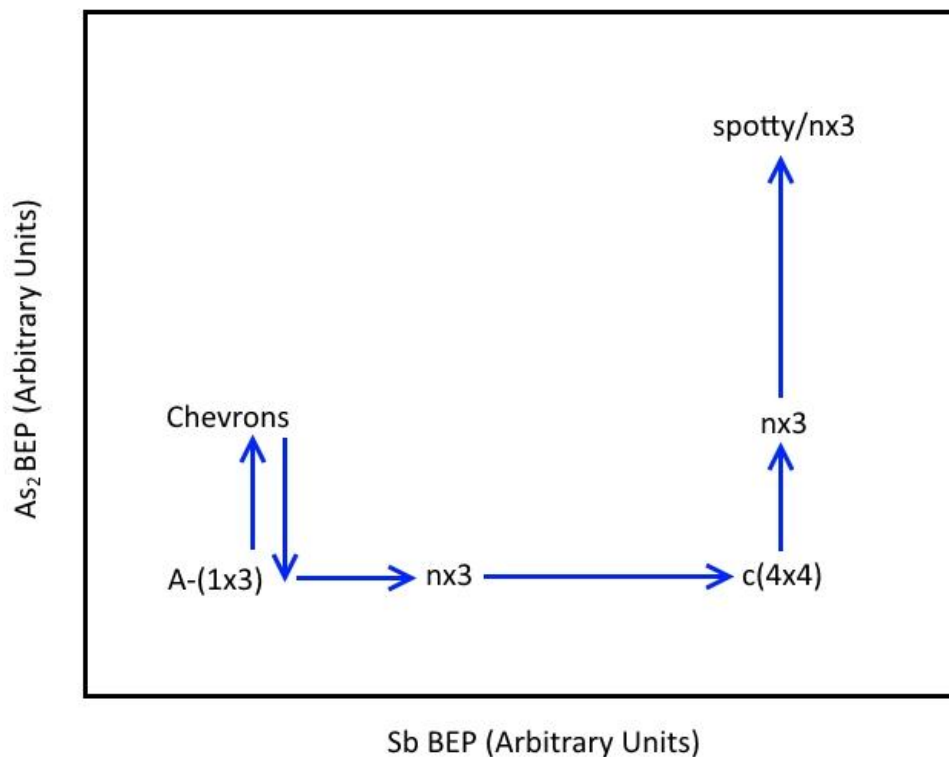


Figure 4.5. Schematic of how As₂ and Sb fluxes were applied for the experiments at 330°C summarized in Table 4.1.

Examining the results at all of the temperatures considered in this work (Table 4.1) reveals further details about the transitions between surface reconstructions for the As:InSb system as a function of As₂ and Sb fluxes. Several experimental conditions result in an nx3 RHEED pattern, which confirms the DFT predictions that the phase diagram is dominated by various configurations of the $\alpha(4 \times 3)$ reconstruction (Figure 4.4). For instance, at 330°C, applying an Sb flux of 8.0×10^{-8} torr causes the faceted surface to transition to a streaky nx3 pattern after the As₂ that created the facets has been removed. This occurrence of an nx3 pattern, which is not observed for pure InSb, suggests that residual As at the surface was sufficient to produce an alloyed surface. This is supported by the DFT predictions that an As-stabilized 4x3 reconstruction can form with very little As, or low μ_{As} . The transition from the c(4x4) pattern to an nx3 pattern provides additional evidence supporting the DFT calculations. Consistent with the DFT predictions, which show that

the $\alpha 3(c4 \times 4)$ can transition to $\alpha(4 \times 3)_2$ at moderate μ_{Sb} and low μ_{As} , the transition from a $c(4 \times 4)$ to an $nx3$ RHEED pattern occurs at a moderate Sb BEP = 4.74×10^{-7} torr and low As_2 BEP = 7.2×10^{-8} torr. This $nx3$ persisted up to an As_2 BEP = 1.35×10^{-6} torr, at which point spots started appearing on the RHEED screen, suggesting the onset of faceting. The $nx3$ RHEED was also observed at 400°C under an As_2/Sb BEPR of 1.01 (Table 4.1). These conditions are not exhaustive, but because the $nx3$ pattern is accessible at several different substrate temperatures; from various initial surface such as a faceted surface, an $A-(1 \times 3)$, or a $c(4 \times 4)$; and at various Sb/ As_2 BEPRs, the $nx3$ pattern likely occupies a large region of phase space. This is in agreement with the DFT calculations (Figure 4.4), which show that much of the phase diagram is occupied by As-containing $\alpha(4 \times 3)$ configurations. This is also consistent with reports of InAsSb growth [2,63,64] exhibiting an $nx3$ pattern and RHEED observations of a static InAs surface displaying an $nx3$ pattern under Sb-rich conditions, as discussed in CHAPTER 3.

These experiments at elevated temperatures provide additional evidence that the $A-(1 \times 3)$ RHEED pattern is the result of coexistence between 4×3 and $c(4 \times 4)$ reconstructions. Instead of observing an $nx3$ at temperatures above 400°C, the $A-(1 \times 3)$ pattern was observed under concurrent Sb and As_2 fluxes before the onset of faceting (Table 4.1). However, the fractional spacing between the intermediate streaks of the $A-(1 \times 3)$ RHEED pattern were observed to increase and approach the even spacing of the $nx3$ with increasing As_2/Sb BEPR at both 425°C (Figure 4.6) and 445°C before faceting occurred. The measured fractional spacing increases from approximately 0.22 to 0.31, nearly the 0.33 spacing of an $nx3$ pattern. Furthermore, this trend continues under a variety of absolute fluxes, for both increasing As_2 flux (series i and ii) and decreasing Sb flux (series iii), implying that this is a thermodynamic, rather than kinetic effect. This trend further supports the argument presented in Section 4.3.1 that the $A-(1 \times 3)$ is the result of coexistence between 4×3

and $c(4 \times 4)$ unit cells. Reviewing the DFT phase diagram of As on InSb (Figure 4.4), it is clear that under moderate μ_{Sb} , increasing μ_{As} causes a transition to a 4×3 reconstruction. In chemical potential space, this transition is abrupt. However, experimentally, the fluxes of As and Sb are controlled instead, which are more directly related to the concentration of each species at the surface. This suggests that the transition from an A-(1×3) to an evenly spaced $n \times 3$ pattern does not proceed immediately once a sufficient concentration of As is supplied. As the As_2/Sb BEPR is increased, the $c(4 \times 4)$ cells of the A-(1×3) are consumed to form more 4×3 cells. As the fraction of the surface covered by 4×3 unit cells increases at the expense of $c(4 \times 4)$ cells, the average spacing between surface cells increases to match that of the 4×3 , which is manifested in the increased streak spacing in the RHEED pattern.

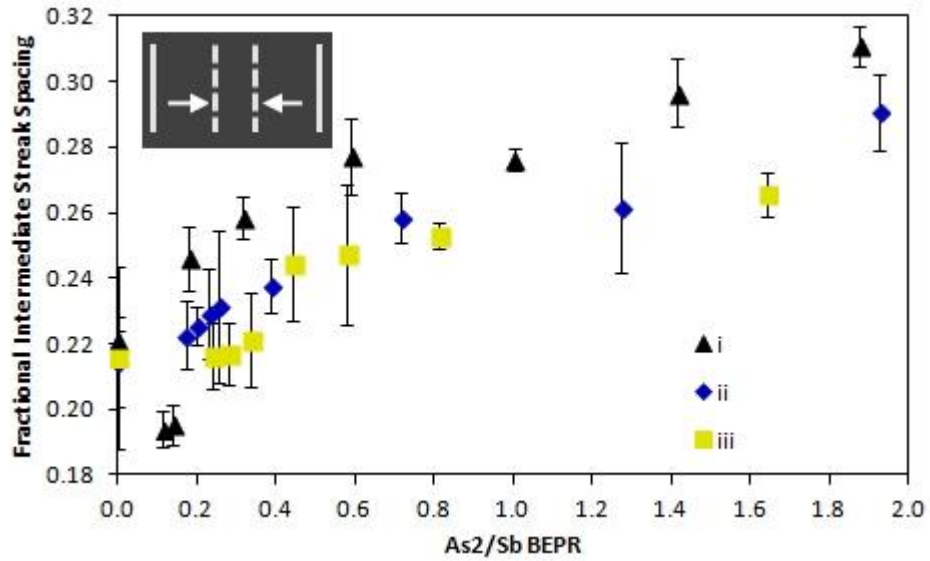


Figure 4.6. Plot of A-(1×3) intermediate streak spacing at 425°C as a function of As_2/Sb BEPR. Inset illustrating which streaks were measured with dashed lines for fractional streaks and solid lines for primary streaks.

Error bars are \pm one standard deviation in the measurement of the streak spacing. The roman numerals refer to selected series of experiments from Table 4.1. Series i was conducted with constant Sb flux of 1.26×10^{-6} torr and increasing As_2 flux. Series ii was conducted with constant Sb flux of 7.84×10^{-7} torr and increasing As_2 flux. Series iii was conducted with constant As_2 flux of 1.35×10^{-7} torr with decreasing Sb flux.

Regardless of substrate temperature or initial RHEED pattern, exposing the surface to an As_2 flux alone resulted in surface roughening through the formation of facets. At most

temperatures, the A-(1x3) was observed in the absence of an applied flux, as expected. While this faceting might appear to contradict the As:InSb DFT phase diagram (Figure 4.4), three dimensional features are beyond the scope of the surface calculations conducted in the present study and such large scale features would be too computationally expensive for DFT. However, the DFT results still provide insight into the formation of the facets. Because many reconstructions are stabilized by subsurface As, it is probable that the creation of these facets is caused by As atoms infiltrating the substrate. This is also consistent with the fact that observations of As-for-Sb exchange are widely reported in the literature [15–19]. Additionally, faceting occurs under As₂ and Sb fluxes applied concurrently for sufficiently high As₂/Sb BEPRs at all substrate temperatures investigated (330–445°C). This suggests that rather than the accumulation of As at the surface, these faceted features consist of InAs or InAsSb. Interestingly, this faceting is reversible in many cases. For example, the faceted surfaces were returned to streaky A-(1x3) RHEED patterns by removing the As₂ flux while maintaining or increasing the Sb flux at all temperatures except 400°C. This is evidence of Sb-for-As exchange at the surface. Because of the reversibility of creating a faceted surface and the variety of growth conditions under which they occur, the size of the facets might be controllable. Thus, optimization of the substrate temperature, fluxes, and exposure time to control facet size and spatial distribution might provide a method of growing quantum dots as an alternative to droplet epitaxy or highly strained growth.

Despite being predicted by the DFT calculations (Figure 4.4), the As-terminated $\beta 2(2 \times 4)$ reconstructions were not observed by simply applying an As₂ flux to the Sb-terminated surface. Instead, exposing the as-grown InSb surface to As causes faceting, suggesting that the As-for-Sb exchange process is fast in the absence of an Sb flux. Thus, any $\beta 2(2 \times 4)$ domains that might have been created are quickly obscured by the facets. Instead, the As-terminated $\beta 2(2 \times 4)_6$ might be

accessible by first depositing 1.0 ML In, as was required to produce an Sb-terminated $\alpha 2(2 \times 4)4$ surface on InAs as was done in CHAPTER 3. As in that case, the increased In concentration might be required in order to provide an alternative reaction pathway. However in the case of As on InSb, this might a limited As exposure to prevent the As from rapidly depleting the surface In and infiltrating the substrate.

Additionally, the observations at 425°C suggest that the supplied Sb BEP= 1.28×10^{-6} torr (the maximum available in this MBE chamber) was insufficient to prevent the onset of faceting under a concurrent As₂ flux. All three experimental series at 425°C (Table 4.1) were conducted by increasing the As₂/Sb BEPR, though in different ways. This was accomplished in series i and ii by holding the moderate to high Sb flux constant while increasing the As₂ flux. Instead for series iii, the low As₂ flux was held constant while the Sb flux was decreased in order to increase the As₂/Sb flux ratio. This difference in procedure changed the flux ratio at which the surface started to roughen through the formation of facets. In series i and ii, the As₂/Sb BEPR that lead to faceting was approximately 1.9, while for series iii, this number decreased to approximately 1.6. This suggests that in order to prevent faceting, a sufficient Sb flux must be maintained to prevent As from infiltrating the crystal. Thus, an nx3 surface should be accessible at elevated temperatures by using an Sb flux greater than 1.28×10^{-6} torr, which was the maximum available for this study.

The results of this section provide greater understanding of the atomic scale details of the interaction between As and Sb in compound semiconductors. DFT calculations show that As is energetically driven to intermix with InSb through the formation of $\alpha(4 \times 3)$ surface reconstructions that are stabilized by subsurface As. RHEED experiments confirm that the phase diagram is dominated by this reconstruction. The RHEED experiments along with the DFT results provide further evidence that the A-(1x3) RHEED pattern is the result of coexistence between 4x3 and

$c(4\times 4)$ reconstructions and is partially stabilized by As. As is observed to roughen the surface of InSb through the formation of faceted features. This is consistent with previous reports of As-for-Sb exchange and the DFT calculations indicating that As tends to infiltrate the subsurface layer of the InSb crystal. Interestingly, this faceting is reversible under sufficiently Sb-rich conditions which is evidence of Sb-for-As exchange.

4.4 Conclusions

The atomic scale details of the interaction between As and Sb on InSb were investigated in this chapter. The DFT phase diagram of InSb indicates that anion-rich part of the calculated phase diagram is dominated by 2×4 and $c(4\times 4)$ reconstructions, which is in better agreement with experimental results than are previous calculations reported in the literature. Furthermore, the MC simulations show that the $c(4\times 4)$ reconstructions displace the $c(2\times 6)$ from the phase diagram, which explains the lack of experimental reports of an InSb $c(2\times 6)$. STM measurements show that the widely observed A-(1×3) RHEED pattern is the result of coexistence between 4×3 and/or $c(2\times 6)$ and $c(4\times 4)$ reconstructions. This is supported by the MC calculations that show only a small energy difference between these reconstructions. An *ab initio* surface reconstruction phase diagram of As:InSb provides evidence of a thermodynamic driving force for Sb-As intermixing through the phase diagram being dominated by three different compositional configurations of $\alpha(4\times 3)$ stabilized by subsurface As. As-rich $\beta 2(2\times 4)$ reconstructions are predicted as well, suggesting that InAsSb could be grown under a nearly stoichiometric surface. RHEED experiments confirm that the 4×3 reconstructions are stable under a variety of conditions. The RHEED experiments also provide further evidence that the A-(1×3) is the result of coexistence between 4×3 and $c(4\times 4)$ reconstructions. Increasing the As_2/Sb BEPR applied to an InSb surface causes the surface A-(1×3) RHEED pattern to become more $nx3$ -like, indicating an increase in the surface coverage of 4×3

reconstructions. Additionally, As is found to roughen the InSb surface by infiltrating the crystal and forming facets. The formation of facets is reversible by applying a sufficiently high Sb flux, which shows Sb-for-As exchange is favorable under Sb-rich conditions.

CHAPTER 5

Modifying the Surface of InAsSb with Bi as a Surfactant

5.1 Introduction

The previous two chapters discussed the compositional endpoints of the surface reconstructions of InAsSb system, namely Sb:InAs and As:InSb. This chapter extends that work by investigating a more complex system: Bi:InAsSb. The use of Bi as a surfactant during growth of InAsSb is shown to modify the interaction between Sb and As. This change in the Sb-As interaction is manifested in decreases in Sb incorporated into InAsSb films under increasing Bi fluxes.

Before discussing previous studies involving Bi as a surfactant, a review of the literature for InAsSb growth is needed. InAsSb is of interest for long wavelength infrared applications because it is a direct gap III-V semiconductor that can attain sufficiently narrow band gaps, depending on the composition [1]. In order to be used effectively in optoelectronic devices, the material must be grown with smooth interfaces, minimal defects, and be compositionally homogeneous. Recent work shows that fully relaxed InAsSb grown on compositionally graded buffer layers at 415°C is free of phase separation or ordering, even for high Sb compositions approaching 50% [1]. However, the optimum substrate temperature and III/V flux ratios have not been systematically investigated for these alloys. Further improvements could possibly also be obtained by the use of surfactants but their influence on the interaction between Sb and As the alloy composition must first be determined.

It has been suggested that the use of Bi as a surfactant may improve the crystal growth of certain III-V semiconductor alloys. For instance, growing GaNAs under a Bi flux results in smoother surfaces and higher N incorporation [29]. Similar effects were found for B incorporation in GaAs [30]. The use of a Bi surfactant has also been observed to inhibit In segregation and decrease interfacial roughness in InGaAs/GaAs [31]. Several mechanisms for these improvements have been proposed. One suggests that that surface Bi atoms prevent other growth processes by blocking otherwise reactive sites [31]. Another proposes that Bi displaces one anion in favor of the other [30]. The effect of Bi on the growth of InAsSb, on the other hand, has not been reported.

In this chapter, how the presence of a Bi flux influences the composition of InAsSb alloys grown via molecular beam epitaxy (MBE) was investigated. It was found that Sb incorporation is decreased with increasing Bi flux. A kinetic model has been developed that suggests that the suppression of Sb incorporation is due to a catalytic effect where Bi atoms on the surface are more likely to be replaced by impinging As atoms than impinging Sb atoms during growth.

5.2 Experimental Procedure

Two series of InAsSb films were grown on (001) oriented GaSb substrates in MBE chambers in two different labs. These series were grown at two different substrate temperatures and In, As, and Sb fluxes, which are summarized in Table 5.1. The growth parameters of each series were held constant, except for the applied Bi flux. The first series (Series A) was grown at the University of Michigan and the general procedure followed can be found in Section 2.3. The series A films were at 385 °C with $R_{\text{In}}=0.5$ ML/s, measured using, beam equivalent pressures (BEP) of 2.1×10^{-6} torr for As_2 , and 0.62×10^{-7} torr for Sb to a thickness of 4000 Å. The rates measured from reflection high energy electron diffraction (RHEED) oscillations corresponding to these BEPs are approximately $R_{\text{As}_2}=1.1$ ML/s and $R_{\text{Sb}}=0.1$ ML/s. These samples were grown

without GaSb buffer layers because previous buffer layers contained unintentional background As incorporation that complicated analysis of the nearly lattice matched InAsSb films. The second series (Series B) was grown at the Army Research Lab at 415 °C in an MBE chamber similar to the one used at U of M. The series B films were grown with $R_{\text{In}} = 0.9 \text{ ML/s}$, $5.7 \times 10^{-6} \text{ torr As}_2 \text{ BEP}$, and $1.2 \times 10^{-7} \text{ torr Sb BEP}$ to a thickness of 2500 Å or 5000 Å as noted. The Bi BEP was varied up to $2.6 \times 10^{-7} \text{ torr}$ in one laboratory (series A) and $4.8 \times 10^{-7} \text{ torr}$ in the other (series B). For series A, the In, As, and Sb fluxes were calculated by converting the rates measured from RHEED oscillations. For series B, the In, As, and Sb fluxes were calculated as described previously [82]; that is, by starving the growth surface of anions until a decrease in the growth rate was observed. Under these conditions, $V/\text{III}=1$, thus the anion flux is equal to the cation flux measured by RHEED oscillations. Alternatively, the anion incorporation rate can be determined using anion uptake oscillations [49,50], which correlate well to the anion starvation method. Bi fluxes could not be calculated using this approach because RHEED uptake oscillations were not observable, nor is the transition from anion to cation terminated surfaces known.

Table 5.1. Growth Conditions for InAsSb Films Grown on GaSb Substrates

	T (°C)	F_{In} ($\times 10^{14} \text{ cm}^{-2} \text{ s}^{-1}$)	F_{As_2} ($\times 10^{14} \text{ cm}^{-2} \text{ s}^{-1}$)	F_{Sb} ($\times 10^{14} \text{ cm}^{-2} \text{ s}^{-1}$)	Bi BEP ($\times 10^{-7} \text{ torr}$)	h (Å)
Series A	385	2.8	7.1	0.8	0.0	4000
		2.8	7.1	0.8	0.7	4000
		2.8	7.1	0.8	1.2	4000
		2.8	7.1	0.8	2.8	4000
Series B	415	5.0	15.1	1.4	0.0	2500
		5.0	15.1	1.4	1.0	5000
		5.0	15.1	1.4	2.6	5000
		5.0	15.1	1.4	4.8	5000

Post-growth characterization of the InAsSb films was conducted using two different techniques. Compositional analysis was conducted using high resolution x-ray diffraction (XRD)

and Rutherford Backscattering Spectrometry (RBS). The compositions were calculated for the samples using two (004) scans with a 180 degree rotation in phi and two (115) scans with a 180 degree rotation in phi and taken in glancing incidence and exit. Rutherford backscattering spectrometry (RBS) was used to confirm that no Bi had incorporated into the films. RBS experiments for this dissertation were conducted at the Michigan Ion Beam Laboratory (MIBL) on a tandem accelerator that bombarded the samples with He^{2+} ions with 1.89 MeV of energy at a normal incidence to the samples. A detector oriented 20 degrees from the sample normal measured the remaining kinetic energy of the backscattered He ions. The experimental RBS spectra were fit with simulated spectra for each elemental species using the SimNRA software [83,84].

5.3 Results and Discussion

In this section, the results of using Bi as a surfactant during MBE growth of InAsSb are discussed. The presence of Bi at the surface results in an nx3 RHEED pattern, indicative of an anion-rich surface. XRD and RBS characterization of the films suggests that Bi might improve the structural quality and compositional uniformity of the films. Furthermore, the Bi is found to decrease Sb incorporation in the films. A kinetic model for anion incorporation is employed to show that rather than acting as a steric barrier, Bi blocks Sb incorporation by catalyzing the formation of InAs.

5.3.1 *Decreased Sb Incorporation Caused by Bi Surfactant*

Each InAsSb film grown successfully for this investigation (Table 5.1) exhibited a streaky nx3 RHEED pattern, consistent with previous reports of InAsSb growth [2,28,63,64]. The fact that Bi caused this RHEED pattern is consistent with reports of Bi on GaAs [55], Bi on GaSb [39], and Bi on InSb [34], which have surface reconstruction phase diagrams with large regions of chemical potential space stabilizing 4x3 reconstructions, and in the case of Bi:InSb, c(2x6) reconstructions.

Thus, the Bi-induced surface reconstruction is likely a compositional variation of $\alpha(4\times3)$, $\beta(4\times3)$, $h0(4\times3)$, or $c(2\times6)$. Additional films were attempted using even higher Bi fluxes than those reported in Table 5.1. A Bi BEP= 1.5×10^{-6} torr at 405°C and with In, As, and Sb fluxes similar to those of series A resulted in a spotty RHEED pattern. This suggests that a high Bi flux roughens the surface, possibly by the formation of Bi droplets, which has been observed in studies of Bi incorporation in Ga-based semiconductors [85–87].

Structural characterization was conducted on the successfully grown InAsSb films. Figure 5.1 shows (004) X-ray Diffraction (XRD) reciprocal space maps (RSMs) of series A under various Bi fluxes. The substrate and film peaks are easily discernible in each map. The clearest trend from these maps is that the amount of Sb incorporated decreases with increasing Bi flux, as shown by the increasing film-substrate splitting. The RSMs also indicate differences in the structural quality of the films. The film peak for the film grown without a Bi flux is diffuse and elongated vertically, along the growth direction, suggesting an out of plane lattice distortion, possibly due to variations in composition. This peak is also broadened indicating lateral variation in the lattice parameter possibly due to defect injection and strain relaxation (10 %) arising from the lattice mismatch between the film and substrate. In contrast, the films grown under a Bi flux exhibit diffraction peaks that are narrow and isotropic, suggesting high crystalline quality and uniformity in composition. The sample grown under the highest Bi flux again shows some peak broadening, most likely due to dislocations arising from the increasing lattice mismatch. The relaxation in this sample was 4 %.

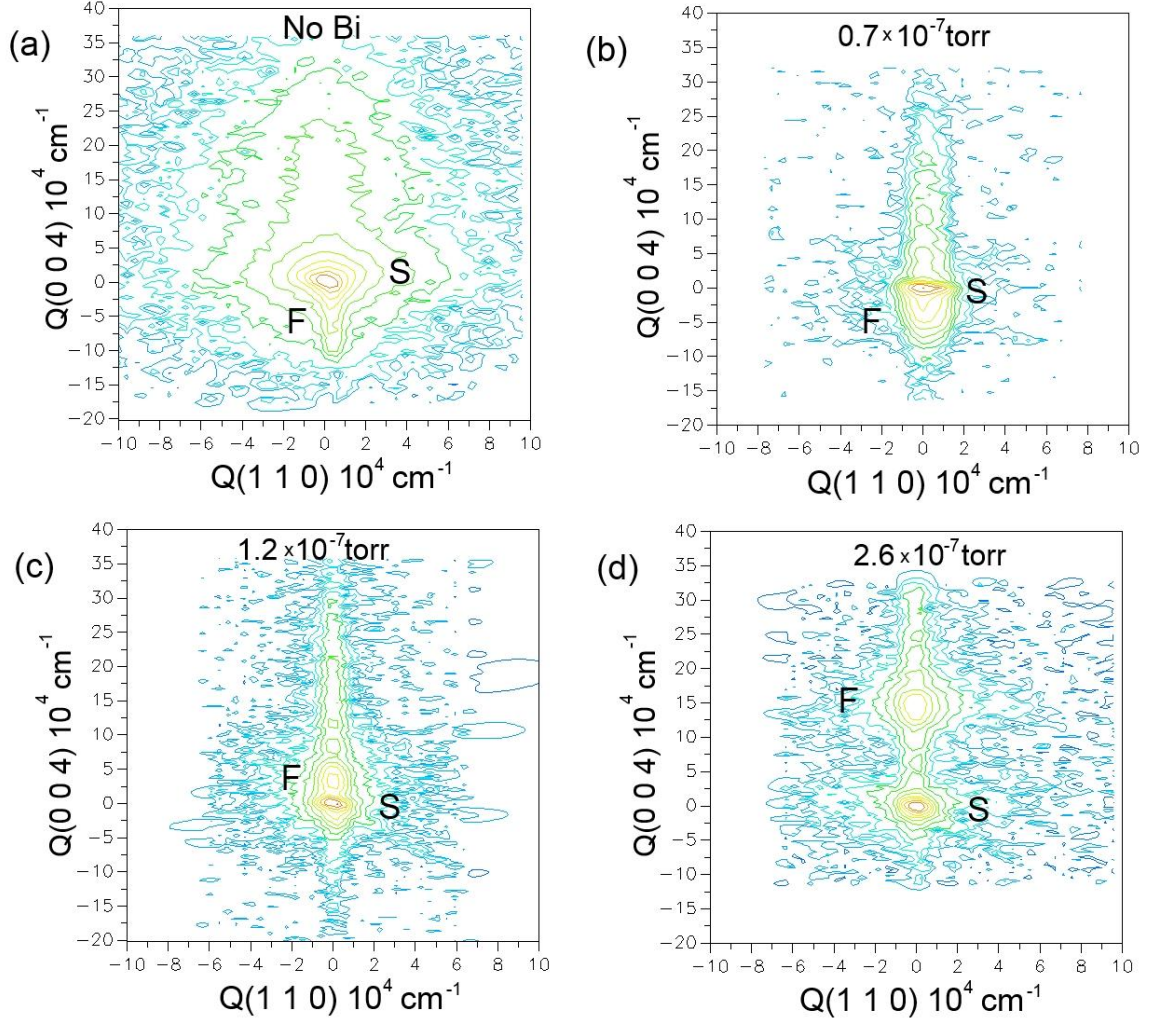


Figure 5.1. (004) Reciprocal space maps of series A films with Bi fluxes noted. S denotes the GaSb substrate and F denotes the InAsSb film.

Aside from the RSMs, XRD was used to determine the amount of Sb incorporated into each film. Figure 5.2 shows plots of the Sb composition determined from the XRD measurements as a function of Bi BEP for the two series. Given that Bi is known to readily desorb at these temperatures [88], it was assumed that no Bi was incorporated into the films when calculating the compositions. It is clear that increased Bi flux decreases the amount of Sb incorporation for otherwise constant growth conditions. The influence of Bi on the composition appears to be stronger for series A (low T) than series B (high T), which may be due to the difference in growth temperatures. However, there might also be a difference in the absolute Bi fluxes between the two

sample series, as ion gauge sensitivity factors are known to vary depending on the gauge geometry and history [89].

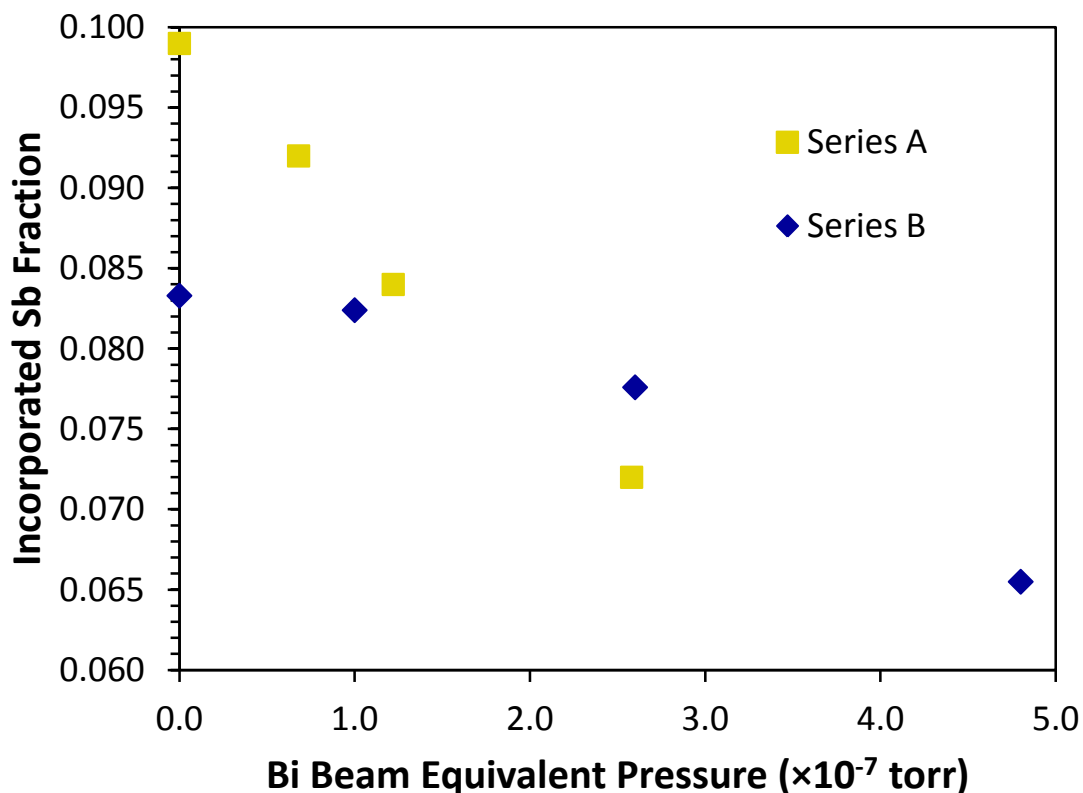


Figure 5.2. Plots of InAsSb film composition vs Bi flux for series A and series B. While these data are plotted together, the Bi BEPs were measured in different chambers and might vary slightly with respect to each other.

Rutherford backscattering spectrometry (RBS) experiments were performed to confirm the assumption that no Bi had incorporated into the films. Figure 5.3 shows the RBS spectra for series A along with the simulated curve and the elemental components for the sample grown without Bi. The vertical dotted line denotes the channel at which the Bi signal would be observed. The RBS data confirms that there is no Bi in the films greater than the detection limit of this RBS system, which is approximately 0.5 atomic % as determined from the average height of the noise near the channel at which a Bi signal would be observed. The RBS spectra for these films show the plateaus that would be expected for homogeneous films, whose positions are consistent with the

compositions determined by XRD. The peaks and valleys in the RBS for the films grown with Bi arise due to the superposition of the signals from each element in the layers, assuming abrupt interfaces. This is consistent with the XRD data of these films, which exhibit Pendellosung fringes (Figure 5.1b-d). The RBS data from the film grown without Bi lacks these distinct peaks, suggesting a rough interface between the InAsSb film and the GaSb substrate. This observation is also consistent with the lattice-mismatch induced broadening observed in the XRD for this film (Figure 5.1a). The RBS spectra of series B had no evidence of Bi incorporation either.

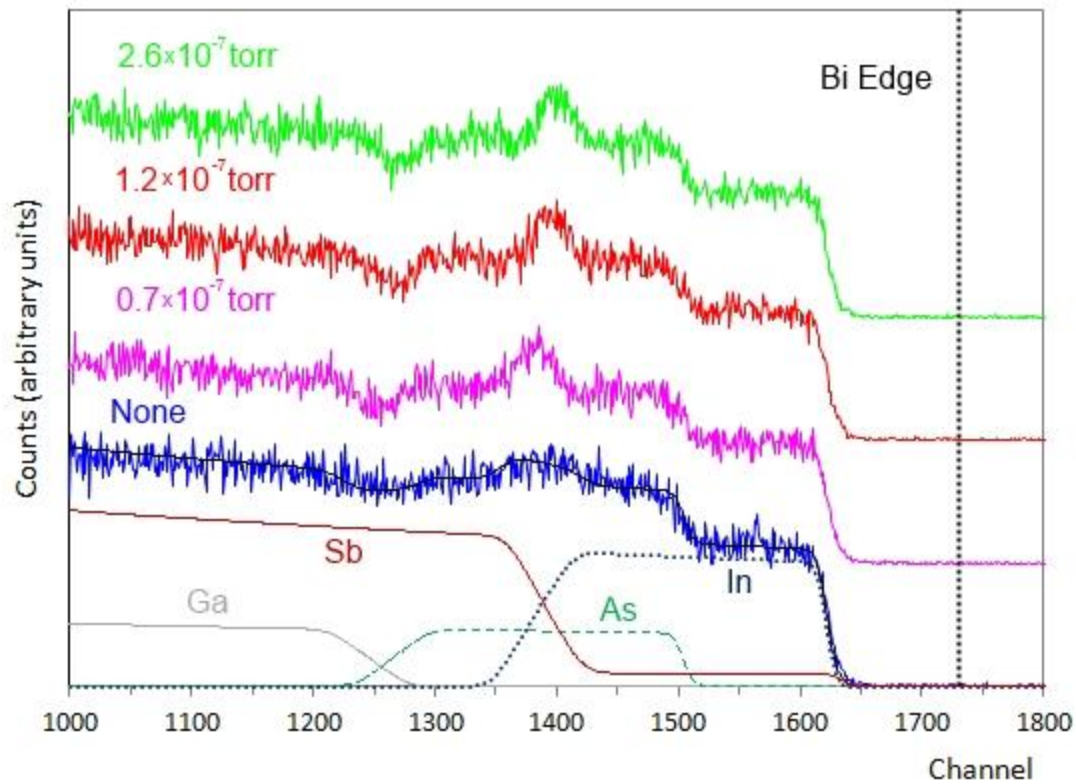


Figure 5.3. Plots of RBS spectra of series A as a function of Bi BEP. The simulated curve and its elemental components are included for the samples grown without Bi. The channel at which Bi would be observed is marked by a dotted line.

5.3.2 Model for Bi-Catalyzed Formation of InAs Formation

A kinetic model of anion incorporation is employed qualitatively here to gain a deeper understanding of how using Bi as surfactant is decreasing the Sb composition of the InAsSb films.

There are several kinetic models for mixed anion alloy growth [82,90–92], each of which takes the various physical processes that take place into account. These processes are illustrated in Figure 5.4. For instance, the incident flux is the primary term that determines the net growth flux, but this contribution is influenced by the presence of desorption and surface segregation. Another process known to occur in mixed anion systems is the removal of one anion species in place of another [17]. For instance, it is well known that As preferentially displaces Sb in both GaAsSb [17] and InAsSb [15,16,82]. Each of these rates is Arrhenius in nature and take the standard form:

$$P = \frac{(N\nu)^2}{F_{In}} \exp \left[-\frac{2E_j}{kT} \right] \quad (5.1)$$

where N is the density of atomic surface sites, ν is the attempt frequency, E_j is the activation energy of the j th process, k is Boltzmann's constant, and T is the temperature. F_{In} is the impinging In flux, which acts to limit the process.

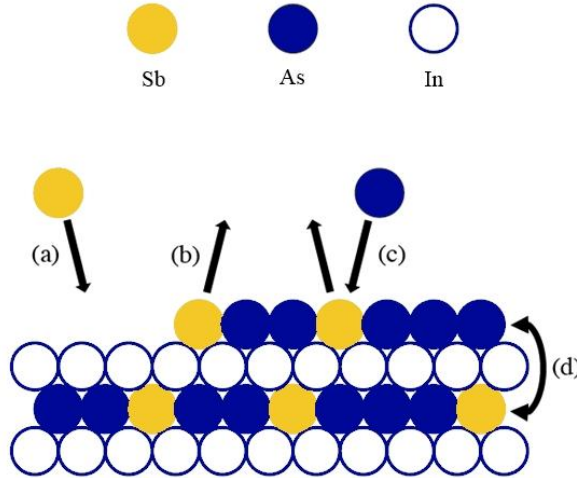


Figure 5.4. Schematic of growth processes at the surface of InAsSb [82]. a. Deposition. b. Desorption. c. Removal of Sb by As. d. Sb segregating to the surface by swapping places with As.

To date, these models have only taken binary alloys into account, but it is straightforward to add a third anion atom to the model. The growth flux for Bi is as follows:

$$J_{Bi} = F_{Bi} - \theta_{Bi} P_{Bi}^{des} - \theta_{Bi} P_{Bi \rightarrow As}^{rem} - \theta_{Bi} P_{Bi \rightarrow Sb}^{rem} + y_b \theta_{As} P_{As \rightarrow Bi}^{seg} + y_b \theta_{Sb} P_{Sb \rightarrow Bi}^{seg} \quad (5.2)$$

The first term on the right hand side represents the amount of impinging Bi, F_{Bi} . The second term represents the reduction in the net flux due to desorption, which is the product of the rate of desorption and the surface coverage of Bi, θ_{Bi} . The third and fourth terms decrease the net flux of Bi via removal of Bi from the surface by As or Sb, and depend on the product of the coverage of Bi and the rate of removal. The fifth and sixth terms increase the net flux of Bi due to surface segregation, the exchange of subsurface Bi and As or Sb on the surface. These terms are the product of the composition of Bi in the subsurface layer (assumed to be the same as that of the bulk) y_b , the surface coverage of As or Sb, and the rate of segregation. y_b , is proportional to the surface coverage of Bi via the equilibrium partition coefficient K , and can range from 0 (for a pure surfactant) to 1 (for complete incorporation) [93]. Similar equations can be written for the growth flux of Sb and As:

$$J_{Sb} = F_{Sb} - \theta_{Sb}P_{Sb}^{des} - \theta_{Sb}P_{Sb \rightarrow As}^{rem} + \theta_{Bi}P_{Bi \rightarrow Sb}^{rem} + x_b\theta_{As}P_{As \rightarrow Sb}^{seg} - y_b\theta_{Sb}P_{Sb \rightarrow Bi}^{seg} \quad (5.3)$$

$$J_{As} = F_{As} - \theta_{As}P_{As}^{des} + \theta_{Sb}P_{Sb \rightarrow As}^{rem} + \theta_{Bi}P_{Bi \rightarrow As}^{rem} - x_b\theta_{As}P_{As \rightarrow Sb}^{seg} - y_b\theta_{As}P_{As \rightarrow Bi}^{seg} \quad (5.4)$$

The concentration of each anion is thus the ratio of the net flux of that anion and the sum of the net anion fluxes.

The experimental results in Section 5.3.1 show that some of the processes that were identified in Equations 5.2 through 5.4 can be eliminated. For instance, the RBS data show that for both series, no Bi was incorporated into any of the InAsSb films. Thus y_b and J_{Bi} are zero. As a result, the impinging flux of Bi is equal to the sum of the desorption and removal fluxes such that:

$$F_{Bi} - \theta_{Bi}P_{Bi}^{des} = \theta_{Bi}P_{Bi \rightarrow As}^{rem} + \theta_{Bi}P_{Bi \rightarrow Sb}^{rem} \quad (5.5)$$

Given that both J_{Sb} and J_{As} depend on the removal of Bi by that anion, Equation 5.5 $F_{Bi} - \theta_{Bi}P_{Bi}^{des} = \theta_{Bi}P_{Bi \rightarrow As}^{rem} + \theta_{Bi}P_{Bi \rightarrow Sb}^{rem}$ (5.5 may substitute for the fourth terms in Equations 5.3 and 5.4. The concentration of Sb is the net Sb flux divided by the sum of all of the net anion fluxes.

Since the only growth parameter that was varied in each series is the flux of Bi, it is reasonable to

assume that the desorption, removal, and segregation terms in each net flux equation are constant. If in this case Bi removal by Sb is much faster than or equal to Bi removal by As, the Sb concentration will increase with increasing Bi Flux, as in the following proportionality:

$$x_b \propto \frac{K_{Sb} + F_{Bi}}{K_{Sb} + K_{As} + F_{Bi}} \quad (5.6)$$

Where K_i is a constant encompassing all of the terms for species i . If instead Bi removal by As is faster than the removal of Bi by Sb, then the Sb concentration will decrease with increasing Bi flux, as in the following:

$$x_b \propto \frac{K_{Sb}}{K_{Sb} + K_{As} + F_{Bi}} \quad (5.7)$$

The experimental results show that Sb incorporation decreases with increasing Bi flux, therefore it is more likely that Bi is more quickly removed from the surface by As than by Sb.

These experiments and analysis of the incorporation model show that surface Bi acts as a catalyst for As incorporation. This is not surprising considering that the In-As bond is stronger than the In-Sb or (calculated) In-Bi bonds [69]. This catalytic model is consistent with the results for GaNAs, which showed enhanced N incorporation in the presence of Bi [29]. In that case, the Ga-N bond is stronger than the Ga-As or (calculated) Ga-Bi bonds [69], resulting in faster removal of Bi by N than by As. These results together demonstrate the importance of the surfactant in changing the chemistry of the surface, rather than acting as a steric barrier to incorporation. Furthermore, the nx3 RHEED patterns observed during growth of InAsSb in the presence of Bi at the surface might contribute to the chemical changes at the surface. The results of Chapters 3 and 4 indicated that Sb tends to preferentially occupy the dimers sites of 4x3 and 2x6 reconstructions of InAs and InSb, while Bi has been predicted to behave similarly on GaAs [55], Bi GaSb [39], and on InSb [34]. Thus on InAsSb, Bi might occupy the dimer sites that would otherwise be preferred by Sb, without

blocking subsurface Sb. In this way, some Sb still incorporates, but the excess Sb that would have occupied dimer sites might instead be replaced by Bi which is in turn replaced by As.

5.4 Conclusions

Experimental evidence shows that the presence of Bi as a surfactant inhibits Sb incorporation in InAsSb alloys for a range of growth conditions without itself incorporating. A proposed kinetic model suggests that surface Bi atoms increase the reactivity of As on the surface. Further study is required to systematically quantify all the mechanisms involved, but this model can be used to determine the composition function of Bi flux, and be extended to describe other mixed anion or mixed/cation systems such as GaAsN or AlInAsSb.

CHAPTER 6

Conclusions and Future Work

The work presented in this dissertation discovered the atomic scale, thermodynamic driving force for the interaction between As and Sb and how this is modified by the presence of a surfactant. This expands current knowledge of the interaction between As and Sb on semiconductor surfaces as a foundation for future work to manipulate this interaction and improve crystal growth of InAsSb and III-As/III-Sb heterostructures. Because these materials are intended for optoelectronic devices, precise compositional control, elimination of defects, and compositionally abrupt interfaces are critical for device performance. However, past work on this materials system has not examined the details of the surface during growth. Thus, the emphasis of this work was to first understand the atomic scale details of the InAsSb system before modifying Sb-As interaction by applying an additional element to the surface in order to guide future investigations correlating the growth surface to materials properties and performance. Due to the complexity of investigation of alloys at the atomic scale, this body of research was necessarily divided into smaller, more tractable studies. To that end, three facets of this larger goal were explored in the preceding chapters using a combination of *ab initio* calculations and experiments. First in CHAPTER 3, the influence of Sb on the surface of InAs was studied, showing that Sb interacts more strongly with the surface than previously thought. Next in CHAPTER 4, the opposite compositional end of the InAsSb system was investigated: the influence of As on the surface of InSb, providing further evidence for the strong intermixing between As and Sb. Finally in

CHAPTER 5, the interaction between Sb and As is modified through the use of Bi as a surfactant, indicating that Bi weakens the interaction between Sb and the crystal through catalyzing the formation of InAs.

6.1 Key Findings

The results of the investigation of the atomic-scale interaction between Sb and As on InAs surfaces yielded several key findings (CHAPTER 3). RHEED experiments indicated that a static, and initially As-terminated, InAs surface exposed to Sb and As₂ fluxes tends to exhibit either an nx3 or c(4x4) RHEED pattern under most fluxes. Density functional theory (DFT) calculations confirm these highly anion-rich reconstructions. The DFT calculations also provide evidence of a thermodynamic driving force for Sb-As intermixing. Several configurations of the β (4x3) and c(4x4) reconstructions are stabilized by subsurface Sb and many other configurations contain Sb-As heterodimers. Additionally, the *ab initio* calculations predict that much of the phase diagram consists of stoichiometric or nearly stoichiometric 2x4 reconstructions ranging from completely As-terminated to Sb-terminated. This is confirmed through STM of an initially In-terminated surface that is exposed to Sb, suggesting that a 2x4 was not observed during the static surface experiments due to a kinetic limitation to replacing As at the surface. These experiments and the DFT phase diagram indicate that InAsSb of any composition could be grown under reconstructions ranging from having bulk-like stoichiometry to being highly anion-rich. Finally, STM shows that Sb roughens the surface of InAs through a cooperative mechanism of creating 2D islands and vacancy clusters (divots) in order to transform the 2x4 terrace to c(4x4) reconstructions. This is in contrast to the past suggestion that Sb only weakly interacts with the InAs surface.

Several conclusions were drawn from the investigation of the InSb surface and the interaction between Sb and As on InSb (CHAPTER 4). First, DFT and MC simulations of the InSb

(001) surface indicate that the surface reconstruction phase diagram includes 2×4 and $c(4\times 4)$ reconstructions. This provides a more complete computational phase diagram that agrees better with experimental results than a previous report. STM imaging of a surface exhibiting an $A-(1\times 3)$ RHEED pattern indicates that this pattern is the result of coexistence between 4×3 or $c(2\times 6)$ and $c(4\times 4)$ reconstructions, which are close in surface energy according to the MC calculations. Next, DFT calculations of the surface reconstructions stabilized by As on InSb indicate that As and Sb intermix through As infiltrating the subsurface layer of the InSb crystal to form configurations of the $\alpha(4\times 3)$ reconstruction. This reconstruction is confirmed with RHEED experiments that show that the $nx3$ pattern is stable under a variety of substrate temperatures, As_2 , and Sb fluxes. These experiments also provide further evidence that the $A-(1\times 3)$ pattern is the result of coexistence between $c(4\times 4)$ and 4×3 reconstructions. At elevated temperature, the 4×3 is not accessible, but the spacing between intermediate streaks of the $A-(1\times 3)$ approaches the even spacing of an $nx3$ pattern with increasing As_2 flux. RHEED also indicates that As_2 roughens the surface through the formation of facets under Sb-poor conditions. All of these changes in the RHEED patterns are reversible under a sufficiently high Sb flux, which is evidence of Sb-for-As exchange under Sb-rich conditions.

Finally, the influence of Bi as a surfactant on the interaction between Sb and As was investigated in CHAPTER 5. The use of Bi resulted in $nx3$ RHEED patterns, which is consistent with reports of Bi-stabilized 4×3 reconstructions on GaAs [55], on GaSb [39], and on InSb [34]. Experimental evidence shows that the presence of Bi as a surfactant inhibits Sb incorporation in InAsSb alloys for a range of growth conditions without itself incorporating. A proposed kinetic model suggests that surface Bi atoms increase the reactivity of As on the surface. Further study is required to systematically quantify all the mechanisms involved and identify the role of Bi-terminated surface reconstructions.

6.2 Prospects for Future Research

It is clear that significant progress has been made contributing to understanding the atomic scale interaction between As and Sb and the modification of that interaction by Bi. The conclusions discussed in Section 6.1 above suggest directions for future research both in gaining further knowledge of the Sb-As interaction and applying this knowledge to improve the properties and performance of InAsSb and III-As/III-Sb devices. One direction for research is to use the Sb:InAs and As:InSb phase diagrams as guides for growing films under varying stoichiometry to determine if there are connections between surface reconstructs and point defect incorporation and interfacial broadening. Since Bi was shown to decrease Sb incorporation, Bi as a surfactant might be an additional means to control material quality and decrease interfacial broadening. Additional open questions remain regarding the use of Bi as a surfactant and its influence on the interaction between Sb and As, specifically regarding the atomic scale details.

The varied stoichiometry of the 0K DFT phase diagrams of both the Sb:InAs (CHAPTER 3) and As:InSb (CHAPTER 4) opens the door for investigations into the influence of growth surface reconstruction on material and device quality for InAsSb and III-As/III-Sb heterostructures. Both phase diagrams consist of alloyed 2x4 reconstructions, suggesting that the entire compositional range of InAsSb could be grown under a stoichiometric or nearly stoichiometric surface. However, this must be validated as alloy growth is inherently different from depositing small amounts of material onto a pure binary substrate. For example, macroscopic strain is known to impact the stability of reconstructions [94,95]. Additionally, the distribution of solute atoms would cause local variations in strain and chemical potential at the atomic scale, which could influence which reconstructions appear and could lead to coexistence between surface phases.

Investigations into the influence of growth surface reconstruction on material properties and the validation of the calculated phase diagrams can be conducted concurrently. Typically, InAsSb is grown under an $nx3$ RHEED pattern [2,63,64] and is often unintentionally background n-type doped [10,63,71–73]. This $nx3$ pattern is consistent with a $4x3$ reconstruction [67]. The $4x3$ contains a double layer of anions, which can be thought of as a layer of antisites, group-V atoms on group-III sites. It is possible that during growth, some proportion of these atoms are trapped in the crystal and become n-type point defects. Thus, growth under a more stoichiometric $2x4$ surface might prevent these defects. The elimination of such defects would be beneficial for device performance, which is sensitive to the concentration of electronically active defects. Additional experiments could be conducted comparing the $c(4x4)$ and $4x3$ reconstructions to determine if one type of reconstruction is more prone to the incorporation of defects than the other.

While the atomic details of As on InSb surfaces were well characterized computationally, there remain open experimental questions about this system. One question involves the As-terminated configurations of the $\beta 2(2x4)$ reconstruction on InSb, which were predicted by DFT calculations but not observed experimentally. It is possible that the formation of this reconstruction competes with the process of As-induced faceting. Similarly to the formation of the Sb-terminated $\alpha 2(2x4)$ on InAs, first depositing In might allow a different reaction pathway by providing a barrier between the As and Sb-containing layers. This might allow the As-terminated $\beta 2(2x4)$ to be confirmed experimentally using STM. Another question relates to the atomistic mechanism behind As-induced surface roughening. While Sb was observed to roughen InAs by forming 2D islands and divots, As was observed to roughen InSb by forming facets. This leaves two distinct avenues of research for surface roughening in the As:InSb system. On one hand, submonolayer deposition of As on InSb might reveal a similar island-divot creation mechanism to Sb:InAs, though possibly with

a 4×3 reconstruction, which is dominant for the As:InSb phase diagram, rather than a $c(4\times 4)$ driving the reaction. On the other hand, submonolayer deposition of As on InSb might provide insight into the nucleation of faceted features, such as which reconstructions form before faceting. Studying the nucleation of facets might also lead to optimizing this process to create faceted quantum dots.

Surface roughening was observed experimentally for both InSb exposed to As and InAs exposed to Sb. While such surface roughening might appear to be inevitable for heterostructure growth, the present work suggests two possible ways to avoid it and the associated interfacial broadening. First, as shown in Figure 3.6, depositing In on the surface before depositing Sb leads to an $\alpha 2(2\times 4)$ reconstruction, rather than the $c(4\times 4)$ reconstructions that drove the island and divot formation (Figure 3.8). This could circumvent the roughening mechanism by separating the arsenide layer from the antimonide layer. Second, lower temperature growth might prevent surface roughening. As shown in Figure 3.7, Sb-induced roughening was only observed at 425°C and not 405°C . This suggests that at lower temperatures, the reaction to pull atoms out of the surface proceeds more slowly.

Related to surface roughening is the phenomenon of interfacial broadening in semiconductor heterostructures, which is a current problem in crystal growth. The results of this dissertation suggest a few methods to pursue as an alternative to the As “pre-soaking” method [14] in order to prevent this broadening. Because surface roughening has been shown in CHAPTER 3 to be the mechanism for interfacial broadening in III-As/III-Sb heterostructures, first depositing the group-III species and/or growing at low temperature, the methods discussed in the previous paragraph, might prevent this broadening. Additionally, it has been suggested that the excess Sb atoms present in double anion layer reconstructions, such as 4×3 or $c(4\times 4)$, contribute to the interfacial broadening in arsenide/antimonide heterostructures [27]. Thus, maintaining a

sufficiently low V/III ratio during growth to maintain a 2×4 reconstruction might prevent broadening. Finally, using Bi as a surfactant might prevent the unintentional incorporation of Sb into the arsenide layers of heterostructures. Such an effect has been reported in the literature previously; the use of a Bi surfactant has been observed to inhibit In segregation and decrease interfacial roughness in InGaAs/GaAs, thus creating a more abrupt interface [31]. This suggests that the In in that case was prevented from incorporating, similarly to how in CHAPTER 5, Bi was found to reduce Sb incorporation by catalyzing the formation of InAs. Thus, Bi might block Sb incorporation and result in abrupt interfaces between arsenide and antimonide layers.

The results of the Bi surfactant study discussed in CHAPTER 5 raise questions about the atomic details of how Bi prevents Sb incorporation through catalyzing InAs. An atomistic understanding of the interaction between Bi and InAsSb surfaces would inform investigations into the influence of Bi-terminated surface reconstructions on material properties and device performance. While the Bi surfactant samples all exhibited an $n\times 3$ RHEED pattern, it is not clear which 4×3 reconstruction this is specifically, or if other structural prototypes are available for this system. The first step for this would involve generating DFT phase diagrams of Bi:InAs and Bi:InSb. While an *ab initio* surface reconstruction phase diagram of Bi on InSb has been previously reported [34], the new calculations of stable configurations of 2×4 and $c(4\times 4)$ reconstructions discussed in CHAPTER 4 suggest that the previous phase diagram might be incomplete. However, this might proceed more quickly by using the results of the Sb:InAs and As:InSb phase diagrams as starting points. Since Bi is a larger atom than either As or Sb, it might occupy surface sites similarly to how Sb occupies sites on InAs. For example, the $c(4\times 4)$ configurations that contain In, As, and Sb in dimer sites tend to form In-As heterodimers instead of In-Sb heterodimers and would likely form instead of In-Bi heterodimers. An additional lesson from the Sb:InAs and As:InSb phase diagrams might be applied to calculations involving Bi, such as not considering supercells of the

$c(4\times 4)$ or 2×4 reconstructions. For these reconstructions, most of the supercell configurations were merely combinations of primitive surface cells that were predicted to be stable on their own. Thus, the computational expense associated with these large cells might be avoidable. Additional computational savings could be achieved by excluding In substitution from the 4×3 reconstructions. This is supported by the fact that allowing In substitution on the $h0(4\times 3)$ structural prototype in this dissertation did not result in any In-containing configurations, aside from the well known $\alpha(4\times 3)$ and $\beta(4\times 3)$ structures with varying As and Sb concentrations. Completion of *ab initio* phase diagrams of Bi-containing reconstructions would then provide a guide for experimental investigation of Bi on InAs and InSb. This includes STM and RHEED studies of Bi-exposed surfaces, as were conducted for Sb:InAs and As:InSb in this dissertation.

APPENDIX A

Selected MATLAB Script for Finite Temperature Surface Energy Calculations

```
% This script calculates surface energies and creates phase diagrams
%for InSb Monte Carlo simulations run using CASM with output as
%temperature runs when controlling T and Sb chemical potential (mu_Sb).
%It can be easily modified for other systems and chemical potential
%runs.

% Note: this script is designed to be used for MC runs that were
%conducted using a cluster expansion for which the energies in the
%reference file were set to zero.

% VASP reference energies
Ebulk=-8.300153; % DFT energy of bulk InSb per compound unit
EH=-5.0972293; % DFT energy of pseudohydrogen bonded to the bottom Sb
layer
EAs=-10.810267/2; % DFT energy of As atom from bulk As
EIn=-6.5359127/2; % DFT energy of In atom from bulk In
ESb=-9.6469348/2; % DFT energy of Sb atom from bulk Sb

kB=8.617e-5; % Boltzmann Constant

% matlabtemp_list lists the temperature data files to be opened
% the matlabtemp.* files must be modified to remove the header and
%extra spaces on the first line of data. The following bash script
%will work:
%{
#!/bin/bash

for file in $(ls temp.*)
do
tail -n +3 $file > tmp$file
sed '1s/ //' < tmp$file > matlab$file
rm tmp$file
done
%}

%Note: matlabtemp_list should be organized with chemical potentials in
%ascending or descending order. Make sure that the direction of the
%thermodynamic integration later in this script is consistent with this
order.
matlabtemp_list=textread('matlabtemp_list','%s'); %#ok<DTXTRD>

%load the data from matlabtemp files and organize into a 3D array,
%rather than creating separate variables. T ranges from 100 to 800 K
```

```

%in 100 K increments (8 temperatures) L= number of chemical potential
%data points
NT=8;
L=length(matlabtemp_list);
Tdata=zeros (NT,4,L);

for n=1:L
    matlabtemp=load(matlabtemp_list{n});
    %extract chemical potential from filename as a floating point,
    %matlab first creates a cell
    %array, so the next line's syntax reads the value of the cell (a
    %floating point)
    mucell=textscan(matlabtemp_list{n},'%*[matlabtemp.]%f');
    mu=mucell{1}*1e-3; %convert eV
    %for T matrices row#: 1=mu_SbSomething, 2=AVconc, 3=AVenergy,
    %4=surface energy
    Tdata(:,1,n)=mu;
    Tdata(:,2,n)=matlabtemp(:,2);
    Tdata(:,3,n)=matlabtemp(:,3);

end

In_slab=60; % # bulk-like In in unit cell
Sb_slab=68; % # bulk-like Sb in unit cell
N_sites=12; % #atomic sites allowed to vary
n_1x1=12; % #1x1 area cells
A_1x1=4.54691585097727^2; %Angstroms squared: area of 1x1 cell
NIn=zeros (NT,L);
NSb=zeros (NT,L);

%determines average number of In and Sb atoms per c(4x4) unit cell
%based on site occupancy. These are not necessarily integers because
%of averaging over the large MC simulation cell.
for n=1:L
    NSb(:,n)=Tdata(:,2,n)*N_sites+Sb_slab;
    NIn(:,n)=(1-Tdata(:,2,n))*N_sites+In_slab;
end
x_Sb=(NSb-NIn-n_1x1/2)/n_1x1/A_1x1;

Phi=zeros (NT,L);
Phi_tot1=zeros (NT,L);
Phi_tot0=zeros (NT,L);
Sum=0;
Ndmu=0;

%{
Thermodynamic (numerical) integration
Phi00 or Phi01 is the reference free energy for a surface either
completely In or completely Sb terminated.
This simulation was run with mu_Sb increasing until a completely Sb-
terminated surface was obtained. Thus, Phi00 is at the end of the Tdata
and integration goes from high to low muSb.
Phi01 is set up for the opposite case, but commented out here
%}

```



```

%{
Phi01=Tdata(:,3,1);
for n=1:1:L
    if n==1
        Phi_tot1(:,n)=Phi01;
    else
        Ndmu=(N_sites*Tdata(:,2,n)+N_sites*Tdata(:,2,n-1))/2.*(Tdata(:,1,n)-Tdata(:,1,n-1));
        Sum=Sum+Ndmu;
        Phi_tot1(:,n)=Phi01-Sum;
    end
end

Phi_tot=Phi_tot1;
%}

Phi00=Tdata(:,3,L);
for n=L:-1:1
    if n==L
        Phi_tot0(:,n)=Phi00;
    else

Ndmu=(N_sites*Tdata(:,2,n)+N_sites*Tdata(:,2,n+1))/2.*(Tdata(:,1,n)-Tdata(:,1,n+1));
        Sum=Sum+Ndmu;
        Phi_tot0(:,n)=Phi00-Sum;
    end
end

%Phi_tot=Phi_tot1;
Phi_tot=Phi_tot0;

%Convert from Grand Caonical Free Energy to Internal Energy
E_tot=zeros(NT,L);
for n=1:L
    E_tot(:,n)=Phi_tot(:,n)+N_sites*Tdata(:,2,n).*Tdata(:,1,n);
end

% Convert mu from mu_SbSomething that CASM uses to mu_Sb-mu_SbBulk,
%mu_Sb relative to the formation of bulk Sb
Tdata(:,1,:)=(Tdata(:,1,:)-(ESb*2-Ebulk));
% Convert mu from mu_SbDimer to mu_Sb-mu_SbBulk for the 2x4 cells.
% Included for informational purposes
%Tdata(:,1,:)=(Tdata(:,1,:)-2*ESb)/2;

% Calculate formation energy per unit area
E_form=(E_tot-(Ebulk-ESb)*NIn-ESb*NSb-n_1x1*EH)/n_1x1/A_1x1;
for n=1:L
    for m=1:NT
        % Calculate surface energy at all points in T-mu_Sb space
        Tdata(m,4,n)=E_form(m,n)-x_Sb(m,n)*Tdata(m,1,n);
    end
end
end

```

```

% plot surface energy vs mu_Sb at all temperatures
figure(1)
hold on
for n=1:NT
    scatter(Tdata(n,1,:),Tdata(n,4,:))
end

% calculate selected DFT 0K surface energies
mu_DFT=zeros(1,22);
alpha2_gamma=zeros(1,22);
beta2_gamma=zeros(1,22);
zeta_gamma=zeros(1,22);
c4x4_gamma=zeros(1,22);
a3c4x4_gamma=zeros(1,22);
c2x6_gamma=zeros(1,22);
a4c2x6over2_gamma=zeros(1,22);
for m=1:22
    mu_DFT(m)=(m-1)/-100;
    zeta_gamma(m)=0.037768835+0.012092224*mu_DFT(m);
    alpha2_gamma(m)=0.03607883;
    beta2_gamma(m)=0.034502336-0.012092224*mu_DFT(m);
    c4x4_gamma(m)=0.032724568-0.060461119*mu_DFT(m);
    a3c4x4_gamma(m)=0.032817102-0.024184448*mu_DFT(m);
    c2x6_gamma(m)=0.032411995-0.056430378*mu_DFT(m);
    a4c2x6over2_gamma(m)=0.033682939-0.024184448*mu_DFT(m);
end

% plot all MC and selected DFT surface energies vs mu_Sb
figure(2)
hold on

for n=1:NT
    scatter(Tdata(n,1,:),Tdata(n,4,:))
end

plot(mu_DFT,zeta_gamma)
axis([-0.21 0 0.032 0.040])
plot(mu_DFT,alpha2_gamma)
axis([-0.21 0 0.032 0.040])
plot(mu_DFT,beta2_gamma)
axis([-0.21 0 0.032 0.040])
plot(mu_DFT,a3c4x4_gamma)
axis([-0.21 0 0.032 0.040])
plot(mu_DFT,c4x4_gamma)
axis([-0.21 0 0.032 0.040])
plot(mu_DFT,c2x6_gamma)
axis([-0.21 0 0.032 0.040])
plot(mu_DFT,a4c2x6over2_gamma)
axis([-0.21 0 0.032 0.040])

xlabel('\mu_{Sb} (eV)')
ylabel('\gamma (eV/\AA)')

% plot selected DFT energies and MC surface energies at selected
%temperatures and use meV
figure(5)

```

```

hold on
n=1;
m=7;
new_mu=Tdata(:,1,:).*1000; %meV
scatter(new_mu(n,1,:),Tdata(n,4,:).*1000)

scatter(new_mu(m,1,:),Tdata(m,4,:).*1000)
plot(mu_DFT.*1000,zeta_gamma.*1000)

plot(mu_DFT.*1000,alpha2_gamma.*1000)

plot(mu_DFT.*1000,beta2_gamma.*1000)

plot(mu_DFT.*1000,a3c4x4_gamma.*1000)

plot(mu_DFT.*1000,c4x4_gamma.*1000)

plot(mu_DFT.*1000,a4c2x6over2_gamma.*1000)

plot(mu_DFT.*1000,c2x6_gamma.*1000)
axis([-210 0 32 40])
xlabel('\mu_{Sb}-\mu_{Sb bulk} (meV)')
ylabel('\gamma (meV/\AA^2)')

```

APPENDIX B

Schematics of Sb:InAs Surface Reconstructions

Chapter 3 presented the atomic scale details of Sb-terminated InAs surfaces. However, for the sake of brevity, only a selection of the stable surface reconstructions were discussed to discuss the general trends in the data. For completeness, all of the surface reconstructions predicted to be stable using DFT calculations for the Sb:InAs system (Figure 3.4) are presented schematically in this appendix. Because many of the stable phases only occupy small regions of chemical potential space, the full phase diagram is not reproduced here. Instead, subsets of the phase diagram are presented covering limited ranges of chemical potentials to make the areas covered by different reconstructions more readily apparent. Figure B.1, Figure B.2, and Figure B.3 emphasize a region of high μ_{As} and moderate μ_{Sb} , while Figure B.4, Figure B.5, and Figure B.6 detail a wider region of phase space extending to high μ_{Sb} and low μ_{As} . The naming scheme devised for these reconstructions is discussed in Section 3.2.3.

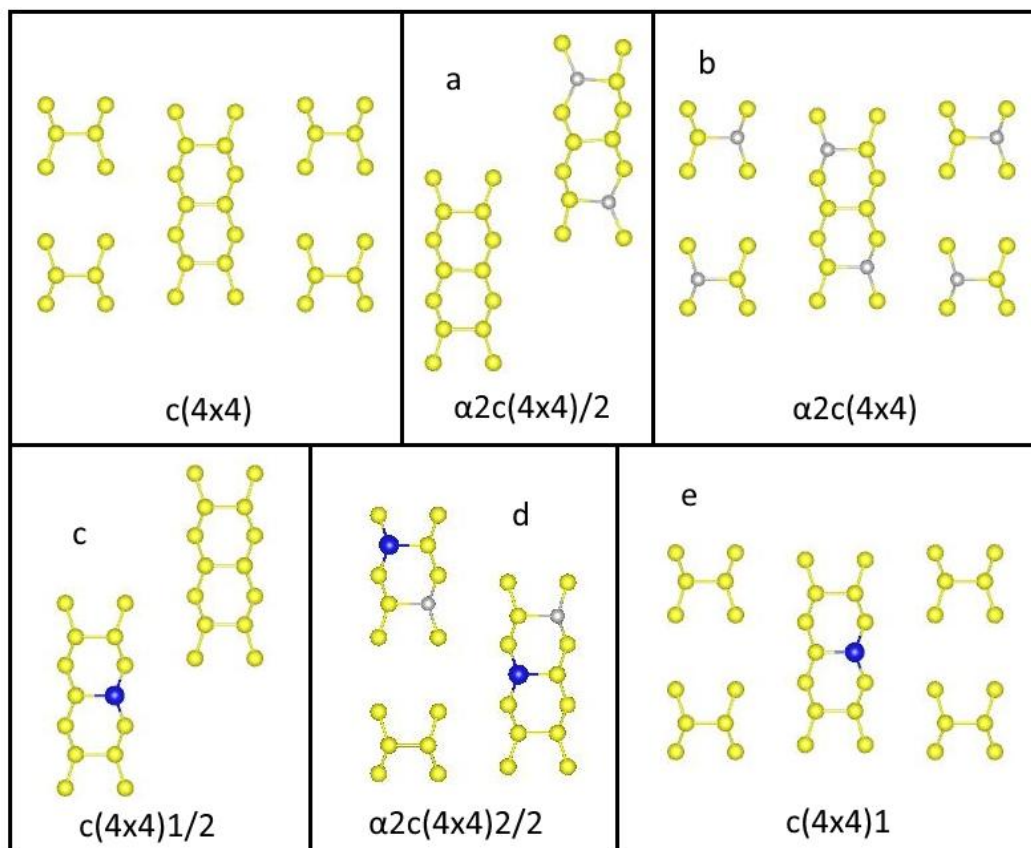
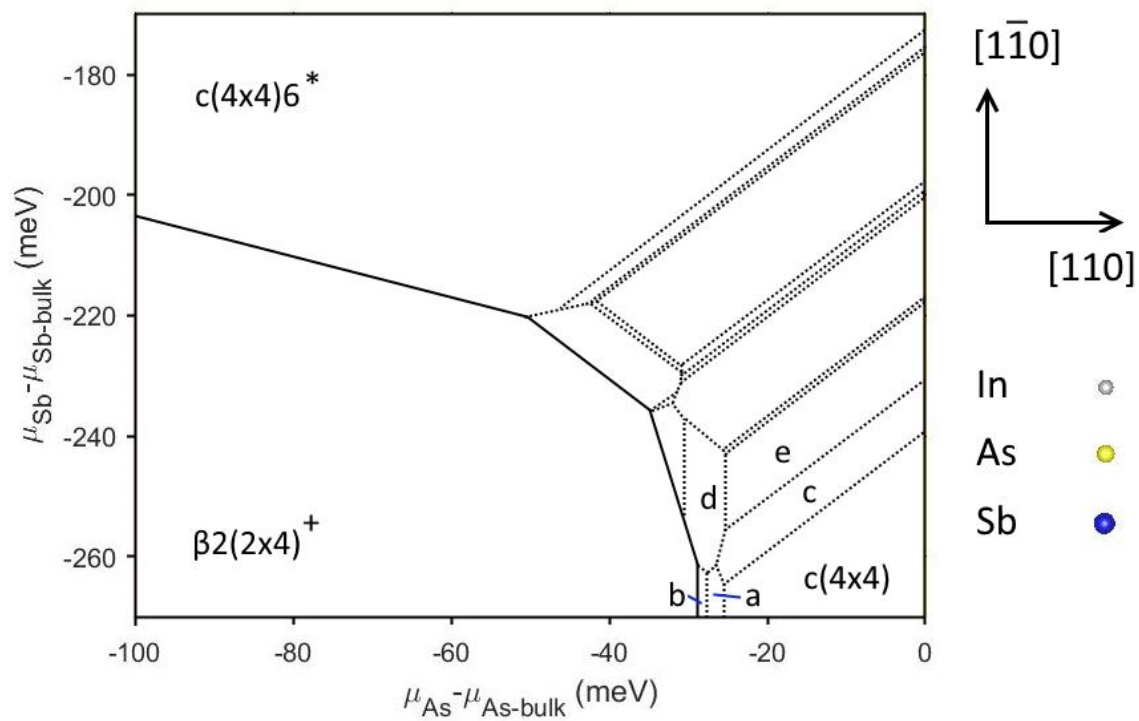


Figure B.1. 0K surface reconstruction phase diagram of Sb:InAs system over a limited chemical potential range and schematics corresponding to the labels on the diagram. *see Figure B.3. +see Figure B.4.

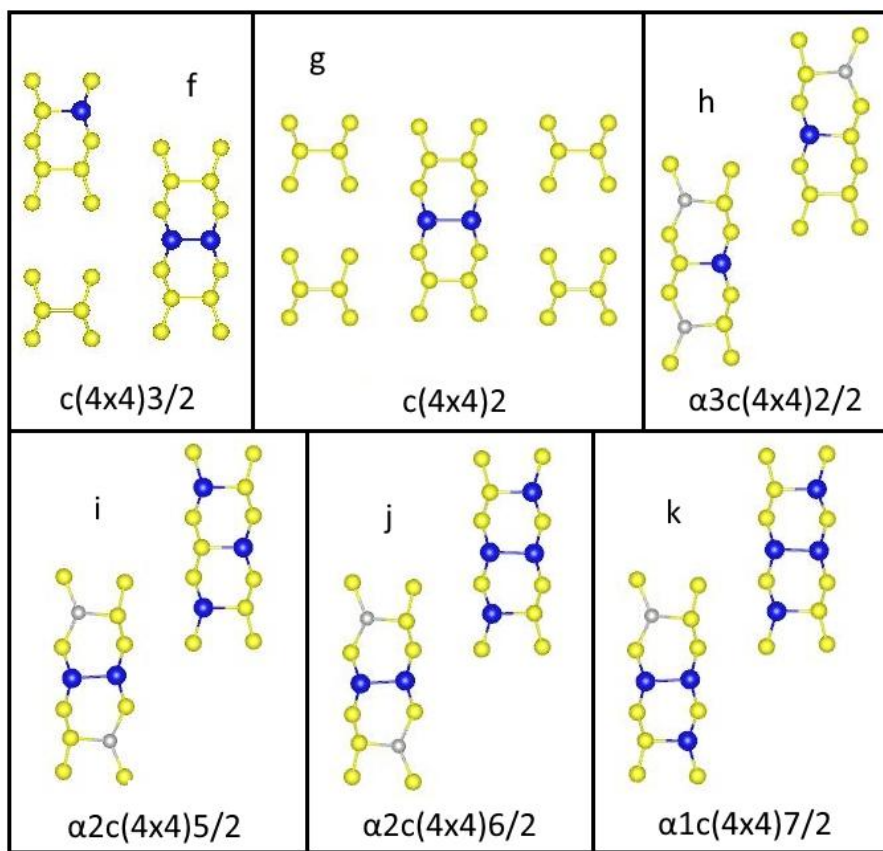
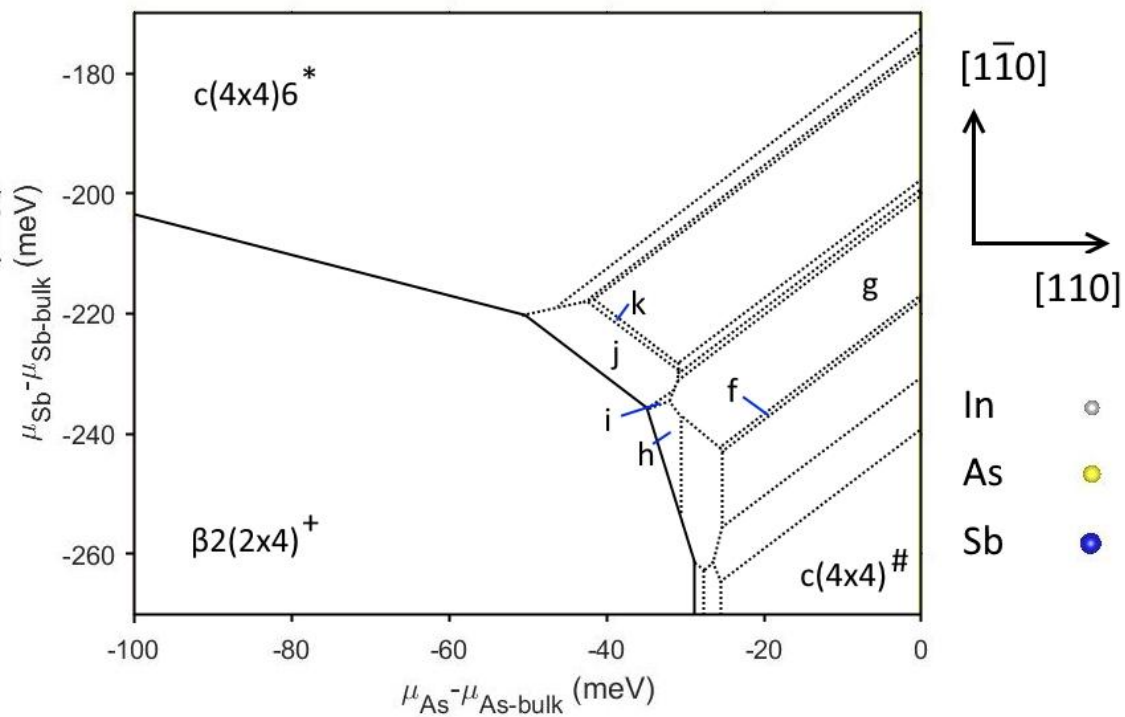


Figure B.2. 0K surface reconstruction phase diagram of Sb:InAs system over a limited chemical potential range and schematics corresponding to the labels on the diagram. *see Figure B.3. + see Figure B.4. # see Figure B.1.

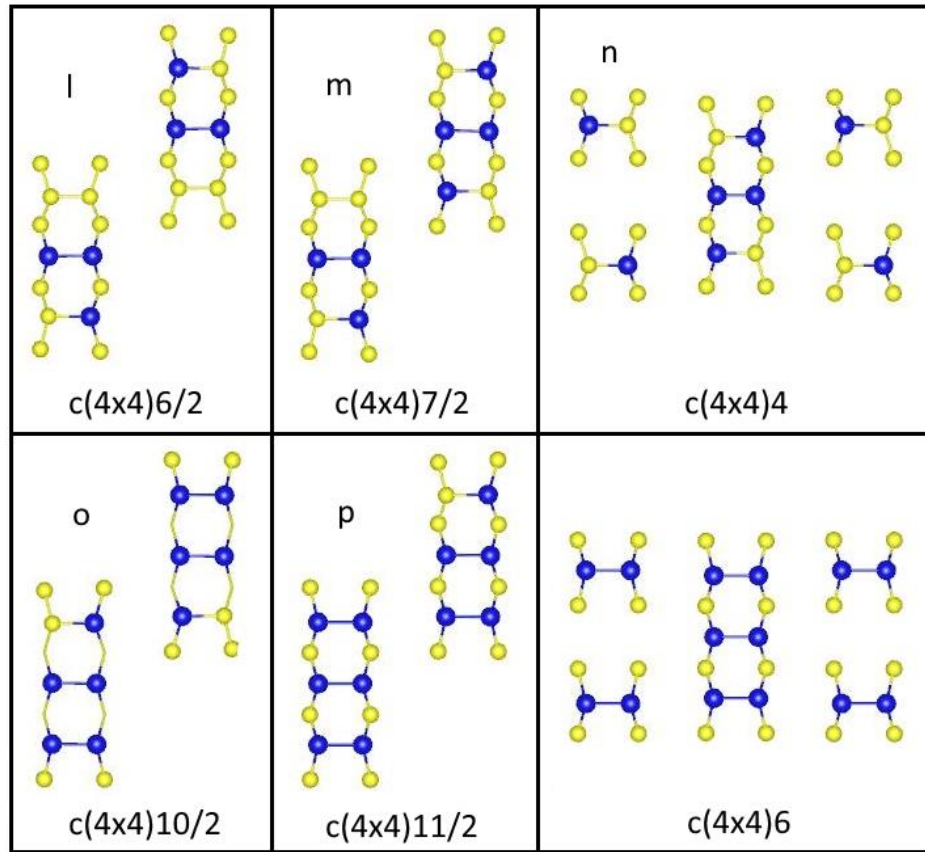
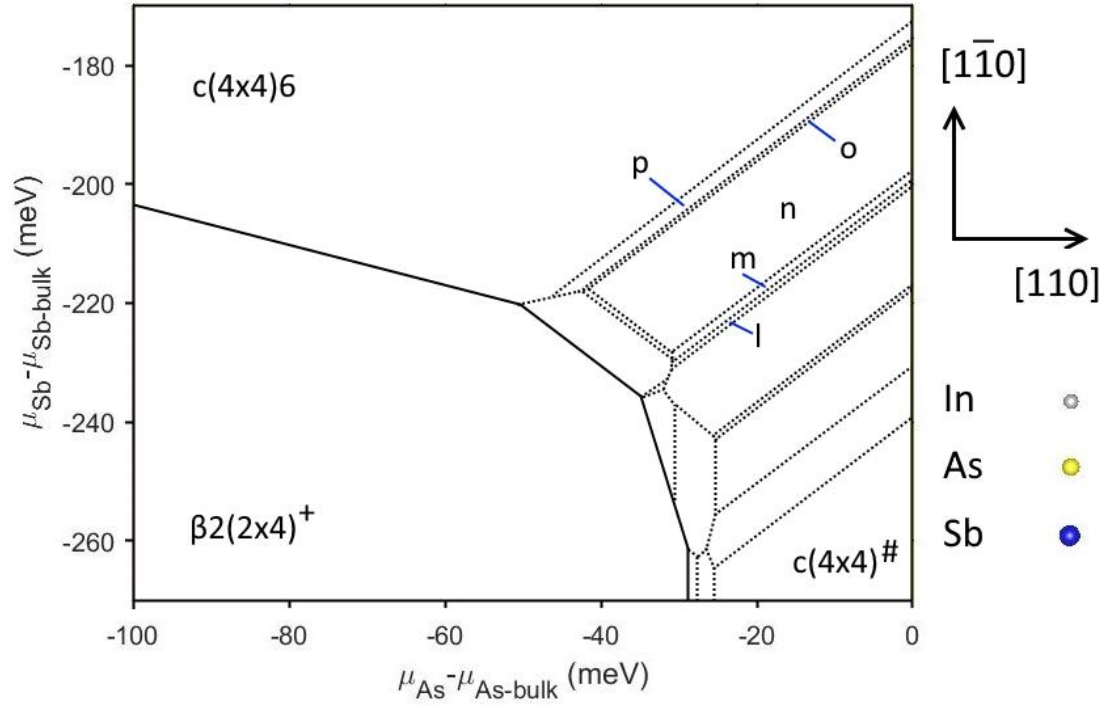


Figure B.3. 0K surface reconstruction phase diagram of Sb:InAs system over a limited chemical potential range and schematics corresponding to the labels on the diagram. +see Figure B.4. # see Figure B.1.

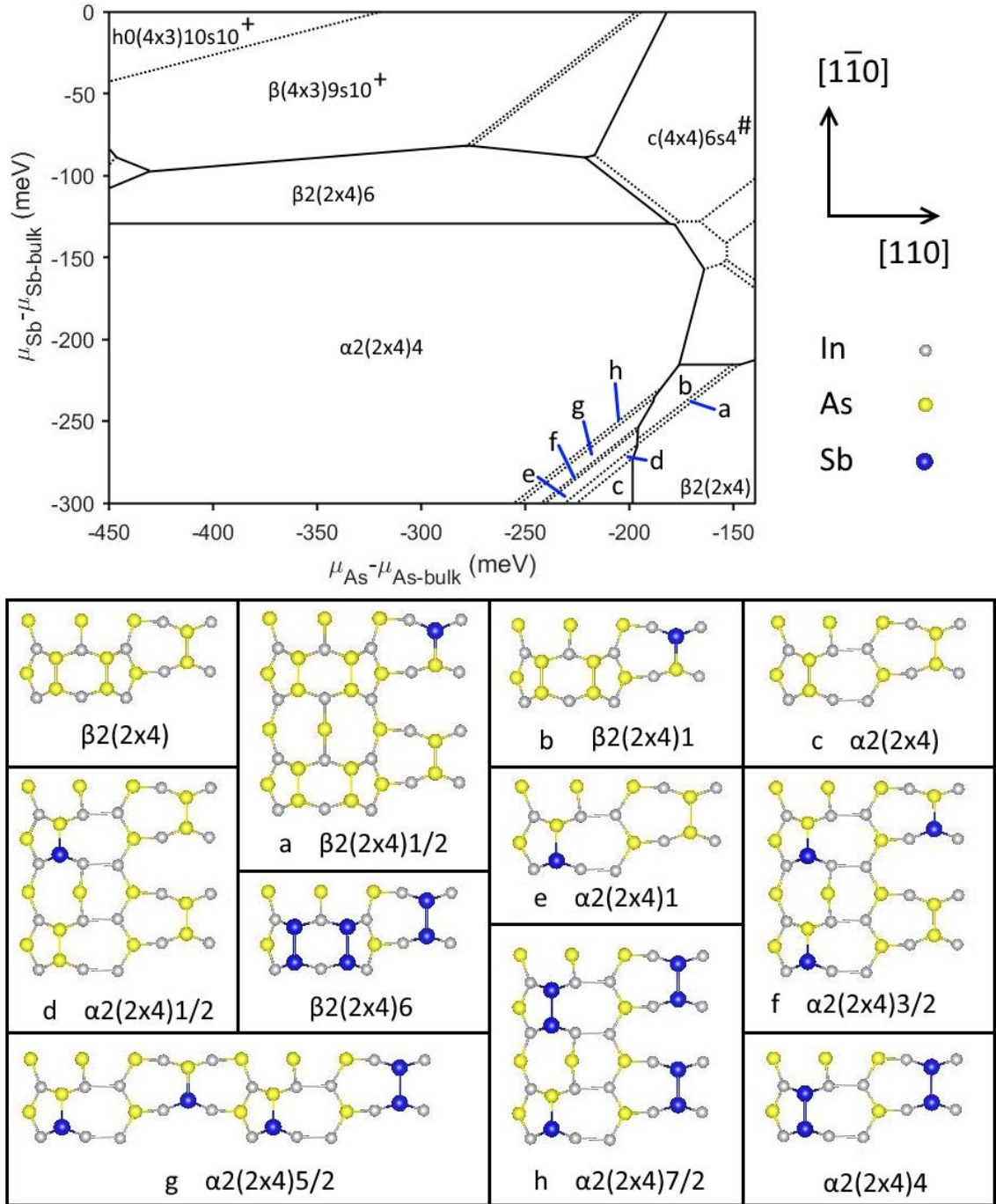


Figure B.4. 0K surface reconstruction phase diagram of Sb:InAs system over a limited chemical potential range and schematics corresponding to the labels on the diagram. +see Figure B.6. # see Figure B.5.

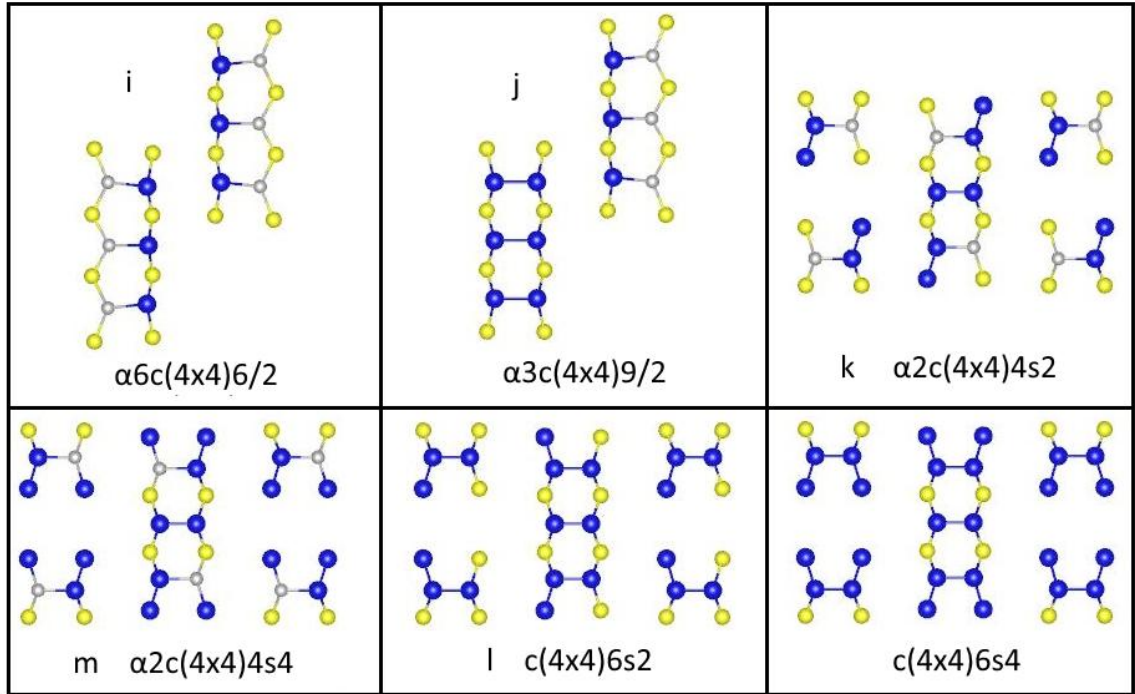
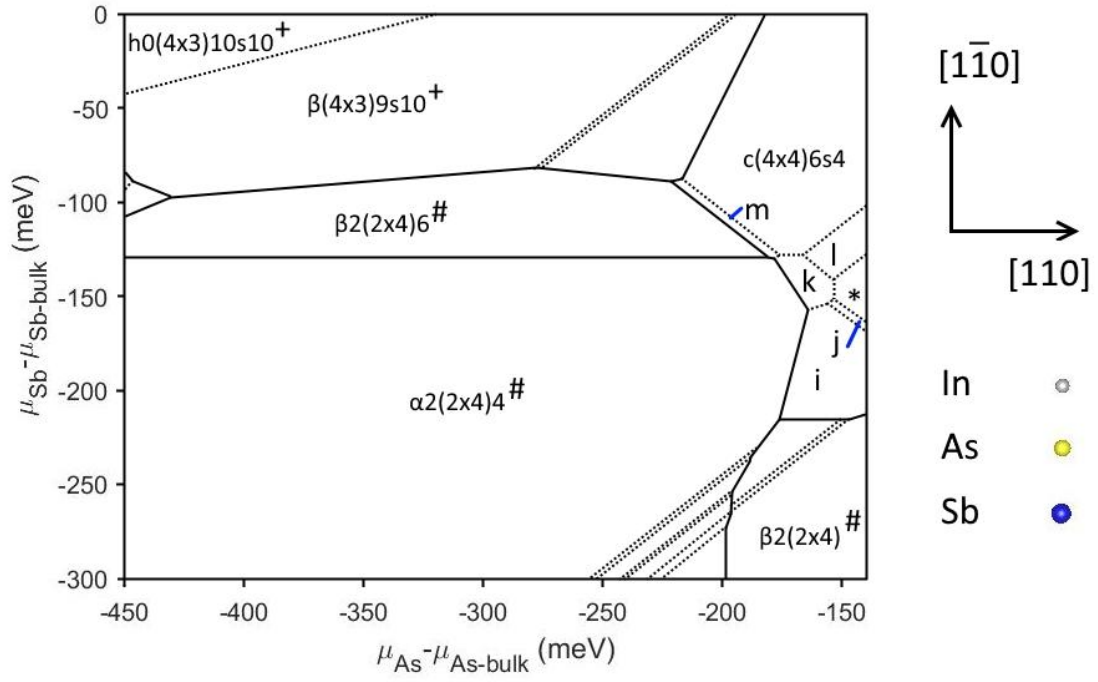


Figure B.5. 0K surface reconstruction phase diagram of Sb:InAs system over a limited chemical potential range and schematics corresponding to the labels on the diagram. +see Figure B.6. # see Figure B.4. * see Figure B.3.

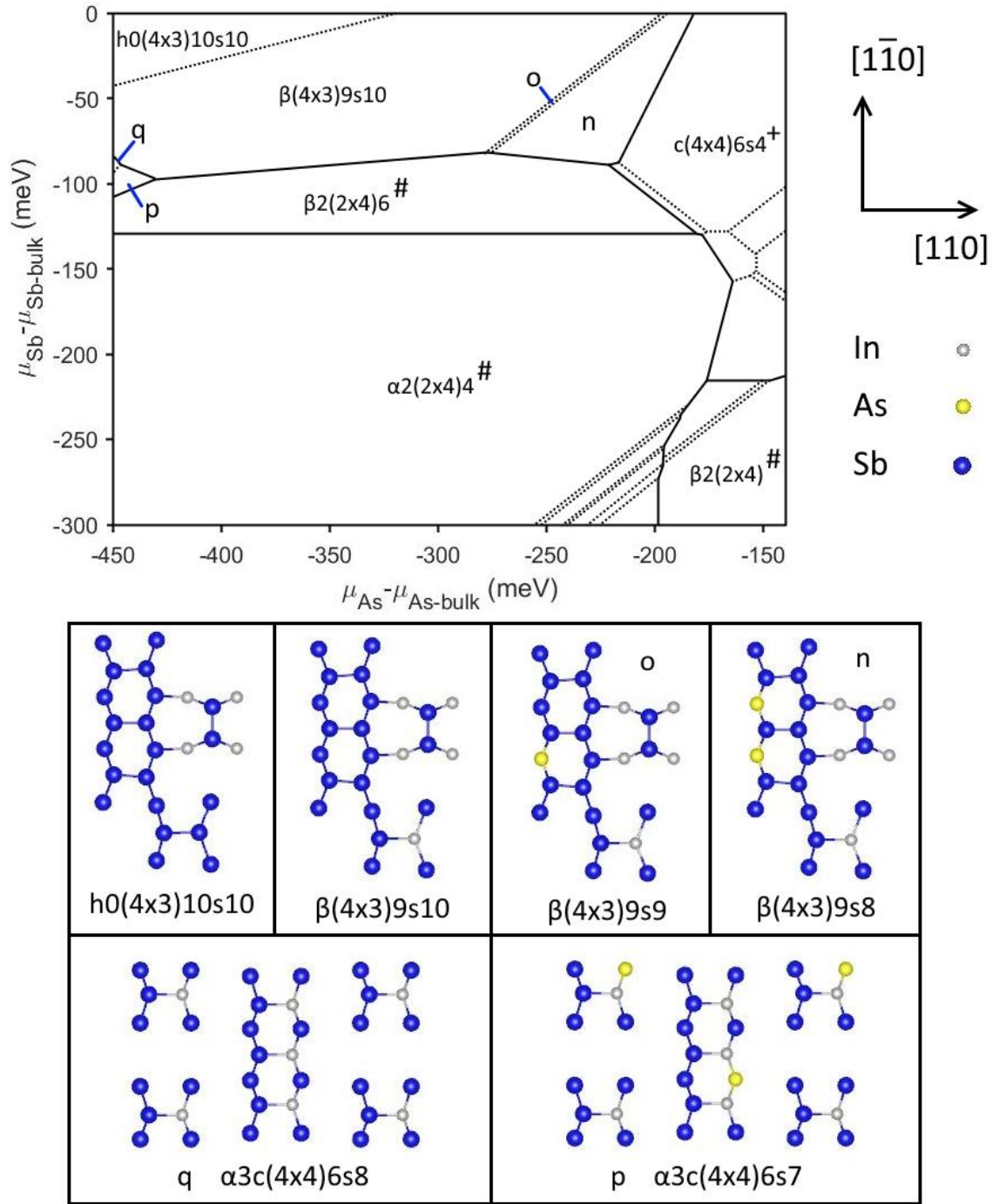


Figure B.6. 0K surface reconstruction phase diagram of Sb:InAs system over a limited chemical potential range and schematics corresponding to the labels on the diagram. +see Figure B.5. # see Figure B.4.

REFERENCES

- [1] S. P. Svensson, W. L. Sarney, H. Hier, Y. Lin, D. Wang, D. Donetsky, L. Shterengas, G. Kipshidze, and G. Belenky, *Phys. Rev. B* **86**, 245205 (2012).
- [2] M. Y. Yen, B. F. Levine, C. G. Bethea, K. K. Choi, and A. Y. Cho, *Appl. Phys. Lett.* **50**, 927 (1987).
- [3] A. Rogalski, *Reports Prog. Phys.* **68**, 2267 (2005).
- [4] M. I. Vasilevskiy and E. V Anda, *Semicond. Sci. Technol.* **10**, 157 (1995).
- [5] P. Norton, *Opto-Electronics Rev.* **10**, 159 (2002).
- [6] D. Donetsky, G. Belenky, S. Svensson, and S. Suchalkin, *Appl. Phys. Lett.* **97**, 2 (2010).
- [7] C. Liao and K. Y. Cheng, *J. Cryst. Growth* **311**, 1976 (2009).
- [8] C. A. Wang, D. A. Shiau, and D. R. Calawa, *J. Cryst. Growth* **261**, 372 (2004).
- [9] E. S. Kouhsari, R. Faez, and M. Akbari Eshkalak, *Superlattices Microstruct.* **83**, 61 (2015).
- [10] E. H. Steenbergen, B. C. Connelly, G. D. Metcalfe, H. Shen, M. Wraback, D. Lubyshev, Y. Qiu, J. M. Fastenau, A. W. K. Liu, S. Elhamri, O. O. Cellek, and Y.-H. Zhang, *Appl. Phys. Lett.* **99**, 251110 (2011).
- [11] H. Miyoshi and Y. Horikoshi, *J. Cryst. Growth* **227–228**, 571 (2001).
- [12] I. T. Ferguson, A. G. Norman, B. A. Joyce, T.-Y. Seong, G. R. Booker, R. H. Thomas, C. C. Phillips, and R. A. Stradling, *Appl. Phys. Lett.* **59**, 3324 (1991).
- [13] M. Yano, H. Yokose, Y. Iwai, and M. Inoue, *J. Cryst. Growth* **111**, 609 (1991).
- [14] R. Kaspi, *J. Cryst. Growth* **201–202**, 864 (1999).
- [15] D. Lackner, O. J. Pitts, S. Najmi, P. Sandhu, K. L. Kavanagh, A. Yang, M. Steger, M. L. W. Thewalt, Y. Wang, D. W. McComb, C. R. Bolognesi, and S. P. Watkins, *J. Cryst. Growth* **311**, 3563 (2009).
- [16] J. Lu, E. Luna, T. Aoki, E. H. Steenbergen, Y. H. Zhang, and D. J. Smith, *J. Appl. Phys.* **119**, 95702 (2016).
- [17] M. Losurdo, P. Capezzuto, G. Bruno, A. S. Brown, T. Brown, and G. May, *J. Appl. Phys.* **100**, 13531 (2006).
- [18] A. J. Martin, A. H. Hunter, T. W. Saucer, V. Sih, E. A. Marquis, and J. Millunchick, *Appl. Phys. Lett.* **103**, 122102 (2013).
- [19] M. W. Wang, D. A. Collins, T. C. McGill, R. W. Grant, and R. M. Feenstra, *J. Vac. Sci. Technol. B Microelectron. Nanom. Struct.* **13**, 1689 (1995).
- [20] D. A. Collins, M. W. Wang, R. W. Grant, and T. C. McGill, *J. Appl. Phys.* **75**, 259 (1994).
- [21] R. Kaspi and K. R. Evans, *J. Cryst. Growth* **175/176**, 838 (1997).
- [22] M. R. Wood, K. Kanedy, F. Lopez, M. Weimer, J. F. Klem, S. D. Hawkins, E. A. Shaner, and J. K. Kim, *J. Cryst. Growth* **425**, 110 (2015).
- [23] S. C. Theiring, M. R. Pillai, S. A. Barnett, and B. W. Wessels, *J. Vac. Sci. Technol. B Microelectron. Nanom. Struct.* **15**, 2026 (1997).
- [24] O. J. Pitts, S. P. Watkins, C. X. Wang, V. Fink, and K. L. Kavanagh, *J. Cryst. Growth* **254**, 28 (2003).

- [25] A. Semenov, O. G. Lyublinskaya, V. A. Solov'ev, B. Y. Meltser, and S. V Ivanov, *J. Cryst. Growth* **301–302**, 58 (2007).
- [26] H. Kim, Y. Meng, J. L. Rouvière, D. Isheim, D. N. Seidman, and J. M. Zuo, *J. Appl. Phys.* **113**, 0 (2013).
- [27] J. Steinshneider, J. Harper, M. Weimer, C.-H. Lin, S. S. Pei, and D. H. Chow, *Phys. Rev. Lett.* **85**, 4562 (2000).
- [28] I. T. Ferguson, A. G. de Oliveira, and B. A. Joyce, *J. Cryst. Growth* **121**, 267 (1992).
- [29] E. C. Young, S. Tixier, and T. Tiedje, *J. Cryst. Growth* **279**, 316 (2005).
- [30] A. J. Ptak, D. A. Beaton, and A. Mascarenhas, *J. Cryst. Growth* **351**, 122 (2012).
- [31] M. R. Pillai, S.-S. Kim, S. T. Ho, and S. A. Barnett, *J. Vac. Sci. Technol. B Microelectron. Nanom. Struct.* **18**, 1232 (2000).
- [32] C. Ratsch, W. Barvosa-Carter, F. Grosse, J. Owen, and J. Zinck, *Phys. Rev. B* **62**, R7719 (2000).
- [33] C. McConville, T. Jones, F. Leibsle, S. Driver, T. Noakes, M. Schweitzer, and N. Richardson, *Phys. Rev. B* **50**, 14965 (1994).
- [34] P. Laukkanen, M. P. J. Punkkinen, N. Räsänen, M. Ahola-Tuomi, M. Kuzmin, J. Lång, J. Sadowski, J. Adell, R. E. Perälä, M. Ropo, K. Kokko, L. Vitos, B. Johansson, M. Pessa, and I. J. Väyrynen, *Phys. Rev. B* **81**, 35310 (2010).
- [35] F. Grosse, W. Barvosa-Carter, J. J. Zinck, and M. F. Gyure, *J. Vac. Sci. Technol. B Microelectron. Nanom. Struct.* **20**, 1178 (2002).
- [36] B. Z. Nosh, B. V Shanabrook, B. R. Bennett, W. Barvosa-Carter, W. H. Weinberg, and L. J. Whitman, *Surf. Sci.* **478**, 1 (2001).
- [37] E. M. Anderson, A. M. Lundquist, W. L. Sarney, S. P. Svensson, P. J. Carrington, J. M. Millunchick, and C. Pearson, *J. Appl. Phys.* **116**, 14901 (2014).
- [38] S. B. Zhang and A. Zunger, *Appl. Phys. Lett.* **71**, 677 (1997).
- [39] A. Duzik and J. M. Millunchick, *J. Appl. Phys.* **116**, 23511 (2014).
- [40] M. Masnadi-Shirazi, D. A. Beaton, R. B. Lewis, X. Lu, and T. Tiedje, *J. Cryst. Growth* **338**, 80 (2012).
- [41] S. B. Zhang, S. Froyen, and A. Zunger, *Appl. Phys. Lett.* **67**, 3141 (1995).
- [42] A. Chakrabarti, P. Kratzer, and M. Scheffler, *Phys. Rev. B* **74**, 245328 (2006).
- [43] A. G. Norman, R. France, and A. J. Ptak, *J. Vac. Sci. Technol. B Microelectron. Nanom. Struct.* **29**, 03C121 (2011).
- [44] W. Barvosa-Carter, A. S. Bracker, J. C. Culbertson, B. Z. Nosh, B. V Shanabrook, L. J. Whitman, H. Kim, N. A. Modine, and E. Kaxiras, *Phys. Rev. Lett.* **84**, 4649 (2000).
- [45] J. C. Thomas, N. A. Modine, J. M. Millunchick, and A. Van der Ven, *Phys. Rev. B* **82**, 165434 (2010).
- [46] E. Tournié and K. H. Ploog, *Thin Solid Films* **231**, 43 (1993).
- [47] S. Zaima, K. Sato, T. Kitani, T. Matsuyama, H. Ikeda, and Y. Yasuda, *J. Cryst. Growth* **150**, 944 (1995).
- [48] J. R. Arthur, *Surf. Sci.* **500**, 189 (2002).
- [49] J. R. Waterman, B. V Shanabrook, and R. J. Wagner, *J. Vac. Sci. Technol. B* **10**, 895 (1992).
- [50] B. F. Lewis, R. Fernandez, A. Madhukar, and F. J. Grunthaner, *J. Vac. Sci. Technol. B Microelectron. Nanom. Struct.* **4**, 560 (1986).
- [51] G. Binnig and H. Rohrer, *Rev. Mod. Phys.* **59**, 615 (1987).
- [52] G. Kresse and J. Furthmüller, *Phys. Rev. B* **54**, 11169 (1996).
- [53] D. M. Ceperley and B. J. Alder, *Phys. Rev. Lett.* **45**, 566 (1980).

- [54] D. Vanderbilt, Phys. Rev. B **41**, 7892 (1990).
- [55] A. Duzik, J. Thomas, A. van der Ven, and J. Millunchick, Phys. Rev. B **87**, 35313 (2013).
- [56] A. Van der Ven, J. C. Thomas, Q. Xu, and J. Bhattacharya, Math. Comput. Simul. **80**, 1393 (2010).
- [57] J. C. Thomas, First Principles Investigation of Entropy and Equilibrium Atomic Structure at the Surface of III – V Semiconductors by, University of Michigan, 2012.
- [58] S. Curtarolo, W. Setyawan, G. L. W. Hart, M. Jahnatek, R. V. Chepulskii, R. H. Taylor, S. Wang, J. Xue, K. Yang, O. Levy, M. J. Mehl, H. T. Stokes, D. O. Demchenko, and D. Morgan, Comput. Mater. Sci. **58**, 218 (2012).
- [59] J. Thomas, J. Millunchick, N. Modine, and A. van der Ven, Phys. Rev. B **80**, 125315 (2009).
- [60] A. J. Duzik, Effects of Bi on the Morphology and Atomic Structure of III-V Semiconductor Surfaces by, University of Michigan, 2013.
- [61] J. C. Thomas, A. van Der Ven, J. M. Millunchick, and N. A. Modine, Phys. Rev. B - Condens. Matter Mater. Phys. **87**, 1 (2013).
- [62] H. Miyoshi, R. Suzuki, H. Amano, and Y. Horikoshi, J. Cryst. Growth **237–239**, 1519 (2002).
- [63] T. H. Chiu, W. T. Tsang, J. A. Ditzenberger, S. N. G. Chu, and J. P. Van Der Ziel, J. Appl. Phys. **60**, 205 (1986).
- [64] P. J. Carrington, Q. Zhuang, M. Yin, and A. Krier, Semicond. Sci. Technol. **24**, 1 (2009).
- [65] X. Marcadet, A. Rakovska, I. Prevot, G. Glastre, B. Vinter, and V. Berger, J. Cryst. Growth **227–228**, 609 (2001).
- [66] A. Ohtake and N. Koguchi, Appl. Phys. Lett. **83**, 5193 (2003).
- [67] O. Romanyuk, V. Kaganer, R. Shayduk, B. Tinkham, and W. Braun, Phys. Rev. B **77**, 235322 (2008).
- [68] P. R. Pukite, C. S. Lent, and P. I. Cohen, Surf. Sci. **161**, 39 (1985).
- [69] M. A. Berding, A. Sher, A.-B. Chen, and W. E. Miller, J. Appl. Phys. **63**, 107 (1988).
- [70] K. Muraki, S. Fukatsu, Y. Shiraki, and R. Ito, Appl. Phys. Lett. **61**, 557 (1992).
- [71] S. P. Svensson, F. J. Crowne, H. S. Hier, W. L. Sarney, W. a Beck, Y. Lin, D. Donetsky, S. Suchalkin, and G. Belenky, Semicond. Sci. Technol. **30**, 35018 (2015).
- [72] A. A. Allerman, R. M. Biefeld, and S. R. Kurtz, Appl. Phys. Lett. **69**, 465 (1996).
- [73] B. V. Olson, E. A. Kadlec, J. K. Kim, J. F. Klem, S. D. Hawkins, A. Tauke-Pedretti, W. T. Coon, T. R. Fortune, and E. A. Shaner, Appl. Phys. Lett. **109**, (2016).
- [74] A. Ohtake, J. Nakamura, S. Tsukamoto, N. Koguchi, and A. Natori, Phys. Rev. Lett. **89**, 206102 (2002).
- [75] G. Bell, J. Belk, C. McConville, and T. Jones, Phys. Rev. B **59**, 2947 (1999).
- [76] A. Duzik, J. C. Thomas, J. M. Millunchick, J. Lång, M. P. J. Punkkinen, and P. Laukkanen, Surf. Sci. **606**, 1203 (2012).
- [77] A. G. de Oliveira, S. D. Parker, R. Droopad, and B. A. Joyce, Surf. Sci. **227**, 150 (1990).
- [78] A. J. Noreika, M. H. Francombe, and C. E. C. Wood, J. Appl. Phys. **52**, 7416 (1981).
- [79] W. K. Liu and M. B. Santos, Surf. Sci. **319**, 172 (1994).
- [80] B. F. Mason and S. Laframboise, Surf. Sci. **258**, 279 (1991).
- [81] S. Kim, S. Erwin, B. Noshov, and L. Whitman, Phys. Rev. B **67**, 121306 (2003).
- [82] J. M. Millunchick, E. M. Anderson, C. Pearson, W. L. Sarney, and S. P. Svensson, J. Appl. Phys. **114**, 234907 (2013).
- [83] M. Mayer, *SIMNRA User's Guide*, 6th ed. (Max-Planck-Institut für Plasmaphysik, Garching, Germany, 1997).

- [84] M. Mayer, AIP Conf. Proc. **475**, 541 (1999).
- [85] Y. Zhong, P. B. Dongmo, J. P. Petropoulos, and J. M. O. Zide, Appl. Phys. Lett. **100**, 112110 (2012).
- [86] A. Duzik and J. M. Millunchick, J. Cryst. Growth **390**, 5 (2014).
- [87] R. B. Lewis, M. Masnadi-Shirazi, and T. Tiedje, Appl. Phys. Lett. **101**, 82112 (2012).
- [88] E. C. Young, M. B. Whitwick, T. Tiedje, and D. a. Beaton, Phys. Status Solidi **4**, 1707 (2007).
- [89] T. A. Flaim and P. D. Ownby, J. Vac. Sci. Technol. **8**, 661 (1971).
- [90] B. W. Liang and C. W. Tu, J. Appl. Phys. **74**, 255 (1993).
- [91] J.-M. Lin, L.-C. Chou, and H.-H. Lin, J. Vac. Sci. Technol. B Microelectron. Nanom. Struct. **29**, 21011 (2011).
- [92] X. Lu, D. A. Beaton, R. B. Lewis, T. Tiedje, and M. B. Whitwick, Appl. Phys. Lett. **92**, 192110 (2008).
- [93] J. Y. Tsao, *Materials Fundamentals of Molecular Beam Epitaxy* (Academic Press, San Diego, 1993).
- [94] C. Ratsch, Phys. Rev. B **63**, 161306 (2001).
- [95] J. Bickel, N. Modine, C. Pearson, and J. Millunchick, Phys. Rev. B **77**, 125308 (2008).